INVESTIGATION OF HOT DILUTE AND HOT COMPRESSED NUCLEAR MATTER

by

MIN-JUI HUANG

A DISSERTATION

Submitted to
Michigan State University
in partial fulfillment of the requirements
for the Degree of

DOCTOR OF PHILOSOPHY

Department of Physics and Astronomy

1997

ABSTRACT

INVESTIGATION OF HOT DILUTE AND HOT COMPRESSED NUCLEAR MATTER

by

MIN-JUI HUANG

Breakup temperatures were determined for the ^{197}Au + ^{197}Au collisions at E/A = 35 MeV and the ^{129}Xe + ^{nat}Cu collisions at E/A = 30 MeV from the relative populations of excited states of ^{5}Li, ^{4}He and ^{10}B fragments and nine double ratios involving the yields of elements with $1 \leq Z \leq 6$. These two experiments were measured from the Miniball-Multics array. Unlike results reported at significantly higher energies, all thermometers for these two experiments yield temperatures that are consistent within the experimental uncertainties.

Extrapolation of the data for the ^{197}Au + ^{197}Au reactions to zero impact parameter yields $T_{em} = 4.6 \pm 0.4\ MeV$, 1.5 MeV lower than the temperature assumed in Statistical Multifragmentation Model calculations which describe most of the other features of this reaction.

For ^{129}Xe + ^{nat}Cu reactions, the breakup temperature for zero impact parameter was also extrapolated and yields $T_{em} = 3.9 \pm 0.4\ MeV$. The number was then compared with BUU calculations and the breakup temperature is shown to favor the soft equation of state before the cooling correction.

For another experiment, ^{84}Kr+^{197}Au collisions at E/A = 200 MeV, directed transverse fragment flow was extracted by using techniques that are free of reaction plane dispersion. The fragment flow per nucleon increases with mass, following a thermal- or coalescence-like behavior, and attains roughly constant limiting values at $4 \leq A \leq 12$. Comparisons of the impact parameter dependences of the measured coalescence-invariant proton flow to Boltzmann-Uehling-Uhlenbeck calculations clearly favor a momentum dependent nuclear mean field.

To

my lovely wife

Yuanling

ACKNOWLEDGMENTS

First, I owe my deepest gratitude to my advisor, Professor Bill Lynch, for giving me a chance to do research with him. He has always been a great help to me. His understanding and perspective in physics helped me stay on the right track and benefited me a lot. His invaluable advice and guidance also helped me finishing my thesis work.

I learned a lot from Professor Betty Tsang and Dr. Hongfei Xi. Professor Betty Tsang contributed a lot in my data analysis and helped me through the thesis writing. Dr. Hongfei Xi has especially helped me in the analysis of temperature measurements. I also thank Professor Alan Galonsky, Professor Wolfgang Bauer, Professor S D Mahanti, and Professor Dan Stump, for kindly serving on my advisory committee and for many helpful comments and suggestions about my dissertation.

It was very lucky for me to work on Miniball group. I owe great deal for their help and their friendship: J. Dinnus, S. Gaff, C.K. Gelbke, T. Glasmacher, D. Handzy, W.C. Hsi, L. Martin, C. Montoya, M.A. Lisa, L. Phair, G. Peaslee, R. Popescu,and C. Williams. Especially, I'd like to thank for Professor T. Glasmacher. He helped me to organize my thesis experiment a lot. I also want to express my gratitude to the staff members of the laboratory, especially J. Ottarson. Without them, the experiment wouldn't be accomplished. The Multics group from Italy kindly provided the experimental device for my thesis experiment and helped me finish the experiment. Especially, I want to thank Dr. C. Nicola and Dr. Milazzo for their help in the experiment and data analysis. The REU student E. Scannapieco, who analyzed the silicon detector efficiency of Multics telescope, also gave me much help in my thesis experiment.

In the analysis of transverse flow, I got a lot of help from Dr. R. Lemmon, Frank Daffin, Dr. K. Haglin, Professor W. Bauer, and Professor P. Danielewicz. I want to thank for their help.

The writing group was formed in November, 1996. This group includes Professor S.K. Thomas, K.D. Kessler, Professor Betty Tsang, Dr. Homgfei Xi, S. Gaff, and R. Shomin. They gave me much instruction in how to write and organize my dissertation. I'd like to thank for their time too.

I owe thanks to many NSCL employees for their roles in helping me work at the cyclotron lab. They are: Kay Barber, Shari Conroy, Tina Keehnm Rilla McHarris, Chris O'conner, Barb Pollack, Reg Ronningen, Dennis Swan, and Chris Townsend.

Finally, I want to thank for my parents and my lovely wife. Without their support, I would not be able to finish the dissertation.

Contents

List of Figures

List of Tables

Chapter 1

Introduction

1.1 Background and Motivation

The study of nucleus-nucleus collisions provides a wealth of information about dynamical and statistical properties of highly excited nuclear systems. Using nuclear reactions one may investigate time dependent properties such as particle emission time scales, pre-equilibrium emission, nuclear viscosity, collective flow, as well as static properties such as the density, temperature, and pressure of systems in local thermal equilibrium. Both the importance and the typical values of these quantities evolve as a function of incident energy.

At low incident energies, the nucleon density stays close to the saturation density of cold nuclear matter $\rho_0 \sim 0.15 fm^{-3}$ and many of the global nuclear properties are well described by the liquid-drop model. In this incident energy region, the reaction dynamics are dominated by mean field, and individual nucleon-nucleon collisions are strongly suppressed due to the Pauli principle. In central collisions, the projectile and target typically fuse and particles are subsequently emitted by evaporation from the surface of the equilibrated compound nucleus [Bohr 36, More 72, Birk 83, Sobo 83]. Models for the decay of compound nuclei at moderate temperature assume that there is enough time between successive emissions for the relaxation of the compound nucleus into a new equilibrium state.

With increasing incident energy, the complete fusion of projectile and target becomes less likely. As the temperature of hot nuclear systems is increased, the time intervals between successive emissions become comparable with the relaxation time $\tau_{rel} = 2R/c_s$, where R is the radius of a compound nucleus and c_s is the (zero) sound velocity in nuclear matter. In this case, particles are often emitted early in the reaction before the residual nuclei can reach global equilibrium, instead of from a fully equilibrated compound nucleus [Gelb 87].

For sufficiently high incident energies, the excitation energy becomes comparable to the total binding energy ($\epsilon^* \sim 8MeV/nucleon$), and the emission time becomes very short. Measurements indicate that the system may totally disintegrate over a time scale of $\tau < 100fm/c$ [Bowm 91, deSo 91], leading to the multiple emission of fragments (multifragmentation). If the decay occurs as a bulk disintegration, a final state of interacting fragments and nucleons may result; the system can be viewed as a mixed phase of gas (nucleons) and liquid drops (light nuclei). If the system appears to be in thermal equilibrium, it may be an appropriate domain to study the liquid-gas phase transition of nuclear matter.

At relativistic energies, individual nucleon-nucleon collisions play a dominant role in the reaction, contributing to a rapid thermalization. Such collisions may produce nuclear systems which are at very high density and temperature. This domain has provided information about the nuclear equation of state at high density, much needed for the understanding of supernova and neutron star formation and stability.

Even higher densities and temperatures that may be achieved at the Relativistic Heavy Ion Collider (RHIC). Here, nucleons in the nucleus may even dissolve into quarks and gluons and form a quark-gluon plasma [Good 84, Stöc 86]. These extreme environments can provide information about the birth of the universe in the first fractions of a second of the big bang; and the interiors of neutron stars [Stöc 86].

Experiments at the NSCL probe an energy domain that is lower than that needed to produce a quark-gluon plasma, but sufficient to the multifragmentation and the bulk phase transition between nuclear liquid and nuclear gas. Moreover, the information relevant to the nuclear equation of state can be also obtained from collisions at NSCL energies. Recent experiments at the NSCL, at the GANIL facility in Caen, France, at GSI facility in Darmstadt, Germany, at the SATURNE facility in Saclay, France, and at the Bevalac facility in Berkeley have increased our understanding of these issues in this energy range. The following subsections will elaborate two of these topics: the liquid-gas phase transition and the equation of state of nuclear matter.

1.1.1 Liquid-Gas Phase Transition

The interactions between nucleons in nuclear matter are attractive at small distances ($\sim$ 1 fm) and repulsive at even smaller distances. This behavior is similar to the van der Waals equation of state which explains molecular interactions. And from this, one may expect that a liquid-gas phase transition can take place in nuclear matter at temperatures

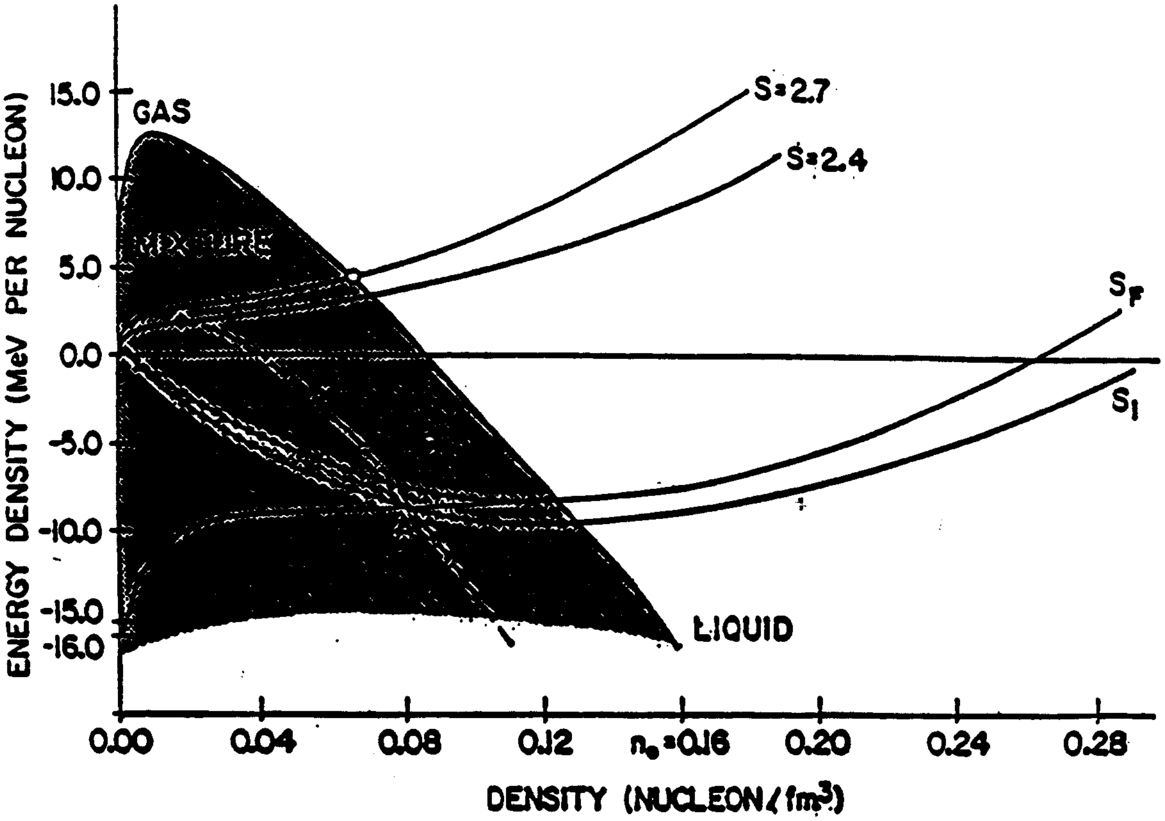

Figure 1.1: Phase boundaries for nuclear matter are shown as a function of nuclear matter density and energy density [Lope 84]. Also shown are isentropes corresponding to the critical point (open circle, $S = 2.7$) and the endpoint (solid circle, $S = 2.4$). Inside the mixed phase region are shown the spinodal (dashed line) and the Maxwell construction of the proper mixed phase entropy curve (solid line) and the mechanically unstable isentropes S_i and S_f (dotted lines) [Lync 87].

less than the critical temperature T_c and density less than normal nuclear matter density ρ_0 [Saue 76, Lamb 81, Schu 82, Jaqa 83, Jaqa 84, Good 84, Boal 86]. A typical phase diagram for nuclear matter is shown in Fig. 1.1 [Lope 84]. Similar to the phase diagram of water, it has regions of liquid, gas, and mixed liquid-gas phases.

One scenario under which a phase transition can occur has been given by Lopez *et al.* [Lope 84]. A hot composite system is formed after the initial collision of two nuclei. The system cools off by expanding isentropically until the system reaches the point where the compressibility $\kappa = \rho(\partial P/\partial \rho)|_s$ becomes negative (here P is the pressure, ρ is the nuclear density, and s is the entropy). In this region the system breaks up and fragmentation occurs [Lope 84]. Within the region of liquid-gas coexistence, fragments are considered to be droplets of liquid embedded in a gas of nucleons. Thermodynamical properties of nuclear matter are strongly reflected in the relative abundance of fragments [Lync 87]. In some approaches, the emission of intermediate mass fragments (IMF's: $3 \leq Z \leq 20$) is then considered to be a signature of statistical clustering near the critical point in the liquid-gas phase diagram [Finn 82].

Properties of liquid-gas phase transition has been calculated in a variety of calculations for infinite nuclear matter [Saue 76, Curt 83, Jaqa 83, Jaqa 84, Rose 84] and also for finite nuclear systems [Stoc 73, Küpp 74, Saue 76, Frie 81, Rave 83, Bonc 84, Sero 86, Schl 87, Sura 87]. These calculations differ somewhat in their predictions for the critical temperature T_c up to about 17 MeV [Saue 76, Curt 83]. Besides these statistical models which try to model the liquid-gas phase transition, there are other statistical models [More 75, Fiel 84, Hahn 87], and dynamical models [Boal 89, Peil 89, Sura 89, Sura 90], which do not predict a phase transition that have also successfully reproduced many features of experimental data. All these models have different strengths and rely on different assumptions about how the system disintegrates. To distinguish among these, additional measurements such as the breakup time scales and the fragment energy spectra are needed. These additional measurements will eventually allow one to eliminate inappropriate models and constrain the parameters of the others.

Since the development of the multifragment detection arrays, considerable experimental evidence related to the liquid-gas phase transition has been obtained. For example, multifragment emission mechanisms have been measured for central Au + Au and Kr + Au reactions for incident energies of E/A = 35 - 400 MeV [Peas 94, Hsi 94, Dago 95, Kund 95]. The measurements for central ^{84}Kr + ^{197}Au collisions reveal that intermediate mass fragment production increases up to maximum of E/A $\approx$ 100 MeV, and then decreases at higher energies [Peas 94]. The decrease in fragment multiplicities for central collisions at incident energies greater than E/A = 100 MeV is also observed for ^{197}Au + ^{197}Au reactions and is consistent with the onset of nuclear vaporization [Tsan 93].

The time scales for multifragmentation, measured via fragment-fragment correlation functions, are short ($\tau \leq 100$ fm/c) at E/A $\gtrsim$ 50 MeV, and provide supporting evidence for a prompt bulk multifragmentation [Bowm 91, Lace 93, Lope 93, Corn 95]. These experiments reveal one of the necessary conditions for mixed phase equilibrium, i.e. the existence a mixture of fragments (i.e. liquid) and nucleons (i.e. vapor) in close proximity to be met in intermediate incident energy nuclear reaction. Comparisons of the Statistical Multifragmentation Model (SMM) with some experimental observables from 35 AMeV ^{197}Au + ^{197}Au reactions show a good agreement with the experimental observables [Dago 96, Dago 96a]. Despite these promising indications, information about freeze-out temperatures and densities for bulk disintegrations need to be measured to proceed with the accurate extraction of thermodynamic quantities from such collisions. Examining the validity of the assumption of local equilibrium at freeze-out is also necessary to discern non-equilibrium and dynamical effects.

Since the thermodynamic limit of macroscopic nuclear material is best realized in the laboratory for the heaviest possible nuclear systems, studies of central collisions between heavy nuclei, such as Au + Au, are of particular relevance. Previous investigations reveal that approximately ten intermediate mass fragments are produced in central Au + Au collisions at E/A = 35 MeV [Dago 95]. Coulomb interactions can alter the experimental determinations of critical exponents for the nuclear liquid-gas phase transition, especially in the highly charged systems produced in Au + Au collisions [Pan 95]. Indeed, exceedingly flat charge distributions are observed [Dago 95] which calculations predict to be a consequence of the destabilizing Coulomb interaction [Pan 95]. Both fragment-fragment correlations and fragment kinetic energy spectra are reasonably described by the Coulomb driven breakup of single thermalized source [Dago 96, Dago 96a]. These experimental observations have been well reproduced by SMM calculations wherein the fragments are produced via a bulk multifragmentation at a density of $\rho_0/6 \leq \rho \leq \rho_0/3$ and a temperature of $T \approx 6MeV$ [Botv 87, Bond 95, Dago 96, Dago 96a]. Tests of the validity of such models, however, will be more stringent if the assumed values of the temperature, density or both can be constrained experimentally. In this dissertation, the breakup temperature of this Au + Au system will be studied via measurements of excited state populations and isotope ratios to provide such constraints.

1.1.2 Equation of State of Nuclear Matter

In order to study the nuclear liquid-gas phase transition, the equation of state (EOS) of nuclear matter needs to be understood. The properties of the nuclear EOS are discussed in terms of nuclear compressibility, which measures how difficult it is to push the system away from its equilibrium. Different values of compressibility reflect different difficulty of the energies required to make the system expand to low density or contract to high density. Near normal nuclear density, compressibility K, which is characterized in terms of $\frac{9}{\rho_0^2}\frac{d^2\epsilon}{d\rho^2}|_{\rho=\rho_0}$, has been extracted from experimental measurements of the giant monopole resonance [Blai 76, Blai 80, Trei 81], from the Landau theory of Fermi liquids [Brow 85], from the nuclear hydrodynamics [Buch 84], and from the droplet model of nuclear masses [Mack 77]. The range of K varies from 74 to 410 MeV [Glen 88]. This range of values reflects the fact that less is known about the EOS at either low ($\rho < \rho_0$) densities or high ($\rho > \rho_0$) densities than for densities close to ρ_0.

The nuclear equation of state at $\rho < \rho_0$ plays an important role in nuclear liquid-gas phase transition and may eventually be constructed by studies of residue formation and multifragmentation [Stöc 78, Stoc 82, Stöc 86, Stoc 86a]. Residues calculated with a large value of K come to equilibrium sooner and at higher density than do residues calculated with a smaller value of K. Thus one way to distinguish the stiffness of nuclear equation of state is to measure the emission temperatures of a residue and compare to transport models such as Boltzmann-Uehling-Uhlenbeck (BUU) calculations. For sufficiently high

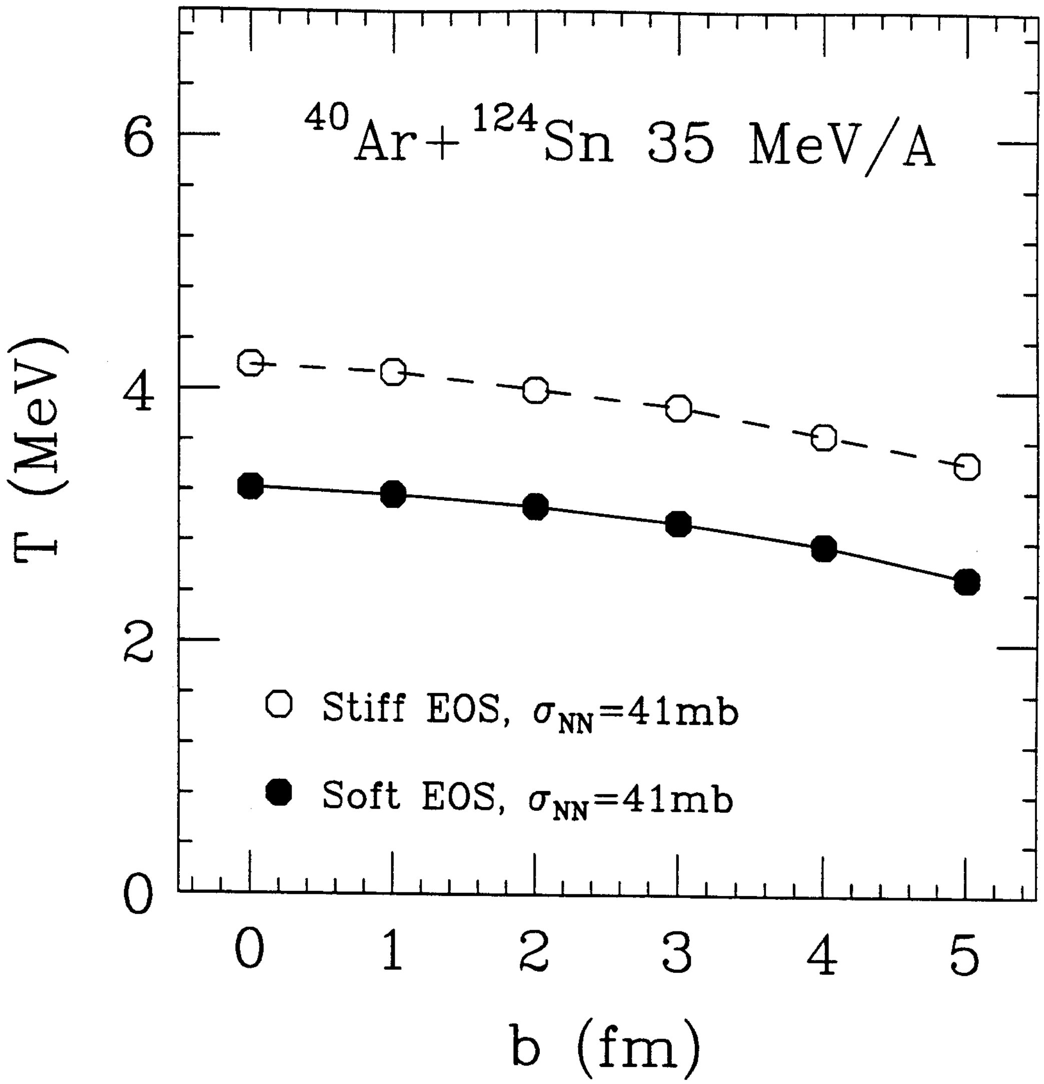

Figure 1.2: Sensitivities of the temperature to the impact parameter and the EOS for ^{40}Ar + ^{124}Sn collisions at E/A = 35 MeV. The RMS uncertainties in the calculations are equal to the radii of the data points [Xu 93].

bombarding energy deposition, residues calculated using a mean field with small value of K may expand to low density $\rho \leq 0.3\rho_0$ and multi-fragment while residues calculated using a mean field with large value of K do not. Thus the fragment yield can be a signature of the nuclear EOS at low density.

Let us examine the mechanism for residue production further using the BUU equation. The BUU equation describes the time evolution of the Wigner function $f(\mathbf{r}, \mathbf{k}, t)$ in phase space [Wong 82, Bert 84, Aich 85, Krus 85, Bert 87, Baue 92]:

$$\begin{aligned}&\frac{\partial f_1}{\partial t} + \mathbf{v} \cdot \nabla_r f_1 - \nabla_r U \cdot \nabla_p f_1 = \\ &\frac{4}{(2\pi)^3} \int d^3k_2 d\Omega \frac{d\sigma_{nn}}{d\Omega} v_{12}[f_3 f_4(1-f_1)(1-f_2) - f_1 f_2(1-f_3)(1-f_4)] \qquad (1.1)\end{aligned}$$

Here, $\frac{d\sigma_{nn}}{d\Omega}$ and v_{12} are the cross section and relative velocity for the colliding nucleons, and U is the mean field potential approximated by

$$U = A\rho/\rho_0 + B(\rho/\rho_0)^\gamma \qquad (1.2)$$

where $\rho_0 = 0.17 fm^{-3}$ is the saturation value of the nuclear matter density and $\rho = \rho(\mathbf{r})$ is the local density of nuclear matter. Values of A = -356 MeV, B = 303 MeV, and $\gamma = 7/6$ correspond to a soft nuclear equation of state (EOS) with compressibility coefficient K = 200 MeV; while A = -124 MeV, B = 70.5 MeV, and $\gamma = 2$ correspond to a stiff EOS with K = 375 MeV.

Within the BUU model, the emission temperatures measured from the stiff equation of state are higher than those measured from the soft equation of state because: 1. The stiff EOS has a large surface restoring force and a large sound velocity, leading to an earlier thermal freeze-out and consequently less time for cooling via pre-equilibrium emission [Xu 93, Xu 94, Xu 94a]. 2. The larger surface restoring force with the stiff equation of state means the residues have higher density and the level density parameter will be smaller, which makes the temperature higher. Fig. 1.2 [Xu 93] shows the calculated temperatures for stiff EOS and soft EOS as a function of impact parameter from BUU calculations. Both calculated temperatures show some dependence on impact parameter. The temperatures also show little sensitivity to the in-medium nucleon-nucleon cross section and are about 1 MeV higher for the stiff EOS than for the soft EOS, independent of the impact parameter. However, since information about impact parameter selected temperatures is rather limited, conclusions concerning the stiffness of the EOS were not be made in previous investigations [Xu 94]. In this dissertation, the impact parameter selected residue temperatures for ^{129}Xe + ^{nat}Cu at 30 AMeV are measured and compared to BUU calculations.

For $\rho > \rho_0$, one can measure the collective transverse flow to get information for the equation of state of finite nuclear matter. As two nuclei collide, the density and pressure increase in the interaction region, and at finite impact parameters there is an inherent asymmetry in the pressure, which results in a transverse flow of matter toward the direction of lowest pressure. The collective transverse flow was initially predicted by theoretical fluid dynamics [Sche 74, Amsd 75, Stöc 80], and also by a number of different transport equation models [Cuss 85, Krus 85, Aich 86, Gale 87] which incorporate compressional degrees of freedom in an equation of state. In these models the amount of transverse flow is directly related to the stiffness of the nuclear equation of state and transport properties of the nuclear medium [Bert 87].

The absolute magnitudes of the transverse flow measured by 4π devices [Beau 83, Gust 84, Renf 84, Ritt 85, Dani 85, Doss 87, Dani 88] are large and shown to be consistent

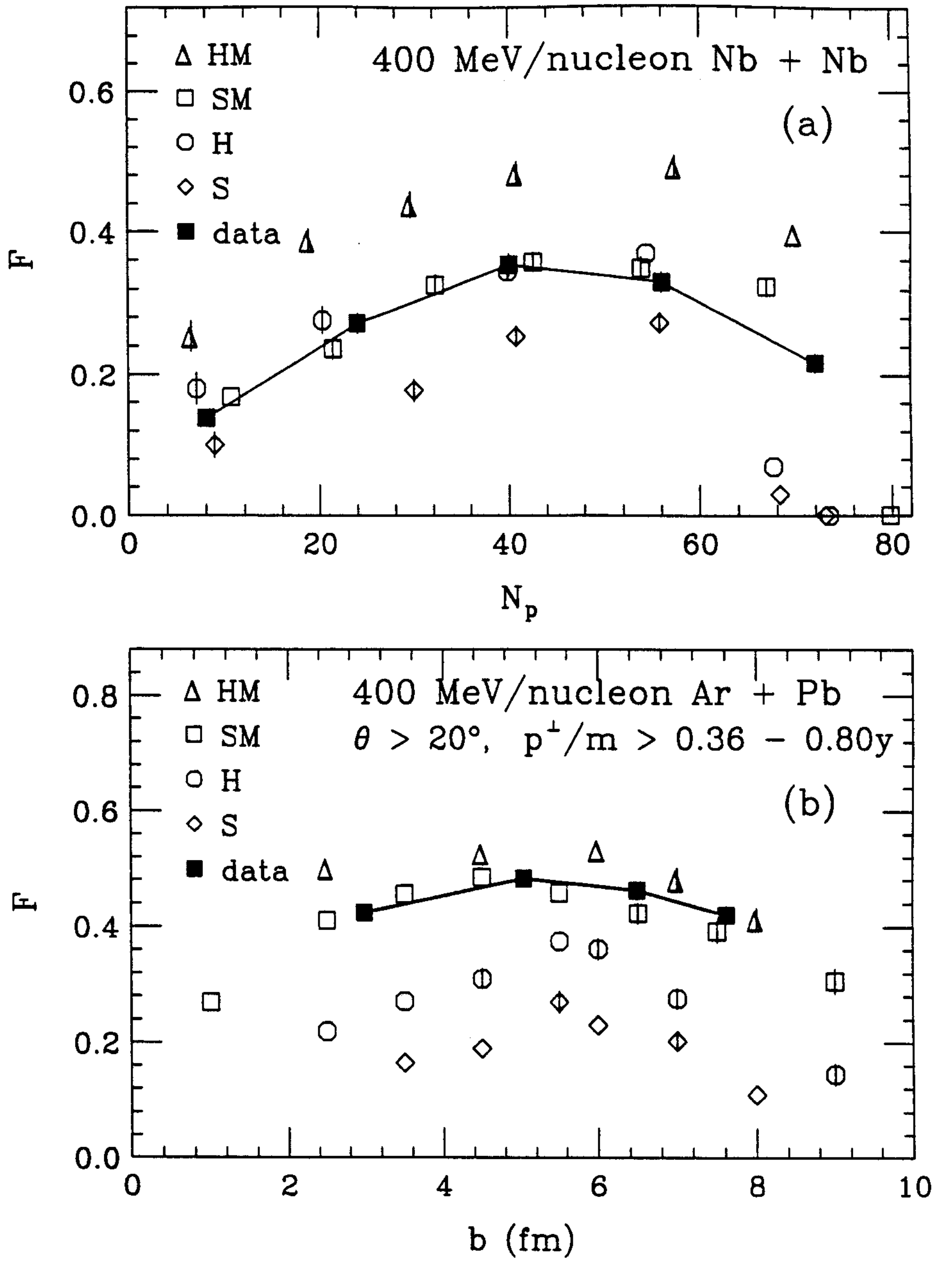

Figure 1.3: Flow parameter F in (a) Nb + Nb and (b) Ar + Pb reactions at 400 MeV/nucleon. Data of [Gust 88, Demo 90] (filled squares) are compared to the results of calculations for different mean fields (open symbols). In (a) and (b) the abscissa shows participant proton multiplicity and impact parameter, respectively. Error bars for the results of calculations, suppressed when less than symbol size, represent uncertainties due to finite statistics [Pan 93].

with a stiff nuclear equation of state [Sche 74, Baum 75, Stöc 80, Moli 85, Stöc 86]. However, Refs. [Aich 87, Gale 87] prove that with a strong momentum dependent force, the soft nuclear equation of state can reproduce the same magnitude of transverse flow as the stiff nuclear equation of state without the momentum dependent force. Fig. 1.3 [Pan 93] shows the values of the flow parameter F from the measurements for Nb + Nb at 400 MeV/nucleon [Gust 88] and Ar + Pb at 400 MeV/nucleon [Demo 90]. These two flow measurements are compared with transport model calculations for different optical potentials. These optical potentials differ from their compressibilities and momentum dependent forces. One can see in the top panel, the soft equation of state with a momentum dependent force (SM open squares) describes the data for mass symmetric Nb + Nb collisions as well as calculations with a momentum dependent stiff EOS (H open circles). However, a very different sensitivity to the EOS is displayed for the mass asymmetric Ar + Pb collisions shown in the bottom panel of Fig. 1.3. Here the sensitivity in compressibility of the EOS is reduced because low maximum densities derived for such an asymmetric system. The sensitivity to the momentum dependence remains. Only calculations utilizing the soft equation of state with a momentum dependent force conform with both sets of data to a reasonable extent.

Besides the sensitivities to the nuclear mean field, the collective transverse flow is also sensitive to the in-medium nucleon-nucleon cross sections. Intuitively, these cross sections could be expected to be lower than those in free space and therefore yield less flow [Bert 87]. The incompressibility in nuclear equation of state, momentum dependent forces, and in-medium nucleon-nucleon cross sections will have an influence on our analysis of the flow for ^{84}Kr + ^{197}Au reactions.

1.2 Organization

The dissertation is organized into six chapters. Chapter 1 lays out some background and interesting points in nuclear reaction physics. Chapter 2 describes experimental devices used in this dissertation – Miniball/Miniwall detectors and Multics array. This chapter also gives details of the calibration of the Multics array.

A variety of techniques used in the measurements of emission temperatures are provided in Chapter 3 – including excited state population and double isotope ratios. These techniques are then implemented in Chapter 4 to measure the emission temperatures of ^{197}Au + ^{197}Au collisions at E/A = 35 MeV and ^{129}Xe + ^{nat}Cu collisions at E/A = 30 MeV. Collective transverse flow for the ^{84}Kr + ^{197}Au system is discussed in Chapter 5. Chapter 6 will give the summary and conclusions.

Chapter 2

Experimental Setup

This thesis consists of the study of three different systems : ^{197}Au + ^{197}Au collisions at 35 AMeV, ^{129}Xe + ^{nat}Cu collisions at 30 AMeV, and ^{84}Kr + ^{197}Au collisions at E/A = 35, 55, 70, 100, 200, and 400 MeV. In each experiment, the MSU miniball, a low threshold 4π array, was supplemented by another array such as the Multics array or the Miniwall array both of which have a higher granularity at forward angles. Some details about the Miniball, Miniwall and Multics arrays will be overviewed in sections 2.1 - 2.3.

For the ^{197}Au + ^{197}Au collisions at 35 AMeV and ^{129}Xe + ^{nat}Cu collisions at 30 AMeV, the high-resolution MULTICS array [Iori 93] was combined with the MSU Miniball [deSo 90] to obtain measurements of isotope ratios and excited state populations. The experiments were performed at the National Superconducting Cyclotron Laboratory (NSCL). The beam intensity was $\sim 10^5$ particles/second for the Au beam and $\sim 10^6$ particles/second for the Xe beam. The thickness of target was 5 mg/cm^2 for the Au target and 4.55 mg/cm^2 for the Cu target. Charges and isotopes up to Z = 6 were detected at $3° \leq \theta \leq 23°$ in the Multics array. Light charged particles and fragments with charge up to Z = 20 were detected at $23° \leq \theta \leq 160°$ by 158 phoswich detector elements of the MSU Miniball. The geometric acceptance of the combined apparatus was greater than 87 % of 4π.

In the ^{84}Kr + ^{197}Au experiment, the MSU Miniball/Washington University Miniwall 4π phoswich detector array was used for the measurements of collective transverse flow. Measurements with ^{84}Kr ions at incident energies of E/A = 35, 55, and 70 MeV were performed with beams from the K1200 cyclotron of the NSCL. Typical beam intensities were $(1 - 2) \times 10^8$ particles per second (intensities were lower by a factor of 2 for the 70 AMeV beam). Measurements at E/A = 100, 200, and 400 MeV were performed at the Laboratoire National SATURNE, Saclay, France, with typical beam intensities of $10^6 - 10^7$ particles per spill. The gold target thicknesses were 1.3 mg/cm^2 at E/A = 35 and 55 MeV, 4 mg/cm^2 at E/A = 70 MeV, and 5 mg/cm^2 at E/A = 100, 200 and 400 MeV. Charged particles were detected with the phoswich (phosphor sandwiches) detectors of the Miniball/Miniwall 4π array. At high incident energies ($E/A \geq 100MeV$), the detector system consists of 276 low-threshold plastic-scintillator-CsI(Tl) phoswich detectors, covering polar angles of $\theta_{lab} = 5.4° - 160°$, corresponding to a total geometric efficiency of approximately 90% of 4π. For the experiment at lower incident energies ($E/A < 100MeV$), 268 plastic-scintillator-CsI(Tl) phoswich detectors were used. An ion chamber also substituted for one Miniball detector in each ring at $\theta_{lab} > 25°$.

2.1 MSU Miniball detection array

The original Miniball array [deSo 90] consists of 11 independent rings coaxial about the beam axis. The individual rings are mounted on separate base plates which slide on two precision rails for ease of assembly and servicing. The rings and detector mounts are made of aluminum. Good thermal conductivity between detectors and the mounting structure allows the Miniball array to operate at constant temperature by cooling the base plates. The individual detector mounts are designed to allow the removal of any detector without interfering with the alignment of neighboring detectors. The entire assembly is placed on an adjustable mounting structure which allows for the alignment of the apparatus with respect to the beam axis.

The half-plane section of the Miniball array in the vertical plane is shown in Fig. 2.1. Individual rings are labeled by the ring numbers 1 - 11 which increase from forward to backward angles. For each ring, the number of detectors is given in parentheses. For a given ring, the detectors are identical in shape and have the same polar angle coordinates with respect to the beam axis; the angles are also indicated in Fig. 2.1. Since the angular distributions of the emitted particles are strongly forward peaked, the solid angle subtended by forward detectors is smaller than for backward detectors. Variations in solid angle were achieved largely by placing detectors at different distances from the target while keeping their sizes approximately constant.

A schematic drawing of the detector design is given in Fig. 2.2. All detectors of the Miniball array are phoswiches and are composed of a thin plastic scintillator foil [Weat 96], spun from Bicron BC-498X scintillator solution, and a 2 cm CsI(Tl) scintillator crystal.

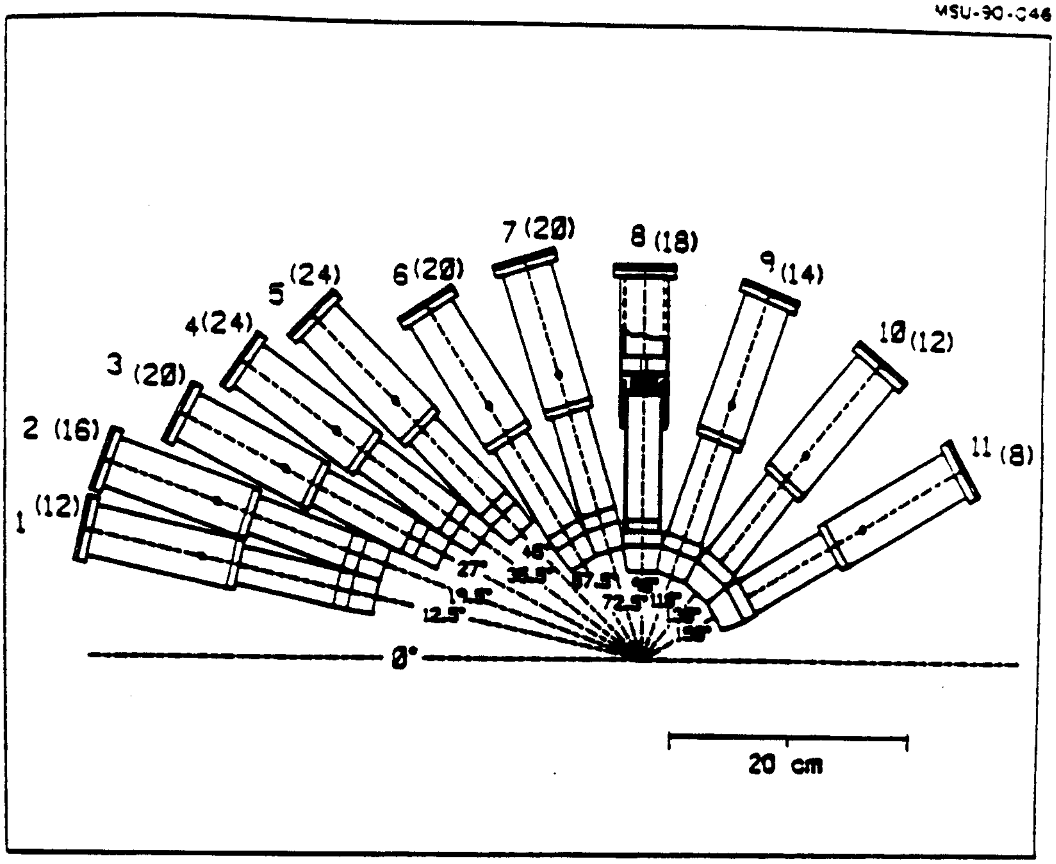

Figure 2.1: Half-plane section of the Miniball array. Individual detector rings are labeled 1 through 11. Numbers of detectors per ring are given in parentheses. The polar angles for the centers of the rings are indicated. The dashed horizontal line indicated the bean axis.

The foils have an average thickness of 4 mg/cm^2. (In the measurements of ^{197}Au + ^{197}Au reactions at 35 AMeV and ^{129}Xe + ^{nat}Cu reactions at 30 AMeV, the average thickness of the foils for ring 3 and ring 4 was increased to 8 mg/cm^2.) The CsI crystals are tapered such that the front and back surfaces subtend the same solid angle in a coordinate system centered on the target. In order to save some costs of fabrication, the curved surfaces were approximated by plane surfaces. The resulting loss in solid angle coverage is on the order of 2%, comparable in magnitude to the loss in solid angle coverage resulting from gaps between individual detectors (which must be provided to allow for mechanical tolerances and optical isolation between neighboring crystals).

The back face of the CsI(Tl) crystal was optically coupled to a clear acrylic light guide with the same dimensions as the crystal. This light guide, in turn, was optically connected to a photomultiplier tube of 1 inch diameter. The photomultiplier tube and the light guide were enclosed inside by a cylindrical μ-metal shield. The sides of the CsI(Tl) crystal and of the light guide were wrapped with white Teflon tape. The front face of the detector was covered by an aluminized mylar foil (0.15 mg/cm^2 mylar and 0.12 mg/cm^2 aluminum) to keep the detection assembly light-tight and to suppress low energy secondary electrons from hitting the plastic scintillator.

In the following the intermediate mass fragments (IMFs) are defined as charged particles with $3 \leq Z \leq 20$. With the Miniball/Miniwall phoswich detectors, charge resolution up to Z $\simeq$ 10 was routinely achieved for particles that traversed the fast plastic scintillator. However, high energy lithium ions that punched through the CsI(Tl) crystals were not counted as IMFs because they could not be distinguished from light particles.

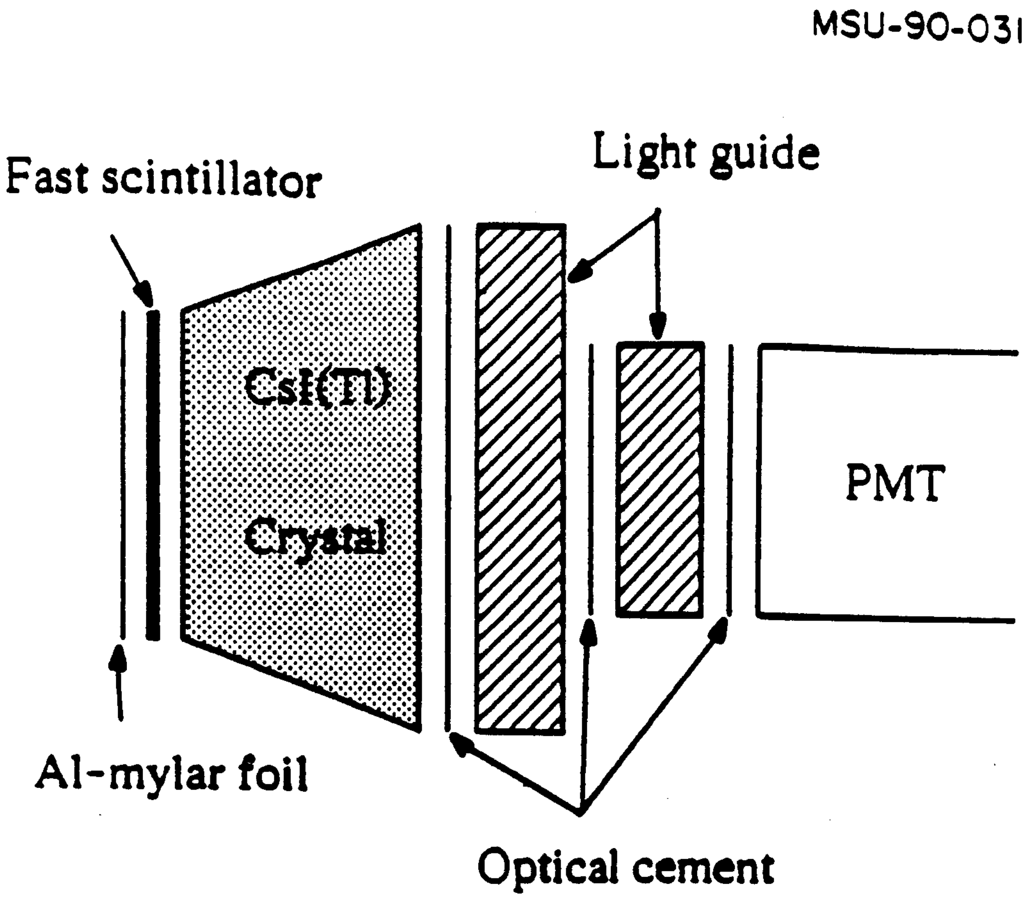

Figure 2.2: Schematic drawing of phoswich assembly of individual detector elements. The μ-metal shield covering the photo multiplier is not included.

Double hits consisting of two IMFs, two light particles, or IMF - light particle coincidences were identified as a single IMF. Typically, under these conditions, multiple hits reduced the charge particle multiplicity in central collisions by an estimated 15-25% and the IMF multiplicity by 1.5-2.5%, depending on the incident energy.

The energy thresholds for a typical ball detector were $E_{th}/A \sim 2$ MeV (4 MeV) for Z = 3 (Z = 10) particles, respectively. To avoid contamination from low energy electrons, hardware discriminator thresholds of 5 MeV were imposed on the Z = 1 particles for the Miniball. The calibration procedures described in Refs. [Phai 93, Hsi 95, Will 96] are used to calibrate all the detectors in the Miniball for the ^{84}Kr +^{197}Au experiments.

In the measurements of ^{197}Au + ^{197}Au collisions at 35 AMeV and ^{129}Xe + ^{nat}Cu collisions at 30 AMeV, the Miniball detector array mainly served as an impact parameter selector. The impact parameters in these two experiments were obtained from the charged particles multiplicity detected in the Miniball array.

The original Miniball array contained 187 phoswich detectors to cover the polar angle $9° \leq \theta_{lab} \leq 160°$ and was designed to address the problems of accurately measuring the multiplicities and angular distributions for asymmetric collisions like ^{36}Ar + ^{197}Au [deSo 91, Kim 92, Phai 92]. Higher particle multiplicities that may occur at high incident energies and heavy systems could cause a double-hit problem wherein single detectors are hit by two particles from a single event. To reduce the problem, the granularity of the Miniball at $\theta_{lab} \leq 25°$ are overcome by replacing them with the Miniwall array.

2.2 Washington Miniwall detection array

The Miniwall detector array was built by L.G. Sobotka *et al.* at Washington University in St. Louis. The Miniwall array consists of a total of 128 detectors arranged in 6 rings, spanning from $\theta_{lab} = 3.3°$ to 25.0°. Similar to Miniball detectors, each Miniwall detector contains a fast plastic foil ($\sim 8mg/cm^2$) and a 3 cm long CsI(Tl) crystal. The mechanical configuration of the Miniwall was quite compact with all the detectors attached to the same plate. A cooling line was mounted around the edge of the plate to keep the temperature of the photomultiplier tubes constant during the experiment.

In the ^{84}Kr $+^{197}$Au experiments, the first three rings of the Miniball array (total 48 detectors) were replaced by Washington University Miniwall detectors and a new ring 3' of Miniball (total 156 detectors). The energy thresholds for particle identification in a typical Miniwall detector were $E_{th}/A \sim$ 4 MeV (6 MeV) for Z = 3 (Z = 10) particles, respectively. For the higher incident energies (E/A $\geq$ 100 MeV), the energy thresholds for particle identification in the wall were somewhat higher at about $E_{th}/A \sim$ 7 MeV (7.5 MeV) for Z = 3 (10) particles. To avoid contamination from low energy electrons, hardware discriminator thresholds of 10 MeV were applied for the Miniwall detectors. For incident energies with $E/A \geq 100MeV$, the Z = 1 thresholds for the Miniwall were higher, typically 20 MeV. Both the charge and energy resolutions of the Miniwall detectors are similar to the Miniball. Similar energy calibrations as described in Refs. [Hsi 95, Will 96] are used.

2.3 Multics Array

The original Multics array is composed of 48 identical telescopes in a 7x7 array with the center cell empty to allow the beam to go through. The Multics array operates in a vacuum vessel and was placed at 53.7 cm from the target. It covers polar angles from 3° to 23°. The solid angle of each Si detector is about 6.4 msr. In the study of Au + Au and Xe + Cu reactions, four telescopes at the corners which cover the polar angle between 23° and 26° were taken out to make the Multics array match smoothly with the Miniball array. The most central four telescopes were covered with 0.5 mm thick Aluminum plate to stop the elastically scattered Au projectiles (The grazing angle is 5.0° for ^{197}Au + ^{197}Au at 35 AMeV and 2.7° for ^{129}Xe + ^{nat}Cu at 30 AMeV.)

Every telescope in Multics array is shaped as a truncated pyramid (170 mm high) and contains three different elements: an ionization chamber filled with CF_4 gas, a solid state detector, and a CsI(Tl) scintillating crystal with photodiode readout. A picture of the Multics+Miniball detectors and the schematic sketch of the three-element telescope are shown in Fig. 2.3.

The pyramidal envelope of each telescope, for a length of 85 mm, is the ionization chamber (IC). The ionization chamber is of the axial type as this configuration minimizes the active area loss. The entrance window (42.4 x 42.4 mm^2) is also the cathode. The Frisch grid and the anode define the active volume and are mounted on the rear cover.

The second element of the telescope, the silicon detector (Si), is position sensitive in two coordinates. It has an active area of 49.5 x 49.5 mm^2 and a typical thickness of $500\mu m$. The silicon detector has a resistive cathode, the charge flowing to this electrode

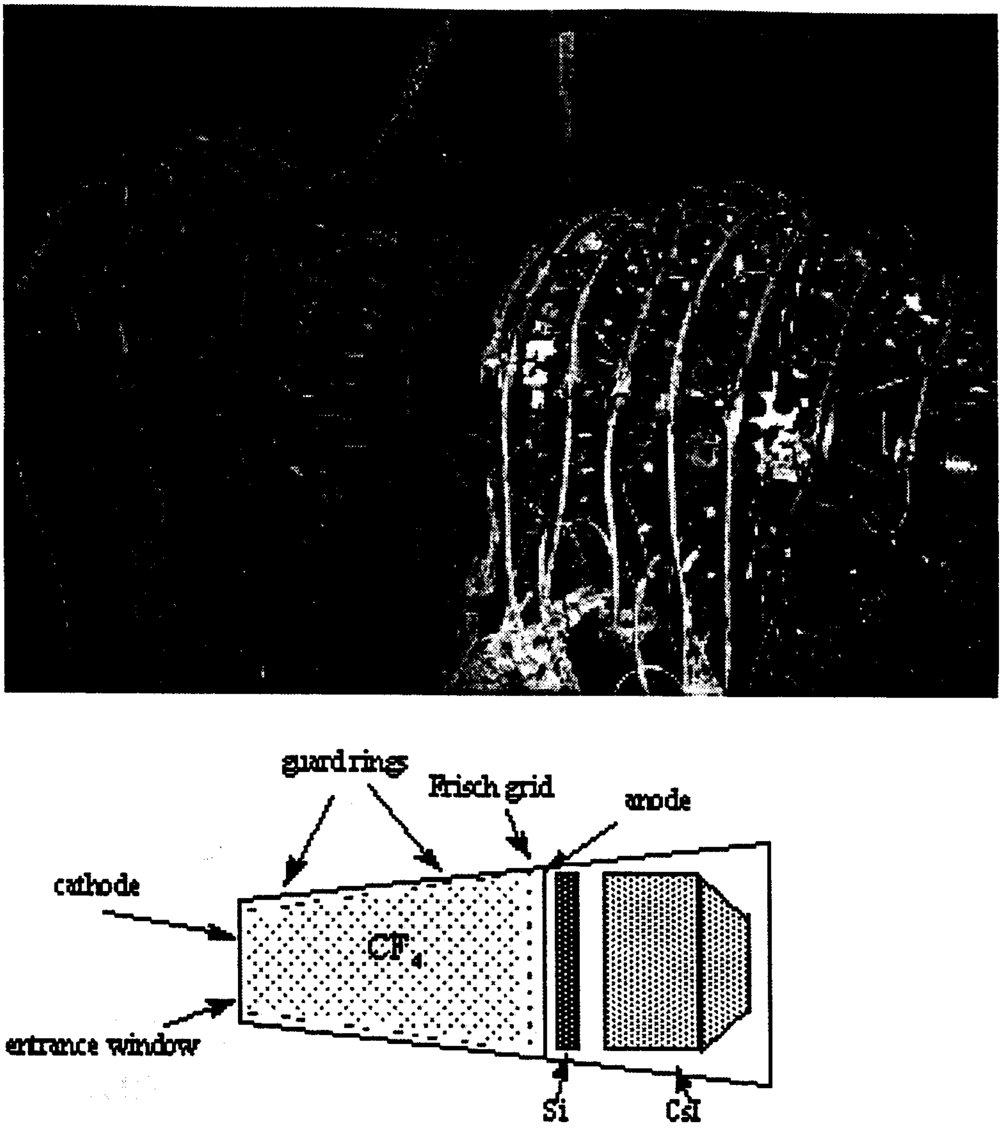

Figure 2.3: Schematic Drawing of the Multics Array

is divided by the resistive layer, as a nonlinear function of the position, into four signals available at the corners of the detector. The energy loss information is collected directly by the anode signal. More details about the position resolution of silicon detectors will be given in a later section.

The CsI(Tl) crystal's total length is 41 mm, and for the last 16 mm, it's shaped as truncated pyramids. The larger base of this pyramidal structure is 51 x 51 mm^2 and is at the end of the Si detector while the smaller one (25 x 25 mm^2) is coupled to the photodiode. The response function of CsI(Tl) crystal is a reasonably linear function of the ion's kinetic energy above a given energy (5 - 6 MeV/A) and has good isotope resolution. The preamplifiers are located in the detector module to reduce noise and to improve performance.

A geometrical inefficiency of about 25% comes from the edges of the silicon detectors and the walls of the ion chamber, while the gaps left between the telescopes account for additional 3% [Brun 91].The pressure of CF_4 in the ionization chamber is reduced to 40 mbar to decrease the energy threshold of the telescopes in these experiments. (The normal pressure of CF_4 is around 200 mbar in other experiments.) The gas was mainly used to cool the silicon detectors in the present experiment.

Light charged particles and IMF's were detected in the Multics array and analyzed for 35 AMeV ^{197}Au + ^{197}Au and 30 AMeV ^{129}Xe + ^{nat}Cu reactions. The dynamic range of the electronics for the Multics array was optimized to provide maximum isotopic resolution for $1 \leq Z \leq 6$ and isotopically resolved yields could be determined for emitted ^{1,2,3}H, ^{3,4,6}He, ^{6,7,8,9}Li, ^{7,9,10}Be, ^{10,11,12,13}B, and ^{12,13,14}C nuclei. Representative identification thresholds of 8.5, 5.5, 4, 8.5, 10.5, 12 and 13.5 AMeV were achieved in the Multics array for p, d, t,

α, ^{6}Li, ^{9}Be, and ^{10}B nuclei, respectively. Energy calibrations accurate to 2% were obtained by irradiating each telescope with ^{228}Th and ^{244}Cm α sources and with low intensity direct beams of p, d, t, ^{3}He, α, ^{6}Li, ^{7}Li, ^{7}Be, ^{9}Be, ^{10}B, ^{11}B, ^{12}C and ^{16}O particles.

2.3.1 Electronics Setup for Multics Array

The data acquisition electronics diagram is shown in Fig. 2.4. The signals from the ion chamber and CsI elements are sent to charge sensitive preamplifiers, followed by shaping amplifiers. The signals are then sent to an Amplitude to Digital Converter (ADC) for digitization and are subsequently read by the computer. The signals generated from the energy and the four position channels of the silicon detectors are digitalized in the same way.

The energy signal of the silicon detector of each telescope was used to generate the trigger. The output from the splitter was sent to a fast time amplifier (FTA) to generate a trigger signal, then the signal was sent to a constant fraction discrimination (CFD) to generate a logic signal which was then sent to a logic box along with other silicon detector logic signals. The trigger condition in this experiment was set with the requirement that the multiplicity of the Miniball detectors must be greater than two or at least one telescope must have a signal. When the computer is reading data from the ADCs, it will send a signal to veto all the subsequent events that occur while it is busy.

2.3.2 Energy Calibration for Multics Array

From computer simulations of energy resolution performed with the calculation, we know the accuracy of the energy calibration is more important than the energy resolution

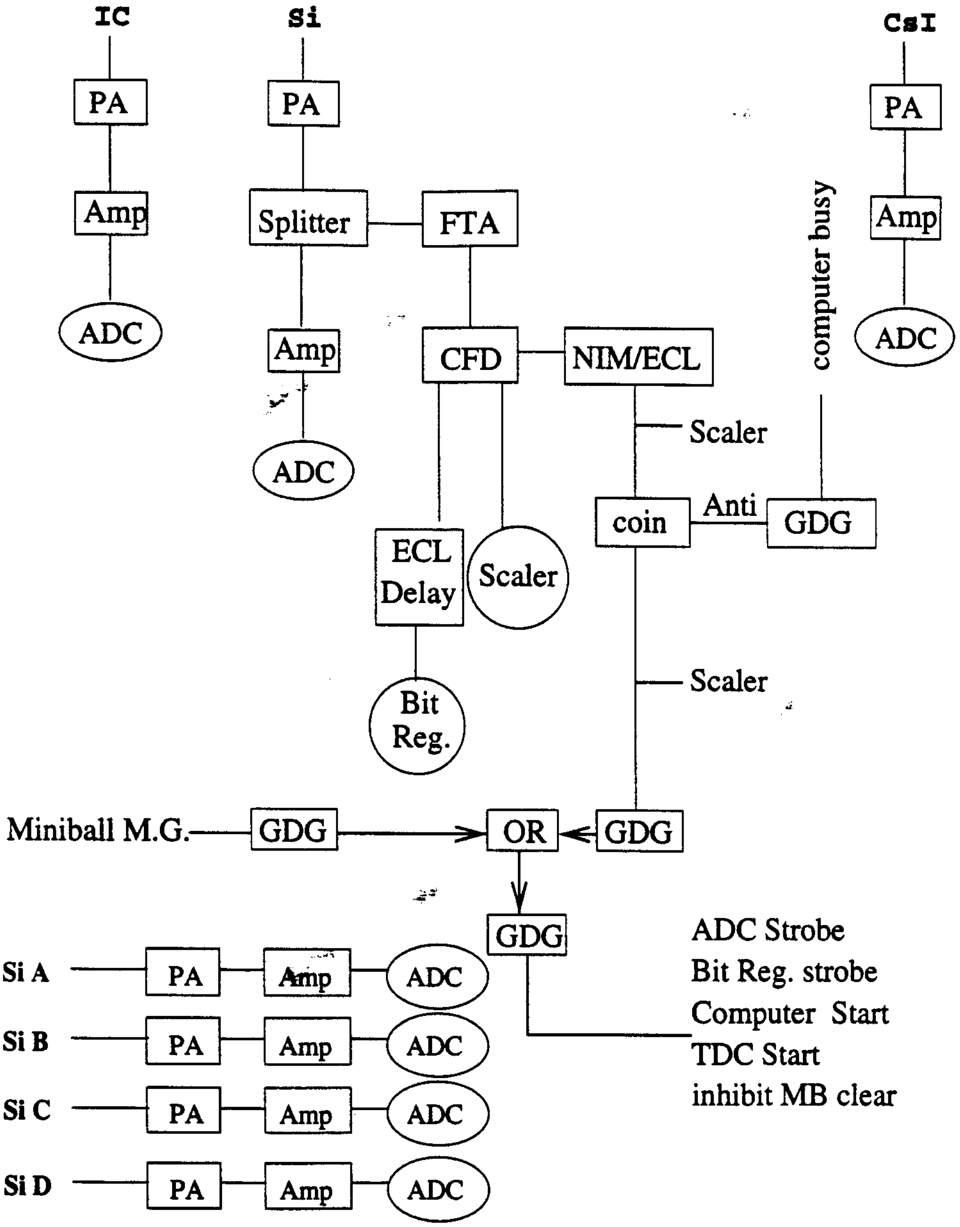

Figure 2.4: The multics electronics diagram

of individual detectors. To achieve a good energy calibration, cocktail beams of ^{4}He, ^{12}C, and ^{16}O at 40.16 MeV/A were used, and a ^{12}C beam was also impinged into a thick aluminum target to produce a lot of fragments that were subsequently analyzed by the A1200 spectrometer as follows. The ^{12}C fragmentation beam was passed through a magnet. From electromagnetic theory, the radius of curvature ρ of a beam in a dipole magnet with field B, charge q, and mass number A, one gets

$$\rho = \frac{mv}{qB} \tag{2.1}$$

$$\frac{E}{A} = \sqrt{U^2 + (B\rho\frac{299.7925Z}{A})^2} - U \tag{2.2}$$

where $U = \frac{M}{A} = 931.49432$ MeV. By choosing different values of the magnetic rigidity $B\rho$ ($B\rho$ = 1.03, 1.1, 1.3 in the experiments), we can select different energies for the isotopes we are interested in calibrating. The beam was then sent directly into individual telescopes to establish the energy calibration. With a single ^{12}C beam at 40.16 MeV/A produced by the cyclotron, we calibrated the Multics detectors with ^{1}H, ^{2}H, ^{3}H, ^{3}He, ^{4}He, ^{6}Li, ^{7}Li, ^{7}Be, ^{9}Be, ^{10}B, and ^{11}B ions via the fragmentation method.

Because the silicon detectors have good linear response to the energy deposition, the energy calibration of silicon detectors is quite straight forward. Fig. 2.5 shows the energy calibration for a typical silicon detector. The solid circles are the particles that stopped in the silicon detector and the open points are the particles that punched through silicon detectors. The silicon energies deposited by punch through particles are calculated using Littmark-Ziegler table [Litt 80]. After corrections for the energy loss of the target, entrance window, the ion chamber, the data can be fitted by a straight line: $E = a \times ch + b$,

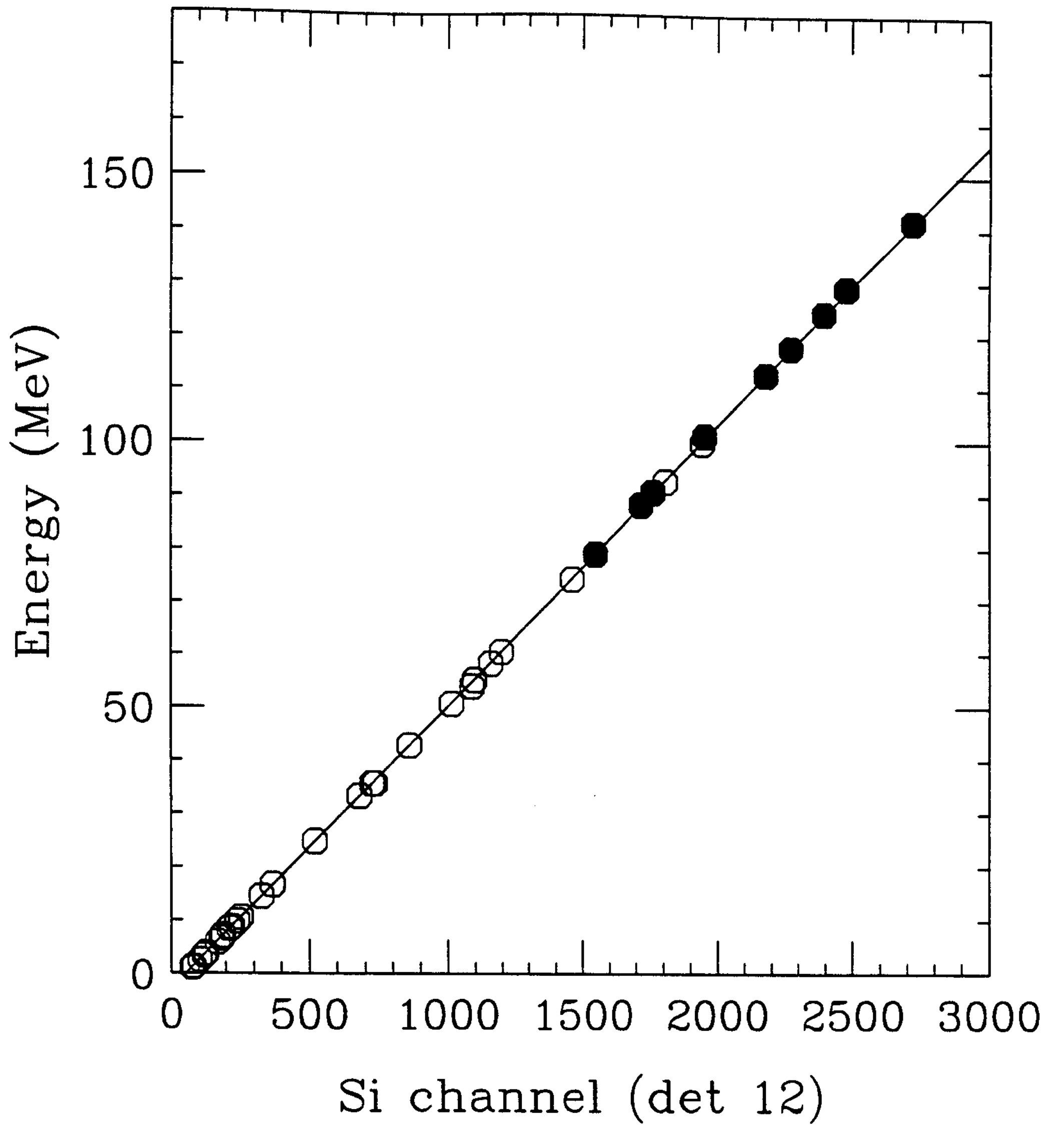

Figure 2.5: Si energy calibration for det 12. Solid points are the particles that stopped in the silicon detector; open points are the particles that punch through silicon detector. The line is a straight line fit.

where E is the energy, ch is the channel number, b is the ADC pedestal, and a is the slope parameter. As expected, the collected charge (channel No.) is simply a linear function of energy deposited in the silicon detector.

For the CsI(Tl) energy calibration, corrections of energy losses in the ion chamber and silicon detector were also included. For light charged particles (H and He isotopes), a linear fit $y = ax + b$ was used for light charged particles [Gong 91, Lisa 93]. Due to the nonlinear and particle dependent response of CsI(Tl) to the energy of heavy fragments, the CsI energies were calibrated by K. Michaelian's model which the energies are isotope dependent [Mich 94]. The comparison between calibrated data and model calculation is shown in Fig. 2.6. The points are the experimental data for Li, Be and B isotopes; the lines are the calculations from K. Michaelian's model. A normalization constant C for each particle type was used to normalize the calculations to the data points. Inset shows the deviation of normalization constant δC for each particle type compared to the average. In Fig. 2.7, the calibration points for all telescopes are plotted together for ^{6}Li and ^{7}Be and compared to the model (dashed lines). One can see the predicted energies of the model are somewhat lower than the calibration energies for low CsI channels and higher for high CsI channels with both ^{6}Li and ^{7}Be.

To reduce the systematic errors introduced by this model, we made a small correction $y = a_0 + a_1 x + a_2/x$ for CsI channel (x) greater than 50. Here y is the deviation between the previous calculated energy using the K. Michaelian's model and calibrated energy, and a_0, a_1, and a_2 are the free parameters to be used to adjust the calculated energies to agree with the energies of the calibration beams. The results for the corrected energy for ^{6}Li and

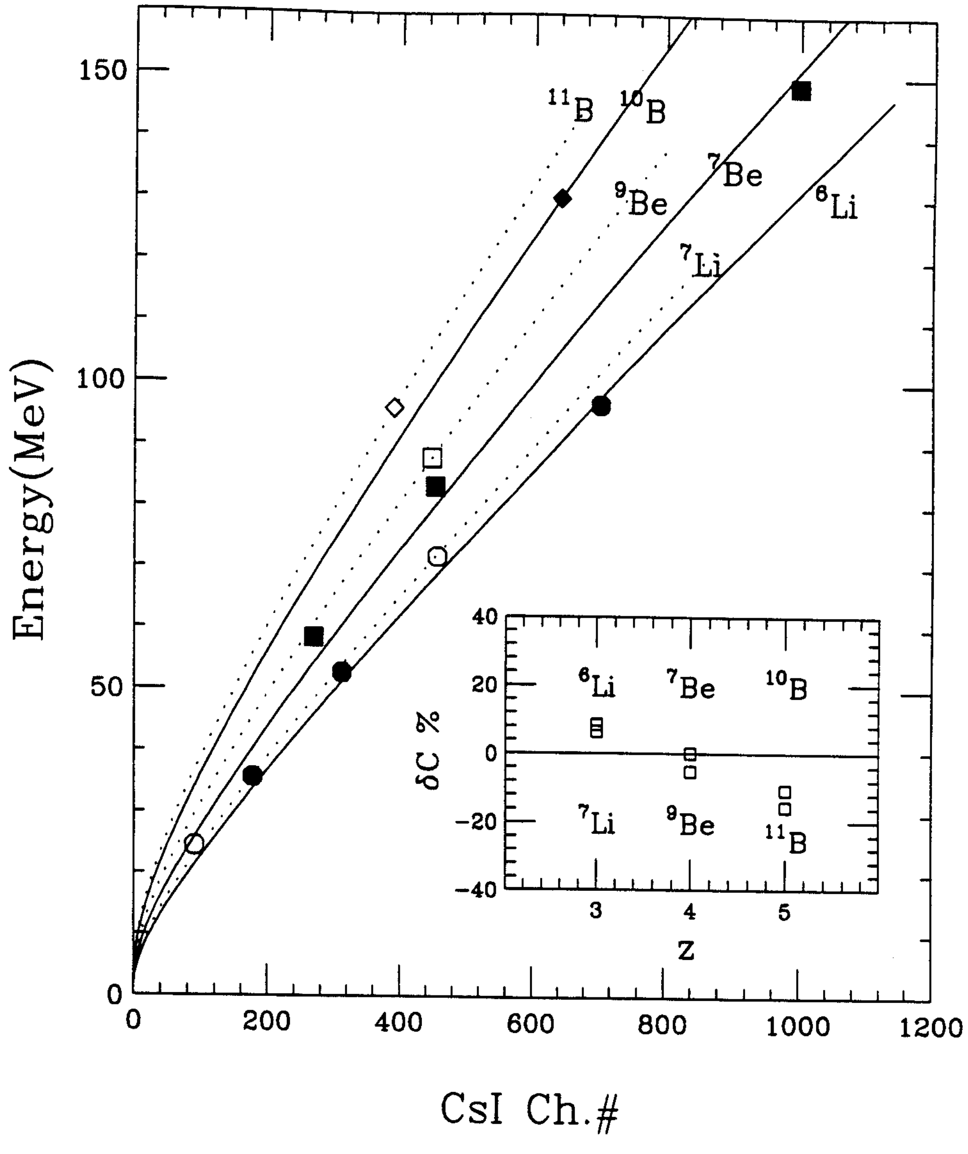

Figure 2.6: CsI(Tl) energy calibration for Li, Be, and B isotopes. The points are the calibration data and the lines are the model calculation. Inset shows the deviation of normalization constant for each particle type compared to the average.

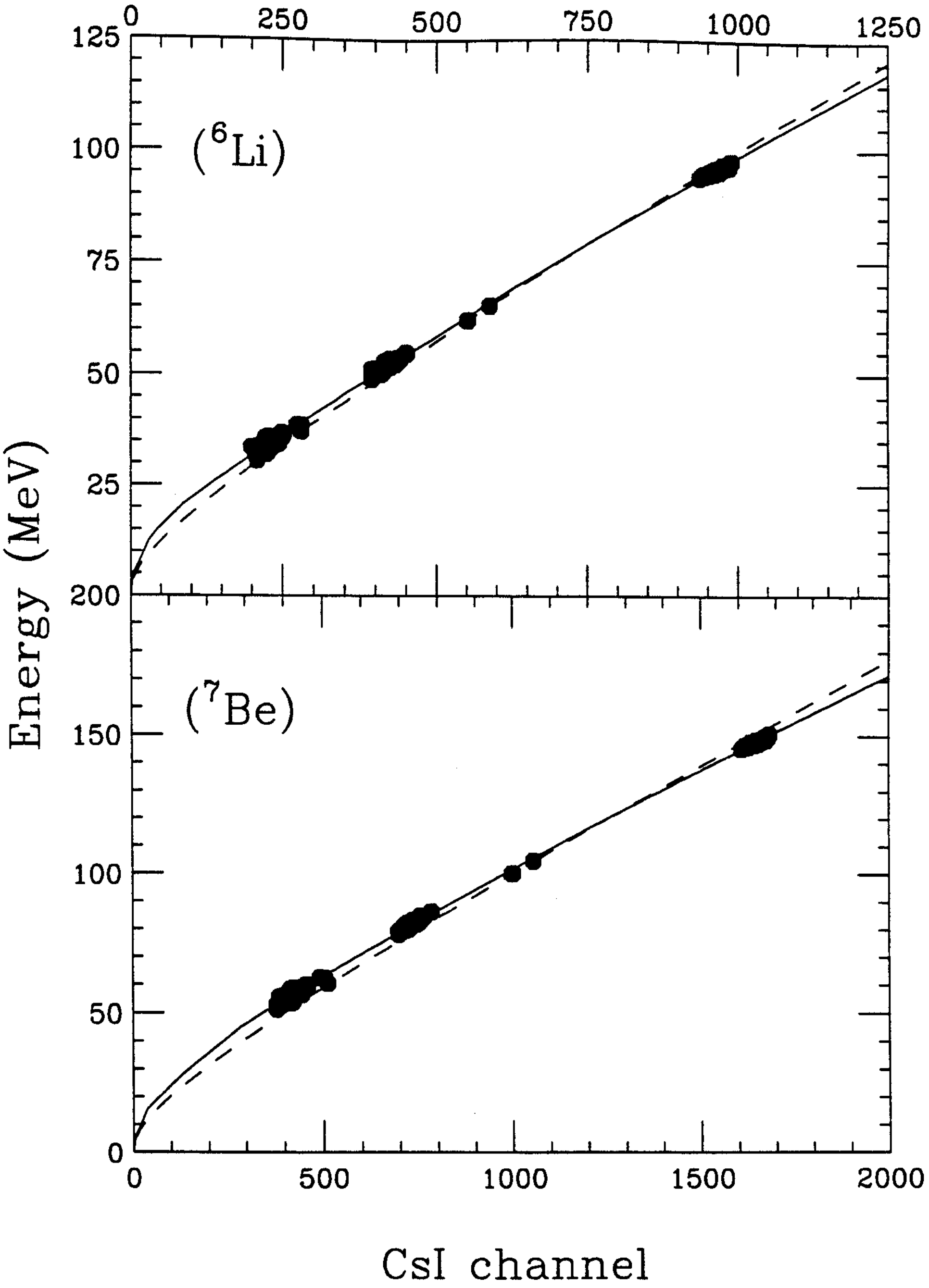

Figure 2.7: The comparison of energy correction with the calculation of CsI(Tl) energy calibration ^{6}Li and ^{7}Be. The solid points are the calibration points; the dashed lines are the model calculation; the solid lines are the calibration curves after the corrections.

^{7}Be particles (solid lines) are also shown in Fig. 2.7. The results after the correction for the CsI energy are consistent with the values for the CsI energy extracted solely from energy loss calculation using the energy losses in the silicon detectors. The energy resolution for the CsI(Tl) detectors is better than 2%.

2.3.3 Multics Array Position Calibration

To deduce the temperatures from the excited state population method, good separation between adjacent excited states is necessary to ensure the yields of decay particles from individual states can be resolved. The angle separation between neighbor telescopes is about 8°; this is certainly not good enough to resolve the peaks of different excited states. To improve the position resolution, position sensitive silicon detectors are used. The position information for these silicon detectors is obtained by means of the resistive charge division method.

For the silicon detectors we used, the positions were reconstructed from the signals collected at the four corners of a uniform continuous resistive layer on one face of the detector, while a fifth contact on the opposite face was used to determine the energy. To calibrate the silicon detectors, a perforated mask was put in front of the telescopes and the detectors were irradiated by 5.8 MeV ^{244}Cm α source at the target position, and were also irradiated by ^{12}C nuclei elastically scattered at 168 MeV. The separation between adjacent holes on the mask is 6 mm. Some of the holes were blocked on this perforated mask to provide a unique pattern for each detector for identification.

A simple analytical relationship has being given to relate the point coordinates x, y to the position signals [Brun 92]:

$$\begin{aligned} x &= \frac{q}{2}\frac{B+D-(A+C)}{A+B+C+D} \\ y &= \frac{q}{2}\frac{A+B-(C+D)}{A+B+C+D} \end{aligned} \tag{2.3}$$

Here A and B are the signals from the left and right upper contacts, C and D the ones from the left and right lower contacts and $q = 2$ is the distance between two adjacent vertices. The origin is in the center of the detector and the x and y are parallel to the sides of the detector. However, Eq. (2.3) is only a rough approximation. Top panel of Fig. 2.8 shows the position information extracted from Eq. (2.3) for a typical detector when the mask was in place and the detector was irradiated with elastically scattered Carbon particles. We can see a strong distortion of reconstructed patterns at the edge of the silicon detector.

To improve the resolution near the edge of the silicon detector, we used an analytic method developed by N. Colonna and E. Lsi [Colo 93]. based on experimental data and an analysis on the symmetries of position sensitive detectors with resistive surfaces to reconstruct the positions. The equations are:

$$\begin{aligned} &x = \frac{1}{2-l}\mu(T_A + T_C - T_B - T_D) \\ &y = \frac{1}{2-l}\mu(T_C + T_D - T_A - T_B) \\ &\alpha\mu^2 + \beta\mu + \gamma = 0 \\ &T_C - T_D + (1-l)(T_B - T_A) = 0 \end{aligned} \tag{2.4}$$

where $\alpha = \frac{1}{2-l^2}[(T_A - T_B - T_D + T_C)^2 + (T_C + T_D - T_A - T_B)^2]$, $\beta = -1 - \frac{l}{2-l^2}(T_A + T_B - T_C - T_D)$, $\gamma = 1 + (1-l)^2$. $l = 0.32$ is the length of the contact (the length of the side is 2); $T_X \propto 1/X^2$ and is normalized to the sum ($T_A + T_B + T_C + T_D = 1$); μ is the normalization

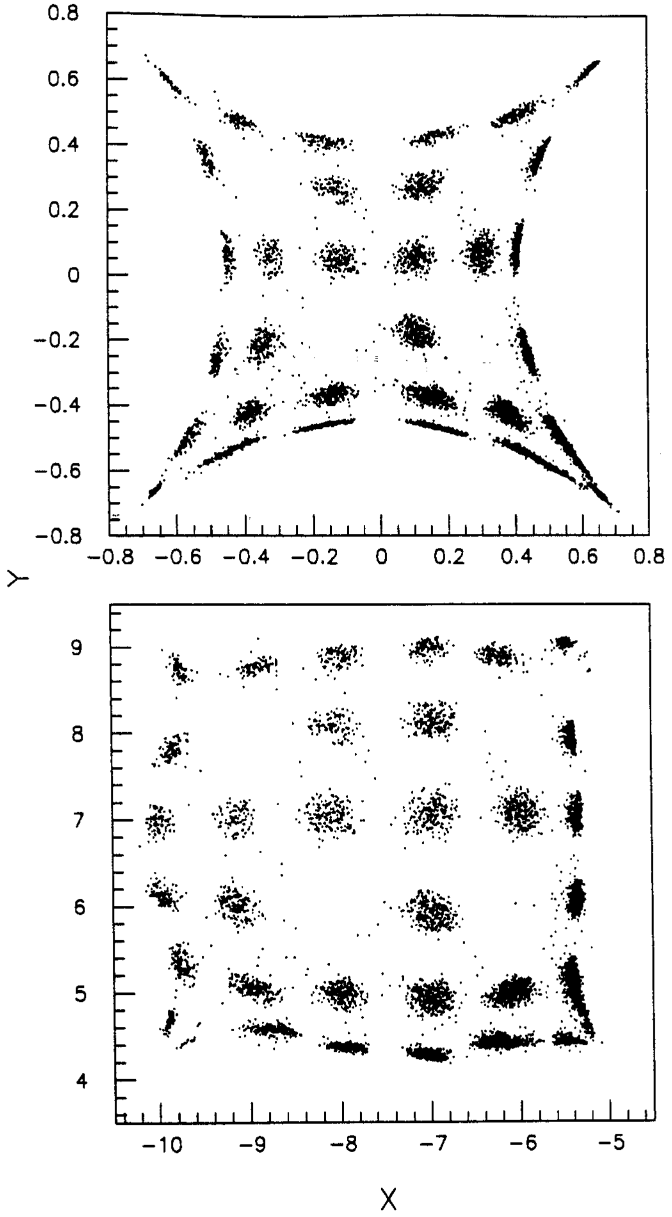

Figure 2.8: The position calibration for silicon detector 33. Top panel shows the X and Y of the mask image by using Eq. (2.3). Bottom panel shows the mask image by using the analytic method [Colo 93] and Eq. (2.5). The (0,0) is at the center of the detector on the top panel, and at the center of the mask (beam direction) on the bottom panel.

factor. The fourth equation of Eq. (2.4) represents the compatibility condition for this region. Because the experimental uncertainties, it will not in general be satisfied. The most probable incident point can be found by minimizing the χ^2 with the constraint imposed by the compatibility condition. To get x and y, μ is solved by the third equation of Eq. (2.4), but only one solution is taken as valid on the basis of the symmetry property of the four signals.

A non-linear fit to the calibration spectra was used after applying this analytic method to further correct for non-Cartesian effects:

$$\begin{aligned} X &= \sum_{0 \leq i+j \leq 3} a_{ij} x^i y^j \\ Y &= \sum_{0 \leq i+j \leq 3} b_{ij} x^i y^j \end{aligned} \tag{2.5}$$

Here x^i and y^j are the ith and the jth powers of the positions x and y obtained from Eq. (2.4). The a_{ij} and b_{ij} coefficients were obtained by fitting the expression to the absolute positions of the holes in the mask. The mask image of one typical silicon detector after correction is shown in the bottom panel of Fig. 2.8.

After energy and position calibration, the position-sensitive silicon detector in each Multics telescope provides a two dimensional angular readout with an angular resolution of 0.27° for 5.8 MeV α particles, sufficient for the measurements of excited state populations of emitted fragments. The particles stopped in silicon detectors lacked isotope resolutions and were not analyzed.

2.3.4 Particle Identification of Multics

The charge and mass information for each Multics telescope can be constructed with Si-CsI detectors. Fig. 2.9 shows a two dimensional plot of Ch_{Si} vs. Ch_{CsI} for a typical Multics detector, where Ch_{Si} and Ch_{CsI} are the channel numbers subtracted from the pedestals for Si and CsI detectors, respectively. While the particle types can be easily identified, it's difficult to get particle information directly from the two dimension plot. To make particle identification (PID) function for the Si-CsI spectrum, a simple linearization method was used to straighten the PID. First, we made two dimensional $log(Ch_{Si}) + log(Ch_{CsI})$ vs. Ch_{CsI} plot. $log(Ch_{Si}) + log(Ch_{CsI})$ instead of $log(Ch_{Si})$ was used for y-axis to improve the linearity. Second, the PID gates were drawn for each spectra and PID number was assigned for isotope. Between and beyond the element lines, PID values were assigned by interpolation or extrapolation. Fig. 2.10 shows the one dimension PID spectrum for a typical telescope. One can see the isotopes and masses are well separated by this linearization method.

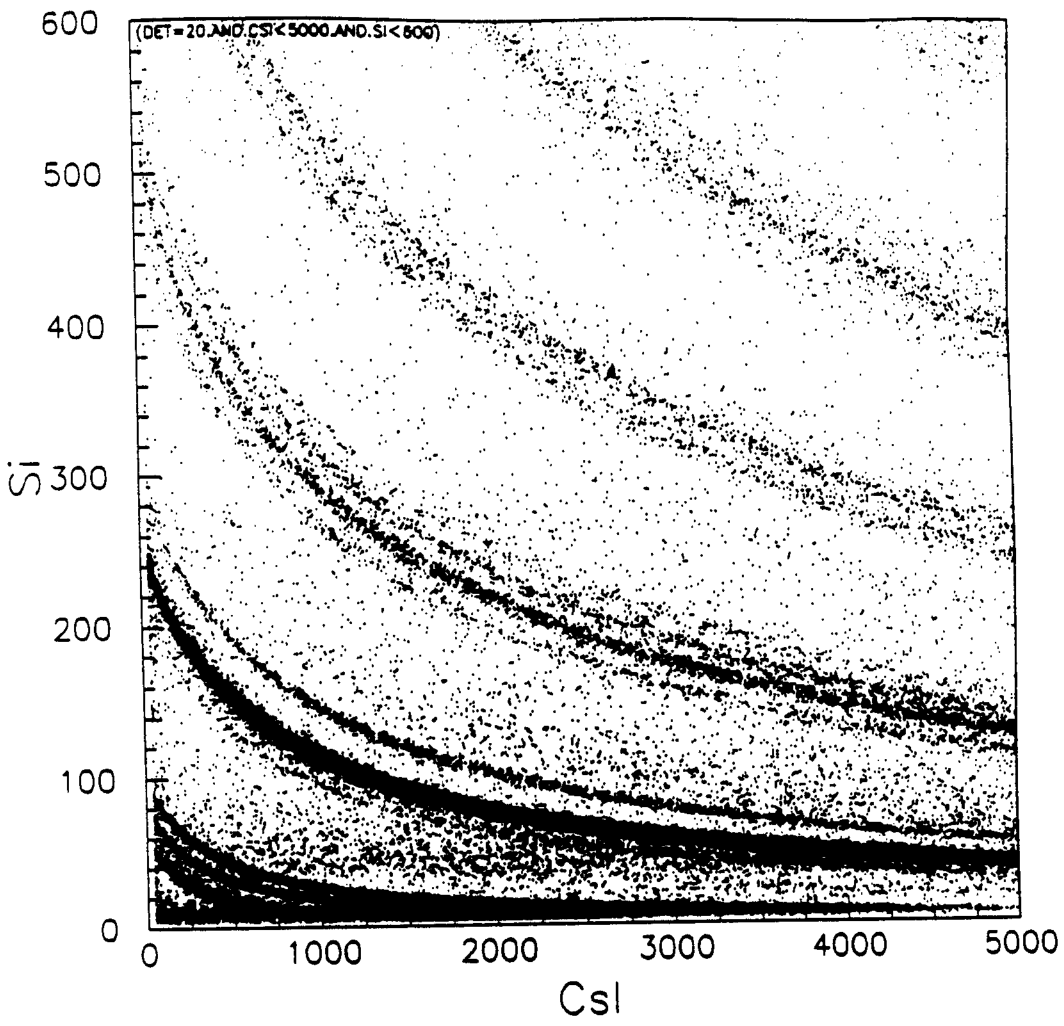

Figure 2.9: The two dimensional ΔE-E spectrum for the energy deposited in the silicon detector(vertical) vs. energy left in the CsI(Tl) detector (horizontal) for ^{197}Au + ^{197}Au 35 AMeV

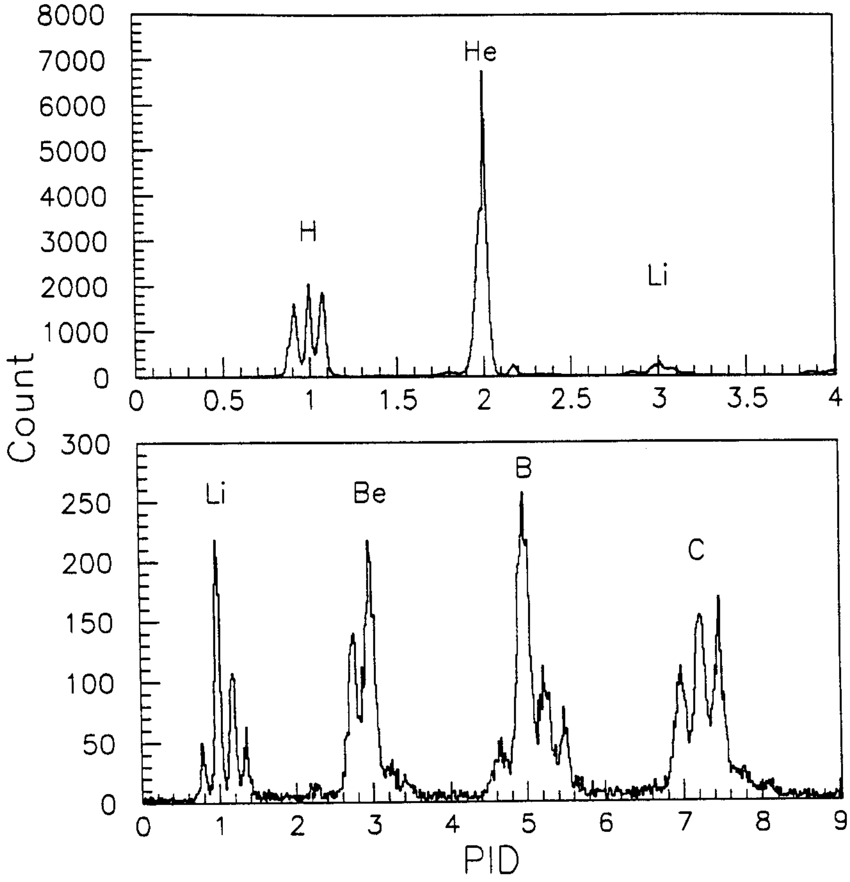

Figure 2.10: The PID 1d spectrum for H and He isotopes (upper part) and Li, Be, B and C isotopes (lower part)

Chapter 3

Nuclear Temperature Measurements

Among the most intriguing features of macroscopic systems are the phase transitions. Various models predict that a phase transition of liquid-gas characters occurs in nuclear systems at excitation energies that can be achieved in intermediate heavy ion reactions and systems that are so excited may disassemble into massive fragments. To correlate experimental observables to the thermodynamic quantities such as temperature and density, methods to measure temperature and density must be developed and established.

The concept of a nuclear temperature was originally introduced in Refs. [Beth 37] and [Weis 37]. In this picture, particles are emitted from a thermalized source and display kinetic energy spectra similar to a Maxwellian distribution with a $e^{-E/T}$ dependence on the kinetic energy E, where T is the nuclear temperature [Weis 37]. Frequently, the energy spectra of emitted intermediate mass fragments can be fitted with thermal moving-source parameterizations [West 78]. One particular simple parameterization is

$$\frac{d^2\sigma}{dEd\Omega} \propto \sqrt{(E - V_c)}e^{-E_s/T} \tag{3.1}$$

where V_c is the Coulomb barrier for fragment emission, E is the laboratory kinetic energy, $E_s = E - V_c + E_0 - 2\sqrt{E_0 - V_c} cos\theta$, $E_0 = \frac{1}{2}mv^2$, m is the mass of the detected particle, v is the velocity of the source in the laboratory frame, and θ is the angle of the emitted particle in the laboratory frame. The slope parameter T increases with increasing incident energy and can be scaled from the bombarding energy per nucleon $(E/A_{projectile})$ [Chit 86, Morr 94]. The dependence on $E/A_{projectile}$ rather than on $E/(A_{projectile} + A_{target})$ can be attributed to the localization of the thermalization to the overlap zone of the projectile and the target. A strong dependence of T on the velocity of the projectile may also reflect underlying contributions from a radial expansion of the compressed and heated matter in the region where the projectile and target overlap.

Thus, the interpretation of the slope parameter T as the temperature of an equilibrated pre-fragment may be somewhat naive. Indeed, in addition to collective expansion effects [Siem 79, Jeon 94, Hsi 95, Lisa 95], the slopes of energy spectra can be strongly affected by Fermi motion [Aich 84, Pana 84], and by the temporal evolution of the emitting system [Fiel 84, Frie 83, Stöc 81]. In practice, the temperatures extracted from the slope parameters T of the energy spectra are typically a factor of two or more higher [Morr 85, Bloc 88] than temperatures extracted from other temperature sensitive observables such as populations or isotope ratios [Chen 87, Naya 89, Kund 91, Zhu 92, Morr 94]. Transport theory calculations also support the lower temperature value of two latter techniques and disagree with the temperature extracted from energy spectra [Frie 88, Boal 89, Xu 93, Zhu 94]. Techniques to measure nuclear temperatures using excited state populations and isotope ratios are therefore utilized and will be discussed in the next two sections. The application of these techniques to extract temperatures from the Au + Au and Xe + Cu reactions will be given in the chapter 4.

3.1 Excited State Populations

If during a nuclear reaction a significant factor of the total system reaches thermal equilibrium, and one considers that the internal excitation of a nucleus can be achieved in a part of the thermalized system, the relative populations of two different states of that nucleus is given by a Boltzmann factor :

$$\frac{n_1}{n_2} = \frac{2J_1+1}{2J_2+1} exp(-\frac{\Delta E}{T_{em}}) \tag{3.2}$$

where $\Delta E = E_1^* - E_2^*$ is the difference between the excitation energies of these two states, J_i is the spin of the ith state and T_{em} is the "emission temperature" which characterizes the internal excitation energy of the system at freeze-out.

Measurements of excited state populations were initially performed for particle stable excited states. In the literature, we found such investigations for example ^{14}N + Ag collisions at 35 AMeV [Morr 84], ^{32}S + Ag collisions at 715 MeV [Xu 86], ^{58}Ni + ^{58}Ni collisions at 638 MeV [Gome 88], and ^{40}Ar + ^{12}C collisions at 320, 400, 480 MeV [Lee 90]. In such measurements, the excited state populations are deduced from measurements of γ rays in coincidence with fragments detected in their ground states. Temperature obtained from the populations of particle stable states using Eq. (3.2) can be as low as $\approx$ 1 MeV [Morr 84] due to the secondary decay of particle unstable nuclei whose populations are distorted through the feeding to the lower of the two states. To decrease the distortion from sequential decay, large values of ΔE are desired, so particle-unstable states of intermediate mass fragments with larger values of ΔE (for example, ΔE = 16.67 MeV for ^{5}Li between the 1st excited state and the ground state) are preferable for the measurements of emission temperature. Measurements of the relative yields of particle-unstable states of intermediate-mass fragments require the coincidence detection of the two daughter nuclei produced by the decay of the parent unstable nucleus. The relative energy E_{rel} of the coincidence particles in the center of mass of the parent nucleus $A \rightarrow d_1 + d_2$ can be determined from the measured energies and angles of the two daughter nuclei. The coincidence yield can then be plotted as a function of the measured excitation energy $E^*_{mea} = E_{rel} + E_b$ to obtain relative energy spectrum $Y_{tot}(E^*_{mea})$, where E_b is the the threshold energy for the parent nucleus A to decay to two daughter nuclei d_1 and d_2. The experimentally measured decay energy spectrum $Y_{tot}(E^*_{mea})$ consists of two parts,

$$Y_{tot}(E^*_{mea}) \quad = \quad Y_c(E^*_{mea}) + Y_{back}(E^*_{mea}) \tag{3.3}$$

where $Y_c(E^*_{mea})$ is the yield from the decay into channel c of the particle unstable nucleus and $Y_{back}(E^*_{mea})$ is the background from coincidences which do not originate from the decay of the parent fragment. Following the arguments of Ref. [Naya 92], the background yield $Y_{back}(E^*_{mea})$ can be approximated by

$$Y_{back} \quad = \quad C_{12}Y_1Y_2[1 + R(E_{rel})] \tag{3.4}$$

where C_{12} is a normalization constant, Y_1 and Y_2 are the single-particle inclusive yields for particles 1 and 2. The background correlation function $[1 + R(E_{rel})]$ is assumed to vanish for $E_{rel} \to 0$ and to be unity at large E_{rel} where the final state interactions are observed to negligibly influence the two particle phase space. The background correlation function can be accurately parameterized by

$$[1 + R(E_{rel})] = 1 - exp(-E_{rel}/\Delta_b) \tag{3.5}$$

where the fit parameter Δ_b is the width of the suppression of the background correlation function due to Coulomb final state interactions.

The coincidence yield $Y_c(E^*_{mea})$ can be related to a normalized excitation energy spectrum $|dn(E^*)/dE^*|_c$ in the rest frame of the unstable fragment by

$$Y_c(E^*_{mea}) = \int dE^* \epsilon(E^*, E^*_{mea}) |dn(E^*)/dE^*|_c \tag{3.6}$$

where E^* is the actual excitation energy, and $\epsilon(E^*, E^*_{mea})$ is the efficiency function. The excitation energy spectrum $|dn(E^*)/dE^*|_c$ is normalized so that $\int dE^* |dn(E^*)/dE^*|_c$ is the total yield observed in channel c divided by the observed yield of the corresponding particle stable nucleus.

The total efficiency function $\epsilon(E)$ is defined as

$$\epsilon(E) = \int dE^*_{mea} \epsilon(E^*, E^*_{mea}) \tag{3.7}$$

And the energy resolution δE^* is defined by

$$\delta E^* = \sqrt{\int dE^*_{mea} \epsilon(E^*, E^*_{mea})(E^*_{mea} - E^*)^2} \tag{3.8}$$

The efficiency function was calculated for the detector geometry of the detection array from the position and energy resolutions of the telescopes. In the efficiency calculation we assumed the particle unstable nucleus decays isotropically in its rest frame. The energy and angular distributions of the excited nucleus are assumed to be identical to those measured for the corresponding stable particle nucleus and were described by simple moving-source parameterizations (discussed in next chapter). Fig. 3.1 shows the energy resolution and the efficiency function (arbitrarily normalized) of the Multics array for the decay of ^{10}B nuclei emitted in central ^{197}Au + ^{197}Au collisions at 35 AMeV.

When stable parent nuclei exist (e.g. α and ^{10}B nuclei), these parameterizations were constrained to reproduce the experimental distributions of the stable parent nucleus. For parent nuclei with particle unstable ground states (e.g.^{5}Li), source parameters of neighboring stable nuclei (^{6}Li) were used. Because of poor position resolution at the periphery of the silicon detectors, a software cut was imposed on both the experimental data and the efficiency calculation. For light charged particles (H and He isotopes), the cut on the silicon detector is 40x40 cm^2. For other fragments, the software cut is 45x45 cm^2.

The excitation energy spectrum $|dn(E^*)/dE^*|_c$ can be obtained from measured phase shifts for the decay channels of the particle unstable nucleus of interest, and by adjusting the relative intensities for the yields from different excited states.

3.1.1 The Excitation Energy Spectrum

The two particle correlation function $R(\mathbf{q})$ can be defined as

$$\sum Y_{12}(\mathbf{p_1},\mathbf{p_2}) = C_{12}[1+R(\mathbf{q})]\sum Y_1(\mathbf{p_1})Y_2(\mathbf{p_2}) \tag{3.9}$$

where $Y_{12}(\mathbf{p_1},\mathbf{p_2})$ is the coincidence yield; $Y_i(\mathbf{p_i})$ is the single particle yield; $\mathbf{p_i}$ is the laboratory momentum of the particle i; $\mathbf{q}$ is the momentum of relative motion and is given by $\mu(\mathbf{p_2}/m_2 - \mathbf{p_1}/m_1)$ non-relativistically (μ is the reduced mass); C_{12} is the normalization

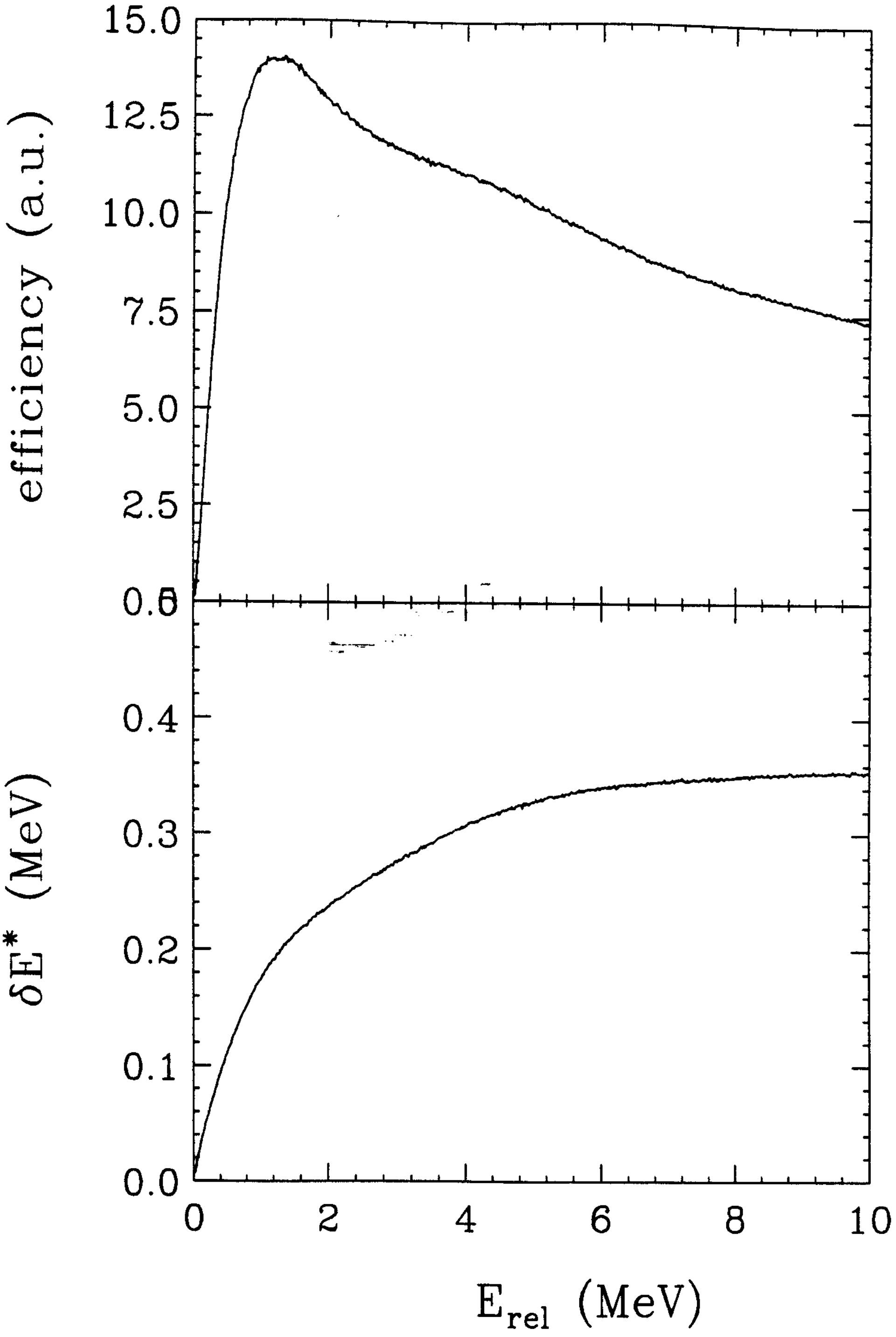

Figure 3.1: The Multics efficiency function and energy resolution calculations of detecting $^{10}B \rightarrow \alpha + {}^{6}Li$ for $^{197}Au + {}^{197}Au$ reactions at 35 AMeV

constant and is determined by $R(q) = 0$ at large relative momentum. The sums on both sides of Eq.(3.9) are extended over all energy and detector combinations corresponding to $\mathbf{q}$.

If one assumes that the two particles only interact with each other and the interaction with the rest of the system can be neglected, the two-particle density of states can be approximated as

$$\rho(p_1, p_2) \quad = \quad \rho_0(P)\rho(q) \tag{3.10}$$

Here, $\rho_0(P) = VP^2/2\pi^2$ denotes the density of states associated with the center of mass frame of these two particles, $\rho(q)$ is the density of states per unit volume in momentum space for the relative motion of the two particles. P is the total momentum of the two particles, q is the relative momentum, and V is the volume of the system. The density of states for center of mass motion $\rho_0(P)$ is not affected by the mutual interaction of these two particles. The density of states for the relative motion $\rho(q)$ can be separated to

$$\rho(q) \quad = \quad \rho_0(q) + \Delta\rho(q) \tag{3.11}$$

The non-interacting term $\rho_0(q)$ for two nuclei with spins s_i can be written as

$$\rho_0(q) \quad = \quad (2s_1 + 1)(2s_2 + 1)\frac{Vq^2}{2\pi^2} \tag{3.12}$$

And the interacting term $\Delta\rho$ can be written as [Land 80]

$$\Delta\rho(q) \quad = \quad \frac{1}{\pi}\sum_{J,\alpha}(2J + 1)\frac{\partial\delta_{J,\alpha}}{\partial q} \tag{3.13}$$

where J is the total angular momentum and $\delta_{J,\alpha}$ is the phase shift for the channel α. If the two particles are in contact with a thermal reservoir at temperature T, the phase space will be populated in accordance with the Boltzmann factor $exp(-E^*/T)$, and the single and coincidence yields can be written as

$$Y_i(p_i) \propto \rho_0(p_i)e^{-E_i/T} \qquad (i = 1,2) \tag{3.14}$$

and

$$Y_{12}(p_1,p_2) \propto \rho(P,q)e^{-(E_1+E_2)/T} \tag{3.15}$$

Combining these two expressions, the correlation function $R(q)$ can be written as

$$\begin{aligned} R(q) &= \sum \frac{Y_{12}(p_1,p_2)}{Y_1(p_1)Y_2(p_2)} - 1 \\ &= \frac{2\pi}{(2s_1+1)(2s_2+1)Vq^2}\sum_{J,\alpha}(2J+1)\frac{\partial\delta_{J,\alpha}}{\partial q} \end{aligned} \tag{3.16}$$

Within the thermal model, in which the kinetic energy distributions of emitted fragments are characterized by the same temperature as the population probabilities, and the two-particle correlation function depends inversely upon the volume of the emitting system but is independent of the temperature of the system.

Information about the temperature of the system can be obtained by the relative populations of the states. From Eq. (3.13), the population of states can then be written as

$$\begin{aligned} \frac{dn(E^*)}{dE^*} &= Ce^{-E^*/T}\Delta\rho(q) \\ &= C\sum_i e^{-E^*/T}\frac{1}{\pi}(2J_i+1)\frac{\partial\delta_{i,res}}{\partial E^*} \end{aligned} \tag{3.17}$$

Here J_i and $\delta_{i,res}$ are the spins and phase shifts of the resonances; C is a normalization constant fixed by the requirement that $\int dE^*|dn(E^*)/dE^*|_c$ is the total decay yield into channel c divided by the total yield for the corresponding particle stable nucleus.

The Boltzmann factor in the excitation energy spectra provides the necessary requirement to extract the temperature. This dependence can be more clearly illustrated if the excited states are well isolated in energy. If the phase shifts are dominated by isolated resonances and the resonances are described by a R-Matrix parameterization [Naya 92], one can write

$$\left|\frac{dn(E^*)}{dE^*}\right|_c = \sum_\lambda \left|\frac{dn_\lambda(E^*)}{dE^*}\right|_c \tag{3.18}$$

and

$$\begin{aligned}\left|\frac{dn_\lambda(E^*)}{dE^*}\right|_c &= N_\lambda e^{-E^*/T}\left(\frac{2J_\lambda+1}{\pi}\right)\frac{\Gamma_{\lambda c}/2}{(E_\lambda+\Delta_\lambda-E^*)^2+\frac{1}{4}\Gamma_\lambda^2}\\ &\times\left[1-\frac{d\Delta_\lambda}{dE^*}+\frac{E_\lambda+\Delta_\lambda-E^*}{\Gamma_\lambda}\frac{d\Gamma_\lambda}{dE^*}\right]\end{aligned} \tag{3.19}$$

Here, Γ_λ is the total width of the resonance, $\Gamma_{\lambda c}$ is the partial width ($\Gamma_\lambda = \sum_c \Gamma_{\lambda c}$), and Δ_λ is the energy shift.

For narrow states and where Γ_λ and Δ_λ depend only weakly on the energy, the decay energy spectrum can be simplified to the Breit-Wigner formula:

$$\left|\frac{dn_\lambda(E^*)}{dE^*}\right|_c = N_\lambda e^{-E^*/T}\frac{(2J_\lambda+1)}{\pi}\frac{\Gamma_\lambda/2}{(E_{res}-E^*)^2+\Gamma_\lambda^2/4}\frac{\Gamma_{\lambda c}}{\Gamma_\lambda} \tag{3.20}$$

where $E_{res} = E_\lambda + \Delta_\lambda$ is the resonance energy for the level λ.

For most cases, the excited states are sufficiently narrow so that the Boltzmann factor $e^{-E^*/T}$ varies little over the resonances. We can take this term out of the integral and define the population probability

$$n_\lambda = N_\lambda e^{-E^*/T} = N_\lambda e^{-E_{res}/T} \tag{3.21}$$

In this limit the formula describing relative populations of particle unstable nuclei is the same as that which describes the populations of particle stable states. The Breit-Wigner formula can then be written as

$$|\frac{dn(E^*)}{dE^*}|_c = \sum_{\lambda} n_\lambda \frac{(2J_\lambda + 1)}{\pi} \frac{\Gamma_\lambda/2}{(E_{res} - E^*)^2 + \Gamma_\lambda^2/4} \frac{\Gamma_{\lambda c}}{\Gamma_\lambda} \tag{3.22}$$

More details about one-level and two-level approximations of the R matrix method can be found in Ref. [Naya 92].

3.2 Isotope Double Ratios

Besides using the population of excited states method to measure nuclear temperatures, nuclear temperatures have also been recently extracted from the relative yields of different isotopes [Poch 95, Kolo 96, Tsan 96]. Through a series of measurements performed for ^{197}Au + ^{197}Au collisions at incident energy of 600 MeV/nucleon, J. Pochodzalla *et al.* [Poch 95] extracted the temperatures from He and Li isotope ratios as a function of excitation energy deposited in the projectile-like residue. A caloric curve was obtained from those isotope ratios (Fig. 3.2), which is similar to that calculated in Ref. [Bond 86]. The extracted isotope temperature remains constant at about 5 MeV for excitation energies in the range of 3 to 10 MeV/nucleon, beyond which the temperature increases linearly with excitation energy possibly indicating the onset of a vapor regime. This observation of a caloric curve qualitatively reproduces many of the essential predictions of microcanonical models [Bond 85, Bond 86, Gros 86]. The following will discuss how to extract the isotope temperatures.

In the thermodynamic picture, the density $\rho(A, Z)$ of a particle (A,Z) composed

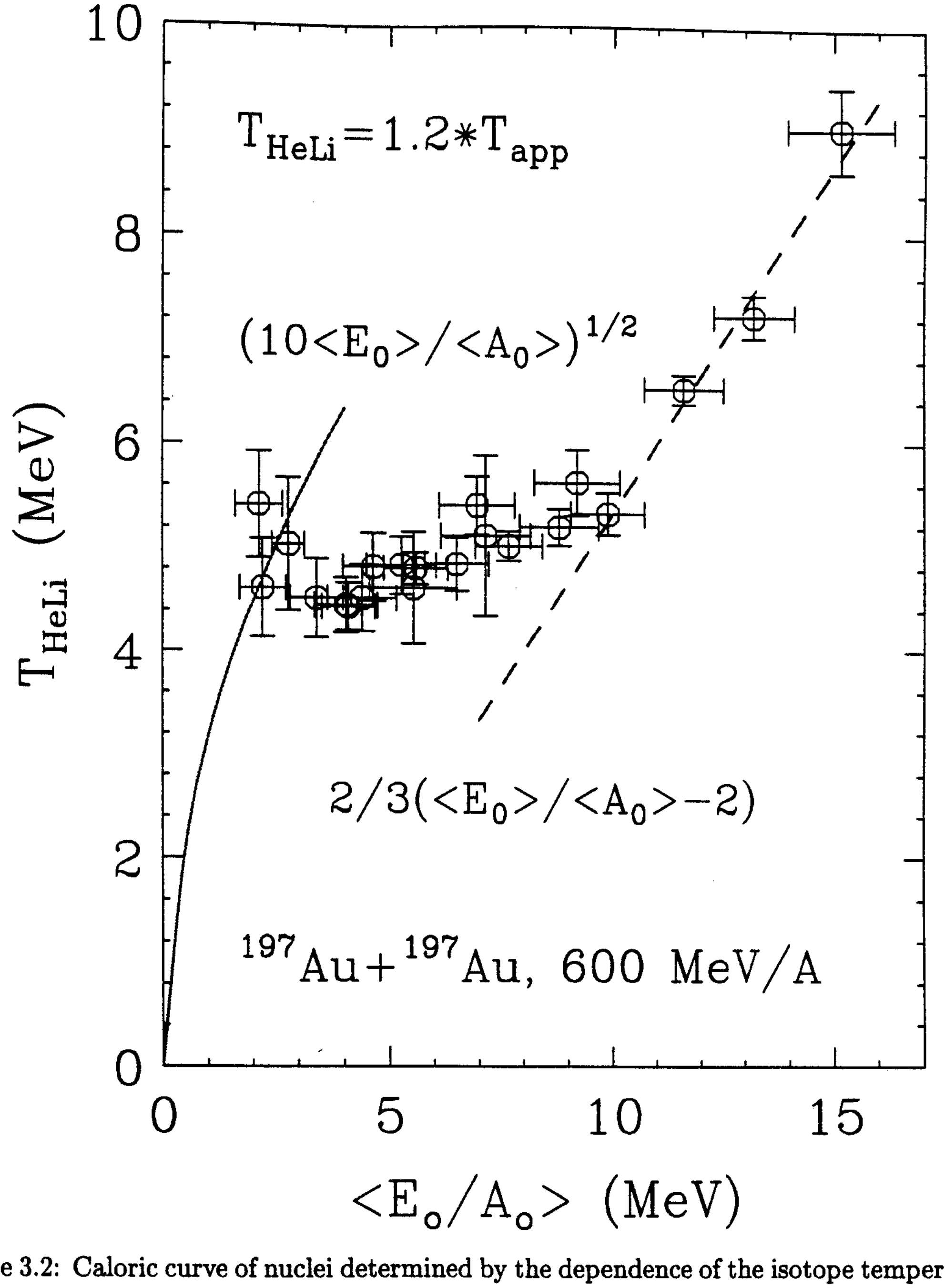

Figure 3.2: Caloric curve of nuclei determined by the dependence of the isotope temperature T_{HeLi} on the excitation energy per nucleon for Au + Au 600 AMeV. [Poch 95]

of Z bound protons and $A-Z$ bound neutrons may be expressed as follows [Albe 85]:

$$\rho(A,Z)=\frac{A^{\eta}\omega(A,Z)}{\lambda^{3}_{T_N}}F_M\left[\frac{\mu(A,Z)}{T}\right] \tag{3.23}$$

where $\lambda_{T_N}=h/(2\pi m_0 T)^{\frac{1}{2}}$ is the thermal nucleon wave-length (m_0 is the mass of a nucleon). Here, the exponent η arises from an integration over the energy spectrum and equals 1.5 in the limit of volume emission and 1.0 in the limit of surface emission, and T is the temperature expressed in MeV. $F_M[\mu(A,Z)/T]$ is proportional to $\exp[\mu(A,Z)/T]$ from Maxwell-Boltzmann statistics, and $\omega(A,Z)=\sum_j\{[2S_j(A,Z)+1]\cdot\exp[-E_j(A,Z)/T]\}$ is the internal partition function of the particle (A,Z), where $S_j(A,Z)$ are the ground state spins and $E_j(A,Z)$ are the energies of these states. $\mu(A,Z)$ is the chemical potential of the particle with nucleon number A and proton number Z. For system at chemical equilibrium, $\mu(A,Z)$ can be expressed by $\mu(A,Z)=Z\mu_{p_F}+(A-Z)\mu_{n_F}+BE(A,Z)$ where $BE(A,Z)$ is the binding energy of the cluster (A,Z), μ_{p_F} and μ_{n_F} are the chemical potentials of free protons p_F and of free neutrons n_F, respectively.

From Eq. (3.23) , the ratio $Y(A,Z)/Y(A',Z')$ between the experimental yields of two different emitted fragments is expected to be

$$\begin{aligned}\frac{Y(A,Z)}{Y(A',Z')}&=\frac{\rho(A,Z)}{\rho(A',Z')}\\&=\left(\frac{A}{A'}\right)^{\eta}\left(\frac{\lambda^{3}_{T_N}}{2}\right)^{A-A'}\frac{\omega(A,Z)}{\omega(A',Z')}\rho_{p_F}^{Z-Z'}\rho_{n_F}^{(A-Z)-(A'-Z')}e^{\frac{BE(A,Z)-BE(A',Z')}{T}}\end{aligned} \tag{3.24}$$

For an isotope pair (A,Z) and $(A+1,Z)$ and if only ground states of particles are considered, Eq.(3.24) can be approximated as:

$$\frac{Y(A,Z)}{Y(A+1,Z)}=\left(\frac{A}{A+1}\right)^{\eta}\left(\frac{2}{\lambda^{3}_{T_N}}\right)\frac{2S(A,Z)+1}{2S(A+1,Z)+1}\rho_{n_F}^{-1}e^{\frac{BE(A,Z)-BE(A+1,Z)}{T}} \tag{3.25}$$

in which the free proton chemical potential ρ_{p_F} is canceled out.

Temperatures can then be extracted from double ratios of isotope yields differing by one neutron to cancel the free neutron chemical potential ρ_{n_F}, and one obtains:

$$T = \frac{B}{\ln(aR_{iso})} \tag{3.26}$$

where

$$\begin{aligned}
R_{iso} &= \frac{Y(A_i, Z_i)/Y(A_i+1, Z_i)}{Y(A_j, Z_j)/Y(A_j+1, Z_j)} \\
a &= \frac{[2S(A_j, Z_j)+1]/[2S(A_j+1, Z_j)+1]}{[2S(A_i, Z_i)+1]/[2S(A_i+1, Z_i)+1]} \left[\frac{A_j/(A_j+1)}{A_i/(A_i+1)}\right]^{\eta} \\
B &= BE(A_i, Z_i) - BE(A_i+1, Z_i) - BE(A_j, Z_j) + BE(A_j+1, Z_j)
\end{aligned}$$

3.3 Sequential Decay Calculation

Consistency between suitable thermometers provides an important test of the degree of thermalization achieved in a reaction. Temperatures determined from relative populations of states and double isotope ratios, however, often differ from one set of isotopes or pair of excited states to another [Kolo 96, Tsan 96, Tsan 96a, Huan 97]. While these variations may sometimes reflect non-equilibrium processes [Gutb 89, Wile 92, Phai 93a], calculations have shown that the perturbations of the distributions can arise from final-state interactions among the emitted particles [Boal 84], and/or feeding from higher-lying states [Morr 84, Morr 85, Poch 85, Xu 86, Bloc 87, Fiel 87, Hahn 87, Poch 87]. Perturbations due to final-state interactions are difficult to assess since they depend on the detailed space-time evolution of the final stages of the reaction [Boal 84]. It's often assumed that they are small compared to those caused by sequential feeding. In general, the resulting uncertainties for temperatures extracted from excited state populations are expected to be smaller when ΔE

is much larger than the temperature T, of the emitting source [Poch 85]. For temperatures determined by isotope ratios, however, the uncertainties can be large. Thus it is important to develop a model which can be used to extract the freeze out temperatures from the apparent temperatures.

In principle, the ideal test of a thermal model should have a direct comparison of the model prediction to the measured excited state population or isotope ratios. Unfortunately, most statistical models lack a description of the secondary decay process at the necessary level of detail. Furthermore, all predictions of a thermal equilibrium description of the fragmentation process are determined by three parameters T, ρ, and the charge to mass ratio Z/A of the thermalized system. Measurements of the charge distribution are enough to constrain the temperature of the emitting system and if the predicted isotope or excited state ratios then disagree with the experimental ones, there is little freedom in such models to probe further. Here, we attempt to decouple these observables by constructing a thermal model with sufficient detail to describe the secondary decay of excited fragments and with enough flexibility to describe the charge distribution as well. Then we perform a back tracing procedure from the data to extract the temperature at freeze-out.

Assuming the particles are emitted at freeze-out by a thermalized source of neutron number N_i, charge number Z_i, spin J_i, the initial population of an excited state of an emitted nucleus with excitation energy E_i^*, and the temperature T_{em}, the initial population of these particles can be approximated by the expression:

$$P_i(N_i, Z_i, J_i, E_i^*, T_{em}) \propto P_0(A_i, Z_i) \exp(-E_i^*/T_{em}) \exp(-t_b/t_i) \qquad (3.27)$$

where $P_0(A_i, Z_i)$ is the probability of populating the nucleus with mass number A and charge number Z at its ground state. The factor $\exp(-t_b/t_i)$ takes pre-breakup cooling effects into account and t_i is the mean lifetime of the emitted fragment calculated according to the Weisskopf model [Weis 37] for statistical decay; t_b is the breakup time scale and is chosen to be 100 fm/c [Xi 96].

In this backtracing procedure, the population probability is parametrized as:

$$P_0(A_i, Z_i) \propto \exp\left(-\frac{V_i}{T_{em}} + \frac{Q_i}{T_{em}}\right) \exp\left(-\frac{Z_i\mu_p + N_i\mu_n}{T_{em}}\right) \tag{3.28}$$

The general form of Eq. (3.28) can be obtained from either statistical evaporation theory or from grand-canonical treatments. The present formula therefore has the flexibility to be applied over a wide range in excitation energy.

The Coulomb barrier V_i is parameterized by

$$V_i = \frac{Z_i(Z_p - Z_i)e^2}{r_0[A_i^{1/3} + (A_p - A_i)^{1/3}]} \tag{3.29}$$

where A_p, Z_p are the total mass and charge number of the fragmenting system and $r_0 =$ 1.2 fm. $-Q_i$ is the separation energy of the ground state:

$$Q_i = B(A_p - A_i, Z_p - Z_i) + B(A_i, Z_i) - B(A_p, Z_p) \tag{3.30}$$

where the binding energy of the emitting source was parameterized by the empirical Weizsacher formula $B(A_i, Z_i) = C_0A_i - C_1A_i^{2/3} - C_2\frac{Z_i^2}{A_i^{1/3}} - C_3\frac{(A_i-2Z_i)^2}{A_i}$ was with $C_0 = 14.1$ MeV (volume term), $C_1 = 13.0$ MeV (surface term), $C_2 = 0.595$ MeV (Coulomb term), and $C_3 =$ 19.0 MeV (paring term) [Marm 69]. The binding energies of emitted fragments were taken to be given by their measured values.

In Eq. (3.28), the chemical potentials μ_p (proton) and μ_n (neutron) were not fixed by a requirement that the average charge and mass were conserved and were treated as free parameters to reproduce the experimental charge distributions. Reproduction of the measured charge distributions is particularly important since calculated charge distributions that are too steep (too shallow) will under-predict (over-predict) the secondary feeding corrections.

Since the spins, isospins and parities of many low-lying particle bound and unbound levels of nuclei with $Z \leq 11$ are known, the information for these nuclei could be used in the sequential decay calculation. The level density of known discrete states [Endt 78, Ajze 88] for $Z \leq 11$ with excitation energy E^* and spin J up to excitation energy ϵ_0 is:

$$\rho(E^*, J) = \sum_i \delta(E_i - E^*)\delta_{J,J_i}; \quad E^* \leq \epsilon_0 \tag{3.31}$$

At higher excitation energies, $\epsilon_0 < E^* \leq E^*_{max}$, where not all states are known in detail, a continuum approximation [Gilb 65] was used:

$$\rho(E^*, J) = \frac{(2J+1)\exp([a(E^* - E_0)]^{1/2})}{24\sqrt{2}a^{1/4}\sigma^3(E^* - E_0)^{5/4}} \exp\left[-(J + \frac{1}{2})^2 / 2\sigma^2\right]; \; \epsilon_0 < E^* \leq E^*_{max} \tag{3.32}$$

Here, $a = A/8 \; MeV^{-1}$ is the level density parameter, $E^*_{max} = \epsilon^*_{max} \cdot A$ is the cut off parameter in the excitation energy employed to save the computing time, and σ is the spin cutoff parameters with the relation [Gilb 65]:

$$\sigma^2 = 0.0888[a(E^* - E_0)]^{(1/2)} A^{2/3} \tag{3.33}$$

For each isotope, the matching energy ϵ_0 was chosen as the location of the maximum of the density. For illustration, the histogram of known level density of ^{20}Ne states is plotted in Fig. 3.3 [Chen 88]. $\epsilon_0 = 13$ MeV was chosen because at the energy $E_x \geq 13$ MeV, the level density decreases with E^*. The curve in Fig. 3.3 was calculated from Eq. (3.32). The

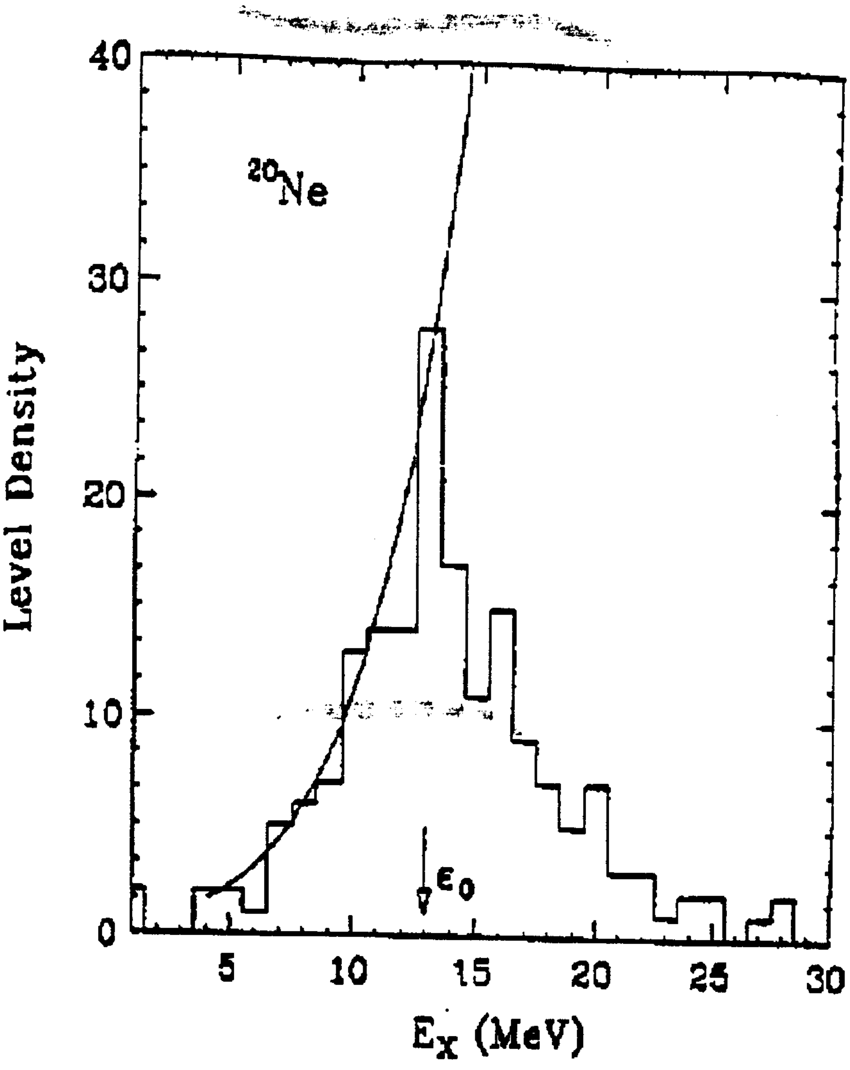

Figure 3.3: The level density of ^{20}Ne plotted as a function of its excitation energy. The histogram shows the number of known levels binned in excitation energy. The curve is the level density calculation with Eq. (3.32) [Chen 88].

energy E_0 is determined by the normalization condition:

$$\int_{E_0}^{\varepsilon_0} dE^* \int dJ \rho(E^*, J) = \int_0^{\varepsilon_0} dE^* \{\sum_i \delta(E_i - E^*)\} \tag{3.34}$$

For nuclei of charge $12 \leq Z \leq 20$ where the low lying states are unknown, a continuum approximation to the level density was used over the entire range of excitation energies. At low excitation energies where $E^* \leq \epsilon_0$, the interpolation formula from ref. [Gilb 65] was modified to include a spin dependence [Chen 88]:

$$\rho(E^*, J) = \frac{1}{T} exp\left[\frac{(E^* - E_1)}{T}\right] \frac{(2J+1)exp[-(J+1/2)^2/2\sigma^2]}{\sum(2J+1)exp[-(J+1/2)^2/2\sigma^2]};\ E^* \leq \epsilon_0 \tag{3.35}$$

where σ was calculated from Eq. (3.33) at $E^* = \epsilon_0$ and was assumed to be constant for $E^* \leq \epsilon_0$; ϵ_0, T, and E_1 were taken from Eq. (3.33).

Each decay was then calculated by using tabulated branching ratios where available [Ajze 88] and from Hauser-Feshbash formula [Haus 52] when such information is unavailable. Unknown spins and parities of tabulated discrete states were randomly assigned in these calculations [Naya 92, Xu 89, Zhu 95] and then changed in subsequent calculations to assess the corresponding uncertainties.

Chapter 4

Temperature Measurements for 35 AMeV Au + Au Reactions and 30 AMeV Xe + Cu Reactions

4.1 Introduction

During the time evolution of a violent central nuclear collision, the various degrees of freedom of the system evolve toward equilibrium at different rates. The utility of the thermal model prediction for any observable depends on the similarity of the average over ensemble of final decay configurations to an average of over a comparable thermal ensemble. This can be tested by comparing theoretical predictions with experimental measurements of a wide range of thermal sensitive observables.

For the liquid-gas phase transition, it is more relevant to investigate systems where local chemical equilibrium is achieved than to attempt a more restrictive constraint requiring both chemical and kinetic equilibrium. Due to the excitation of large scale radial or rotational collective motion during the early stages of the collision, and the role of such motion plays in hastening the breakup, the damping of collective motion into thermal motion is only rarely achieved. Chemical equilibrium, on the other hand, mainly requires local rearrangements of the nucleons and therefore can proceed more rapidly. Furthermore, it is primarily chemical equilibrium that is required for fragment charge distributions and multiplicity distributions to be consistent with thermal models. Thermometers that test chemical equilibrium can provide information about chemical temperatures and are therefore most important for investigations of multifragmentation and the liquid-gas phase transition.

In this chapter, temperatures are extracted from excited state populations and isotope ratios from Au + Au collisions at E/A = 35 MeV and Xe + Cu collisions at E/A = 30 MeV. The first experiment provides information about chemical temperatures achieved in a multifragment final state which other measurements have suggested local equilibrium is reached in this incident energy. The second experiment provides an opportunity to test a transport model that predicts the temperature of reaction residue to be intimately linked to the low density nuclear equation of state.

4.2 Impact Parameter Determination and Central Collisions

Nuclear temperatures have been measured for more than a decade with inclusive measurements [Song 83, Hils 87, Chen 87, Xu 89, Kund 91, Naya 92]. While providing some indication of the overall thermal energy per nucleon, interpretations of inclusive measurements are complicated by the implicit average over impact parameter which makes it difficult to unravel the complex interplay between statistical and dynamical effects. More precise measurements can be performed with 4π detector arrays at different impact parameter gates [Bade 82, West 85, deSo 90, Gobb 93]. The sensitivity of the observables like the charged particle multiplicity to the impact parameter can be used to select the impact parameter [Gust 84, Stöc 86, Tsan 89, Cava 90, Bowm 91, deSo 91, Phai 92].

The measured charged particle multiplicity distributions (N_C) in Miniball detectors for 35 AMeV ^{197}Au + ^{197}Au collisions (top panel) and 30 AMeV ^{129}Xe + ^{nat}Cu collisions (bottom panel) are shown in Fig. 4.1. The distributions exhibit a rather structureless plateau and a near exponential falloff at the highest multiplicities. Using a monotonic relationship between the charged particle multiplicity and the impact parameter allows one to assign a corresponding "reduced impact parameter" $\hat{b}$ to each value according to the N_C. The relation is:

$$\hat{b} = \frac{b}{b_{max}} = \left[\int_{N_C(b)}^{\infty} dN_C \cdot P(N_C) \right]^{1/2} \tag{4.1}$$

Here, $P(N_C)$ is the probability distribution for detecting the N_C charged particles and b_{max} is the impact parameter where $N_C = 3$. The reduced impact parameter assumes values of $\hat{b} = 0$ for the most central collisions and $\hat{b} = 1$ for the most peripheral collisions.

Ideally, measurements of central collisions should be performed subject to a restrictive gate on the impact parameter. At first glance, a tight gate might appear feasible because particle multiplicities increase significantly as the impact parameter is reduced. This trend makes it possible to exclude very large impact parameters. At smaller impact parameters, however, the impact parameter sensitivity is insufficient to overcome the lin-

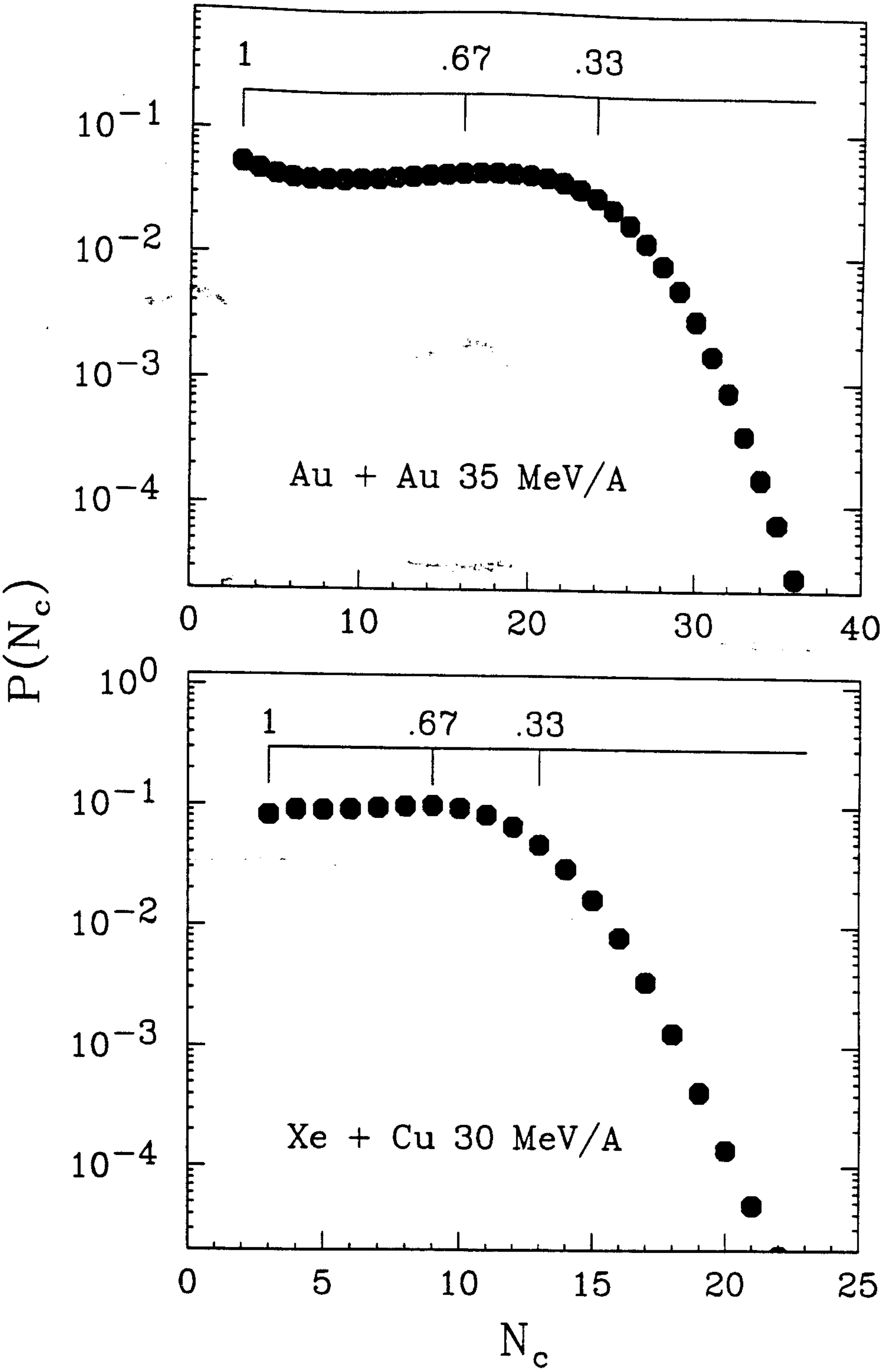

Figure 4.1: Charged particle distributions for Au + Au (top panel) and Xe + Cu (bottom panel) reactions. The reduced impact parameter $\hat{b} = b/b_{max}$ is indicated at the tops of both panels where b_{max} is the impact parameter corresponding to $N_C = 3$.

ear decrease of the reaction cross section $\Delta\sigma = 2\pi b\Delta b$ with decreasing impact parameter. The folding of impact parameter dependence of the particle multiplicity against the linear dependence of the reaction cross section means that the measurement of differential multiplicities with a high statistical accuracy is most easily achieved over a somewhat narrow range of impact parameters.

The impact parameter selected coincidence ^{6}Li - α and d - ^{3}He yields relevant to excited state populations are shown in Fig. 4.2 and follow trends consistent with these general expectations. Due to the low beam intensity achieved during this experiment, it was necessary to employ rather broad gates. The central collisions are hence defined as $\hat{b} < 0.45$ ($N_c > 21$) for Au + Au collisions and $\hat{b} < 0.6$ ($N_c > 9$) for Xe + Cu collisions. Conversely, peripheral collisions in this experiment are defined as $\hat{b} > 0.45$ ($N_c \leq 21$) for Au + Au collisions and $\hat{b} > 0.6$ ($N_c \leq 9$) for Xe + Cu collisions.

4.3 Particle Singles Cross Section

Fig. 4.3 and Fig. 4.4 show the energy spectra of selected isotopes for Au + Au reactions at central collisions and peripheral collisions, respectively. Fig. 4.5 and Fig. 4.6 show the energy spectra of selected isotopes for Xe + Cu reactions at central collisions and peripheral collisions, respectively. All the energy spectra shown from Fig. 4.3 to Fig. 4.6 display maxima at energies that correspond to the Coulomb barrier for emission from a projectile like residue, but at higher energies the spectra decrease exponentially. Previous investigations [Chit 86a, Bowm 92, Phai 92] have shown that such energy spectra can be

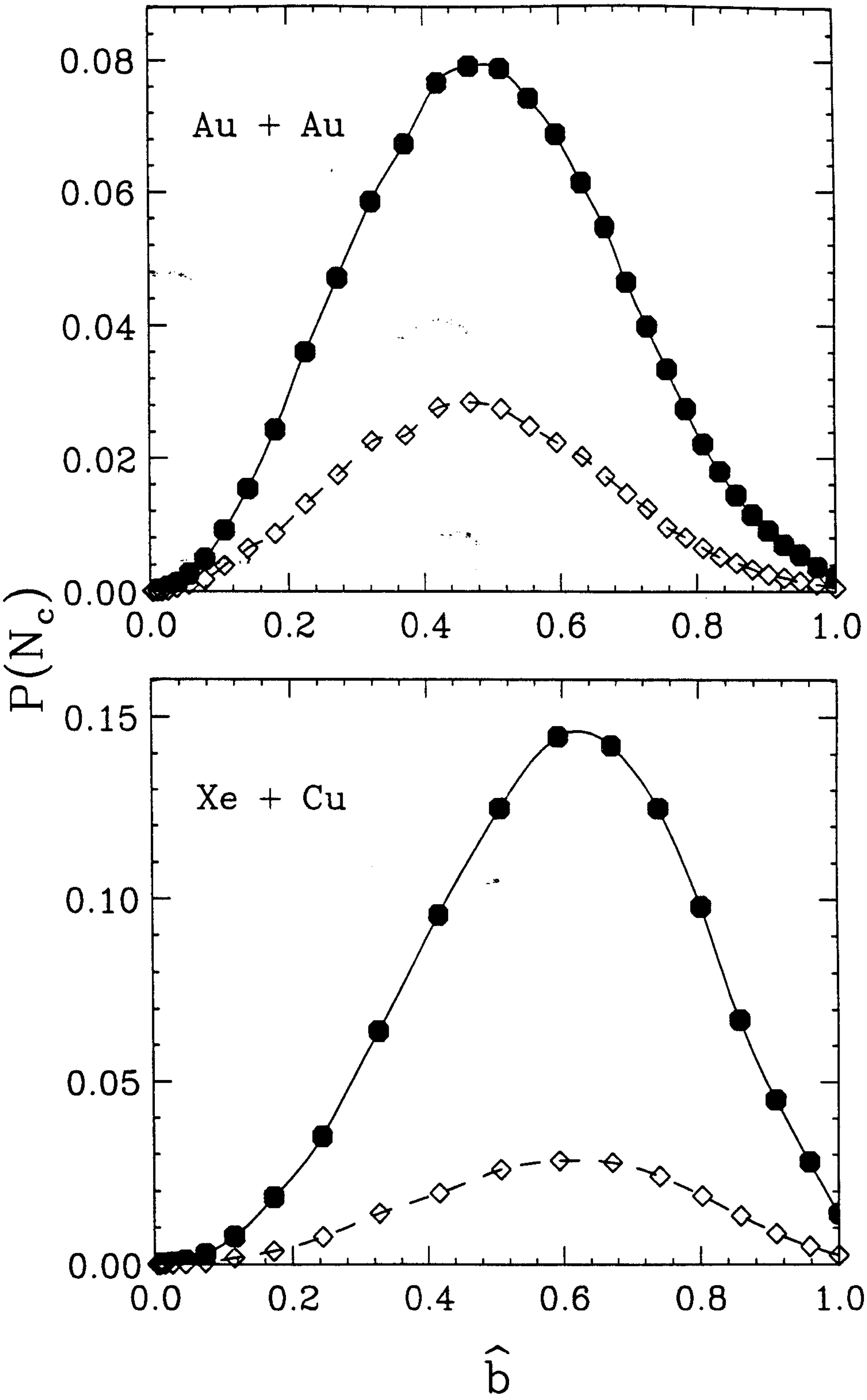

Figure 4.2: The probabilities of coincidence yields as a function of reduced impact parameter ($\hat{b}$) for Au + Au (top panel) and Xe + Cu (bottom panel) reactions. The solid points are the α - ^{6}Li pairs and the open squares are the d - ^{3}He pairs. The probability is normalized to the total counts of α - ^{6}Li pairs. The lines are drawn to guide the eyes.

fitted with relativistic Maxwellian distributions [Land 80, Hsi 94] (in this case three):

$$\begin{aligned}\frac{dP^2(\vec{p})}{dEd\Omega} &= \sum_{i=1}^{3}\frac{dP_i^2(\vec{p})}{dEd\Omega} \\ &= \frac{dP_1^2}{dEd\Omega}(\vec{p},\vec{v}_1,V_1) + \int_0^{2\pi}\frac{d\phi_R}{2\pi}\sum_{i=2}^{3}\frac{dP_i^2}{dEd\Omega}(\vec{p}_i,\vec{v}_i(\phi_R),V_i) \qquad (4.2)\end{aligned}$$

where the subscript 1 is the participant source, the subscripts 2 and 3 are the projectile like and target like sources, E and $\vec{p}$ denote the kinetic energy and momentum of the emitting particle, $\vec{v}_i$ denotes the velocity, V_i denotes the effective Coulomb barrier of the ith source, and ϕ_R denotes the azimuthal angle of the reaction plane. Here, $dP_i^2/dEd\Omega(\vec{p},0,V_i)$ is defined in the rest frame of the source ($\vec{v}_i \equiv 0$) by

$$\begin{aligned}\frac{dP_i^2}{dEd\Omega}(\vec{p},0,V_i) &= a_i\Theta(E-V_i)(E+mc^2-V_i) \\ &\times \sqrt{(E+mc^2-V_i)^2-m^2c^4}\,\exp(-\frac{E-V_i}{T_i}) \qquad (4.3)\end{aligned}$$

and $dP_i^2/dEd\Omega(\vec{p},\vec{v}_i,V_i)$ is obtained from Eq. (4.3) by Lorentz transformation. In Eq. (4.3), a_i is a normalization constant, T_i is a temperature parameter, $\Theta(E-V_i)$ is the unit step function, and m is the mass of emitting particle. Because of the mass symmetry of Au + Au collisions, $\vec{v}_3 = -\vec{v}_2$, $a_3 = a_2$, and $T_3 = T_2$ are stringently required in the c.m. frame for the spectator sources for Au + Au collisions.

To include a collective radial flow in the participant source, a radial expansion, $\vec{v}(\vec{r}) = c\beta_{exp}\vec{r}/R_S$, was assumed which attains its maximum velocity $c\beta_{exp}$ at the surface $r = R_S$. The velocities of individual particles were assumed to be thermally distributed with temperature T_1 about the local radial expansion velocity. Coulomb expansion after breakup was modeled in the limit of large β_{exp}, i.e., particles with charge Z_f, emitted from a source with charge Z_S, were assumed to gain a kinetic energy $\Delta E_{Coul}(r) = Z_f(Z_S - Z_f)e^2r^2/R_S^3$,

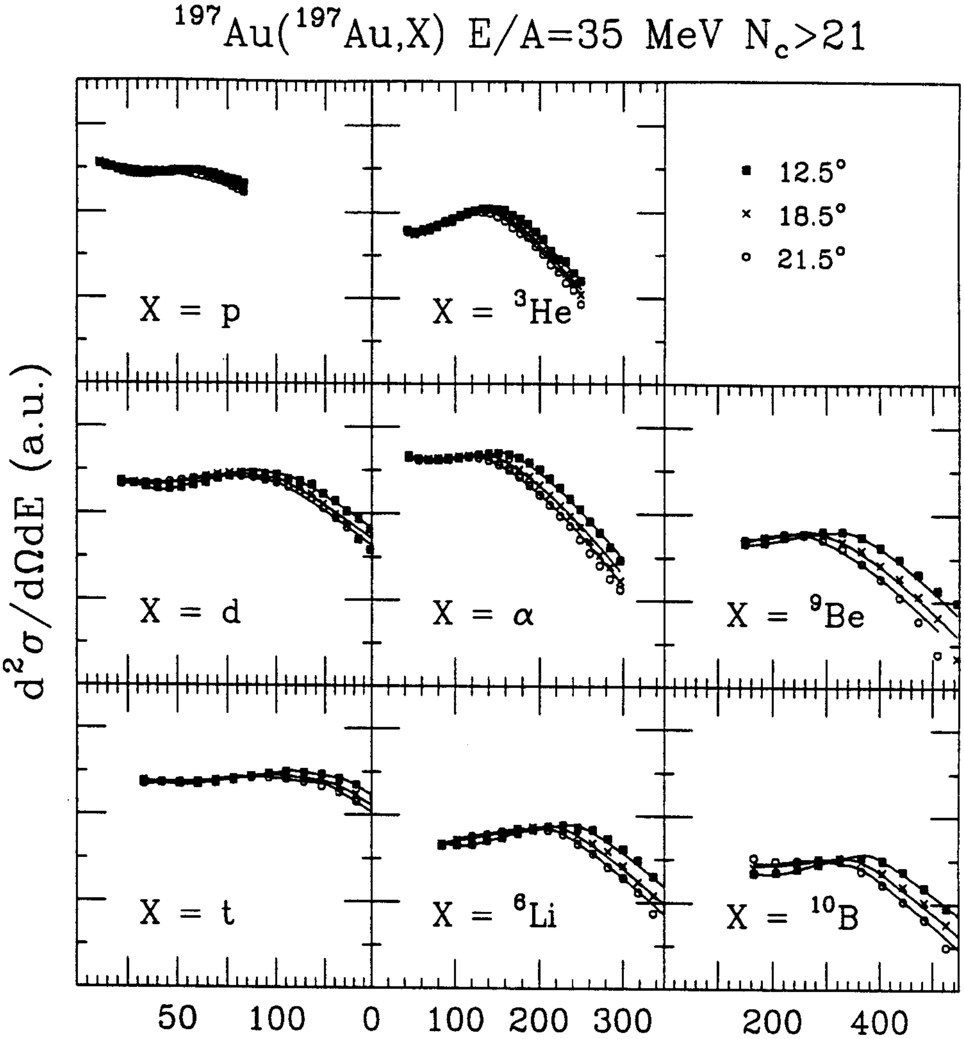

Figure 4.3: Single particle cross sections for p, d, t, ^{3}He, ^{4}He, ^{6}Li, ^{9}Be, and ^{10}B emitted at 35 AMeV ^{197}Au + ^{197}Au central collisions. The curves are the corresponding moving source fits using Eq. 4.2.

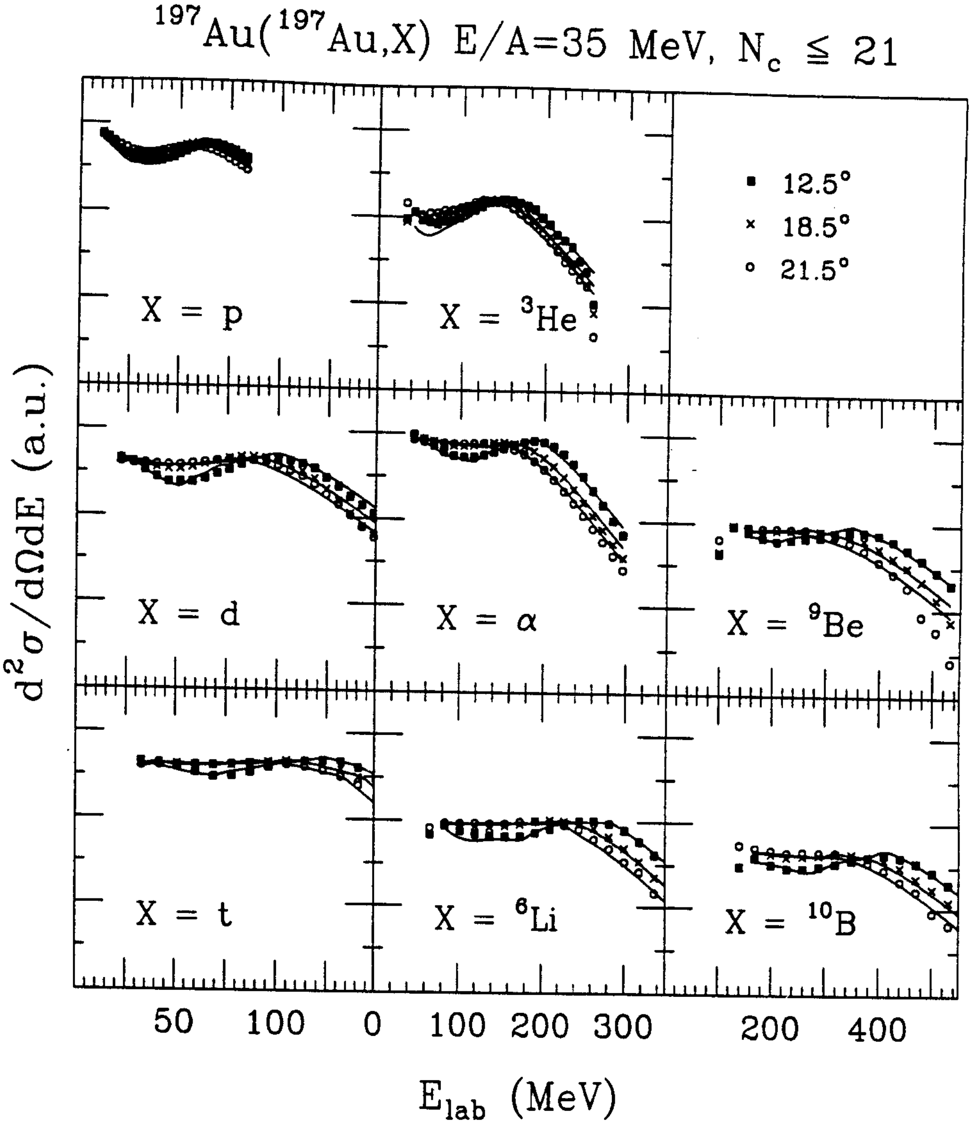

Figure 4.4: Single particle cross sections for p, d, t, ^{3}He, ^{4}He, ^{6}Li, ^{9}Be, and ^{10}B emitted at 35 AMeV ^{197}Au + ^{197}Au peripheral collisions. The curves are the corresponding moving source fits using Eq. 4.2.

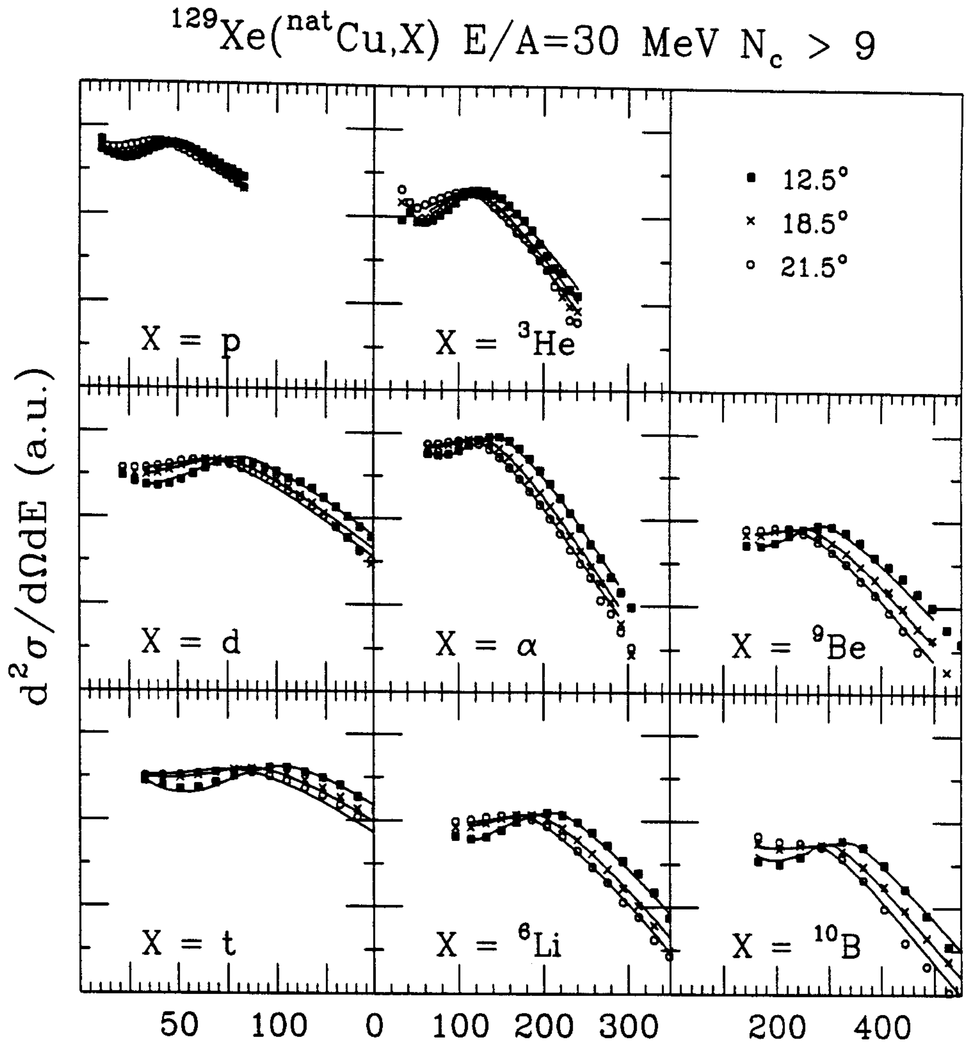

Figure 4.5: Single particle cross sections for p, d, t, ^{3}He, ^{4}He, ^{6}Li, ^{9}Be, and ^{10}B emitted at 30 AMeV ^{129}Xe + ^{nat}Cu central collisions. The curves are the corresponding moving source fits using Eq. 4.2.

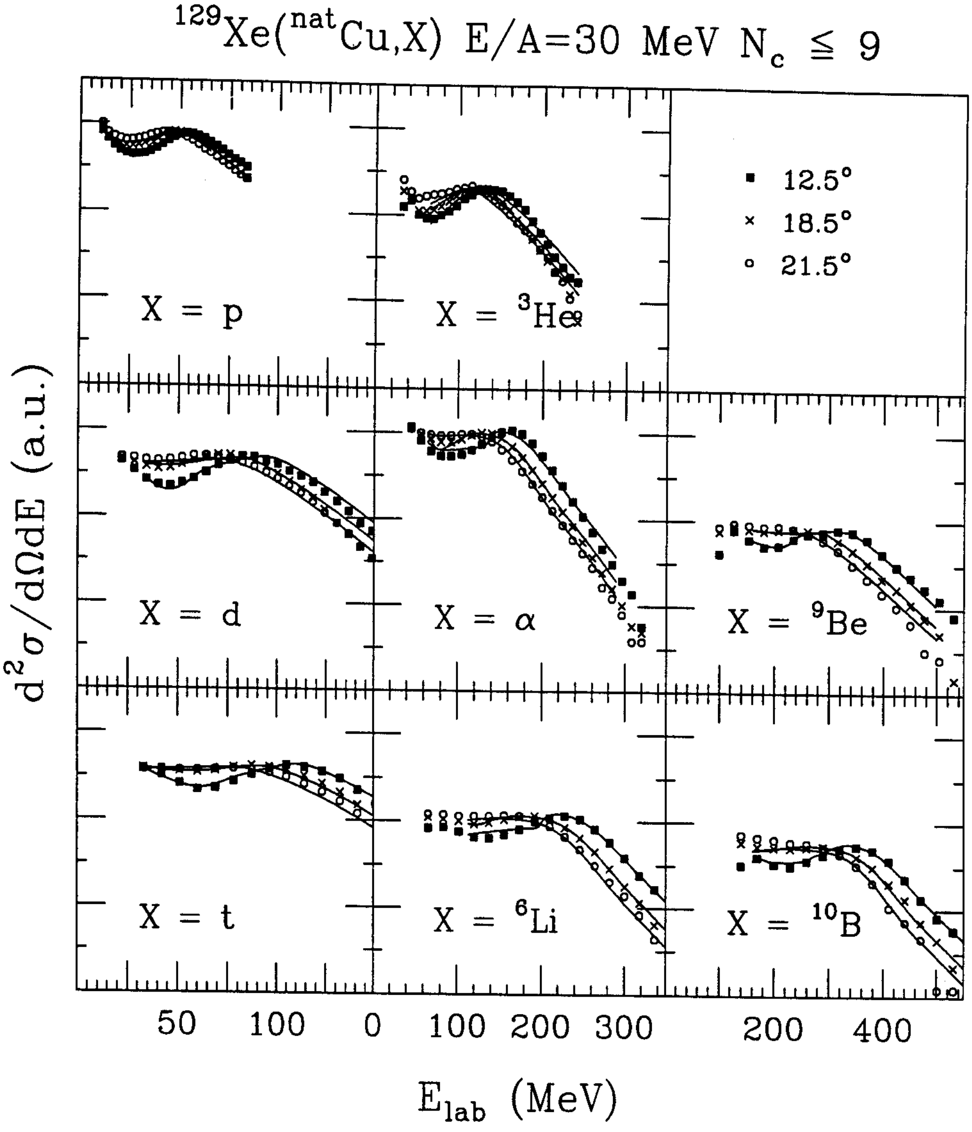

Figure 4.6: Single particle cross sections for p, d, t, ^{3}He, ^{4}He, ^{6}Li, ^{9}Be, and ^{10}B emitted at 30 AMeV ^{129}Xe + ^{nat}Cu peripheral collisions. The curves are the corresponding moving source fits using Eq. 4.2.

without changing direction. In the c.m. frame one obtains [Hsi 94]

$$\frac{dP_1}{dEd\Omega} = \frac{3}{4\pi R_S^3} \int_0^{R_S} r^2 dr \int d\Omega_r \int dE' \frac{dP_1}{dE'd\Omega}(\vec{p}', \vec{v}(\vec{r}), 0))\delta(E' - E + \Delta E_{Coul}(r)) \quad (4.4)$$

with the direction of the particle's momentum assumed unchanged by Coulomb acceleration. The total energy spectrum is obtained by inserting Eq. (4.4) into Eq. (4.2) as the participant source. Best fits to the data using Eq. (4.2) are shown by the solid lines in Fig. 4.3 - 4.6 and the parameter values for the fits are listed in Table 4.1 and Table 4.2.

Although the kinetic energy spectra are well described by the supposition of the contributions from the three sources, the range of angles in the fitting only covers the Multics array (3° – 23°). This is not sufficient to unambiguously establish the parameters of these sources, thus the parameters are useful mainly as input to the efficiency calculations to extract the population probabilities. In the efficiency calculations, the angular distributions of the excited fragments are assumed to be the same as that for the corresponding stable nucleus. In the one exception, ^{6}Li energy spectra are used for unstable ^{5}Li.

4.4 Nuclear Temperatures for Central Collisions from ^{5}Li, ^{10}B, and ^{4}He Excited State Populations

4.4.1 Particle Unstable State of ^{5}Li

Fig. 4.7 and Fig. 4.8 show the correlation functions for the decay of $^5\text{Li}_{g.s} \rightarrow p + \alpha$ (top panel) and $^5\text{Li}^* \rightarrow d + {}^3\text{He}$ (bottom panel) for Au + Au and Xe + Cu reactions at central collisions. For these two systems, central collisions are defined as $\hat{b} < 0.45$ ($N_c > 21$) for Au + Au reactions and $\hat{b} < 0.6$ ($N_c > 9$) for Xe + Cu reactions to maximize

Au + Au central collisions

Part.	a_1	a_2	a_3	T_1	T_2	T_3	β_{exp}	β_2	β_3
p	1.42	0.24	-	14.3	8.1	-	-	8.8E-2	-
d	8.1	3.4	-	6.7	5.5	-	3.2E-2	9.6E-2	-
t	9.6	3.7	-	5.9	5.6	-	3.2E-2	8.0E-2	-
^{3}He	3.2	0.3	-	12.2	7.1	-	3.2E-2	10.4E-2	-
^{4}He	12.0	20.0	-	6.8	7.8	-	3.2E-2	8.7E-2	-
^{6}Li	1.4	0.2	-	14.3	8.1	-	3.2E-2	9.5E-2	-
^{9}Be	0.76	0.35	-	21.4	12.1	-	3.2E-2	9.1E-2	-
^{10}B	0.26	0.14	-	14.0	14.9	-	3.2E-2	8.2E-2	-

Au + Au peripheral collisions

Part.	a_1	a_2	a_3	T_1	T_2	T_3	β_{exp}	β_2	β_3
p	0.35	29.0	-	13.4	5.5	-	1.0E-3	11.0E-2	-
d	0.17	14.0	-	13.5	4.8	-	3.2E-2	11.0E-2	-
t	4.8	10.0	-	10.9	5.4	-	3.2E-2	9.1E-2	-
^{3}He	4.3	1.7	-	12.3	8.8	-	3.2E-2	9.9E-2	-
^{4}He	11.9	57.6	-	10.1	6.7	-	3.2E-2	9.9E-2	-
^{6}Li	1.9	1.0	-	3.0	7.9	-	3.2E-2	9.7E-2	-
^{9}Be	0.54	1.2	-	5.3	15.3	-	3.2E-2	9.0E-2	-
^{10}B	0.86	0.36	-	4.8	14.3	-	3.2E-2	8.6E-2	-

Table 4.1: Source parameters in the center of mass for the three moving-source fits for Au + Au central collisions and peripheral collisions. $\vec{\beta}_3 = -\vec{\beta}_2$, $a_3 = a_2$, and $T_3 = T_2$

Xe + Cu central collisions

Part.	a_1	a_2	a_3	T_1	T_2	T_3	β_{exp}	β_2	β_3
p	22.2	18.7	68.6	3.9	24.0	11.0	2.8E-2	4.2E-2	-1.4E-1
d	14.2	6.4	48.0	5.3	7.0	13.5	2.9E-2	3.9E-2	-1.1E-1
t	9.6	1.0	17.4	5.1	2.8	15.1	2.9E-2	3.9E-2	-1.1E-1
^{3}He	5.3	0.08	15.0	8.8	11.3	5.7	2.9E-2	4.0E-2	-1.5E-1
^{4}He	68.3	30.4	190.	5.2	7.1	7.5	9.9E-3	5.0E-2	-1.4E-1
^{6}Li	1.7	0.2	100.	8.4	7.8	8.1	8.9E-3	4.2E-2	-1.3E-1
^{9}Be	1.1	0.2	43.2	9.0	12.9	25.0	4.0E-2	5.5E-2	-1.6E-1
^{10}B	0.6	0.06	63.9	9.2	13.5	21.1	2.9E-2	4.4E-2	-1.7E-1

Xe + Cu peripheral collisions

Part.	a_1	a_2	a_3	T_1	T_2	T_3	β_{exp}	β_2	β_3
p	54.4	1.37	91.1	5.9	7.4	5.5	2.5E-2	4.2E-2	-1.4E-1
d	9.0	3.6	50.3	4.4	6.5	8.8	6.3E-3	4.9E-2	-1.6E-1
t	9.0	0.3	77.0	4.8	3.3	13.5	2.9E-2	4.0E-2	-1.3E-1
^{3}He	4.6	0.06	1.9	8.0	12.9	20.5	2.9E-2	4.0E-2	-1.3E-1
^{4}He	69.5	3.3	23.7	6.2	5.0	21.5	2.9E-2	4.4E-2	-1.4E-1
^{6}Li	1.3	0.5	0.01	3.8	8.4	5.0	9.1E-3	5.1E-2	-1.4E-1
^{9}Be	0.7	0.3	22.3	10.5	15.9	17.3	7.9E-3	4.5E-2	-1.6E-1
^{10}B	0.6	0.2	-	2.2	13.4	-	9.1E-3	4.0E-2	-

Table 4.2: Source parameters in the center of masses for the three moving-source fits for Xe + Cu central collisions and peripheral collisions.

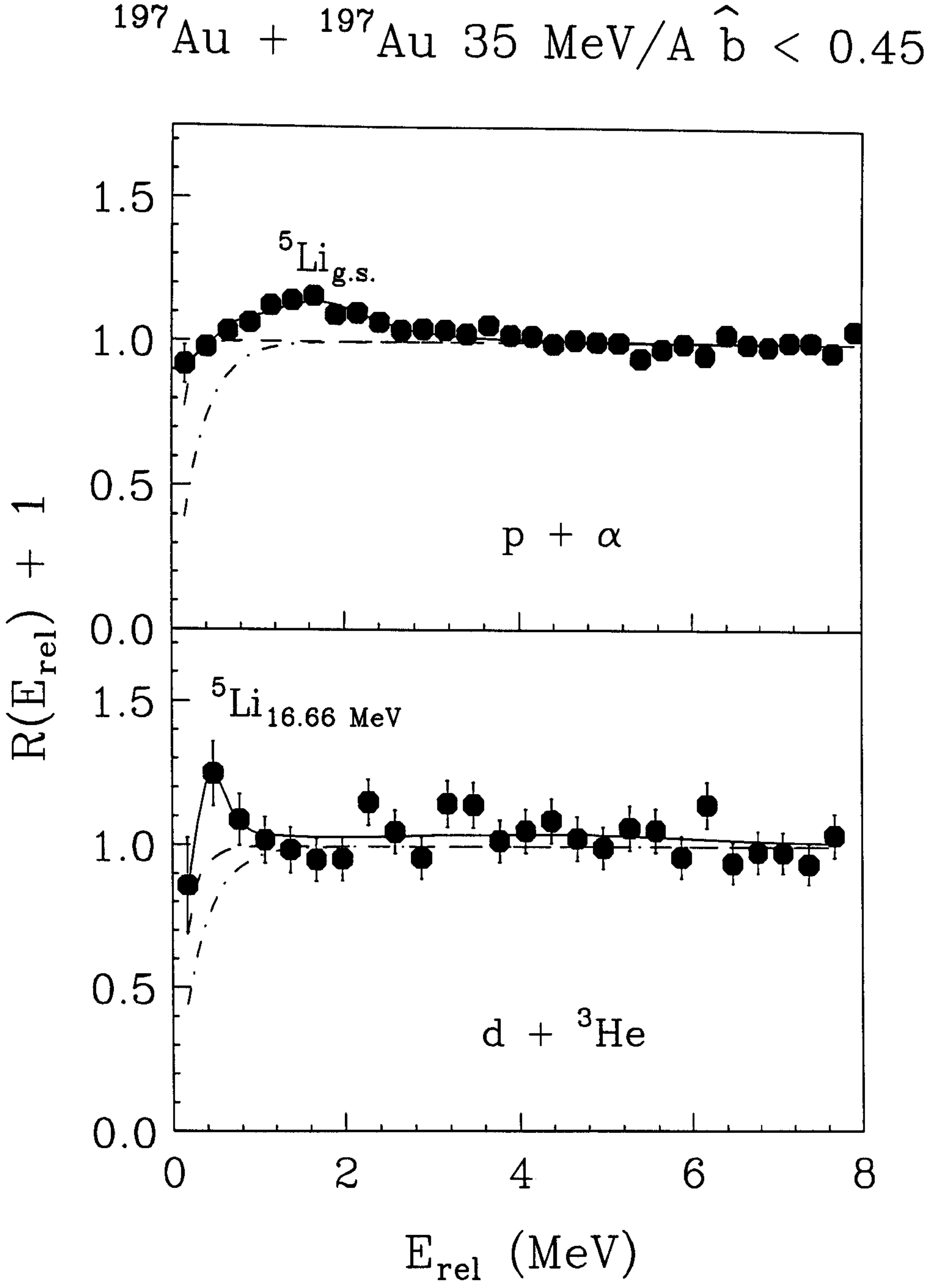

Figure 4.7: p - α (top panel) and d - ^{3}He (bottom panel) correlation functions as a function of relative energy for 35 AMeV Au + Au central collisions. The solid curves show the best fits. The dashed and dot-dashed lines depict two extreme backgrounds.

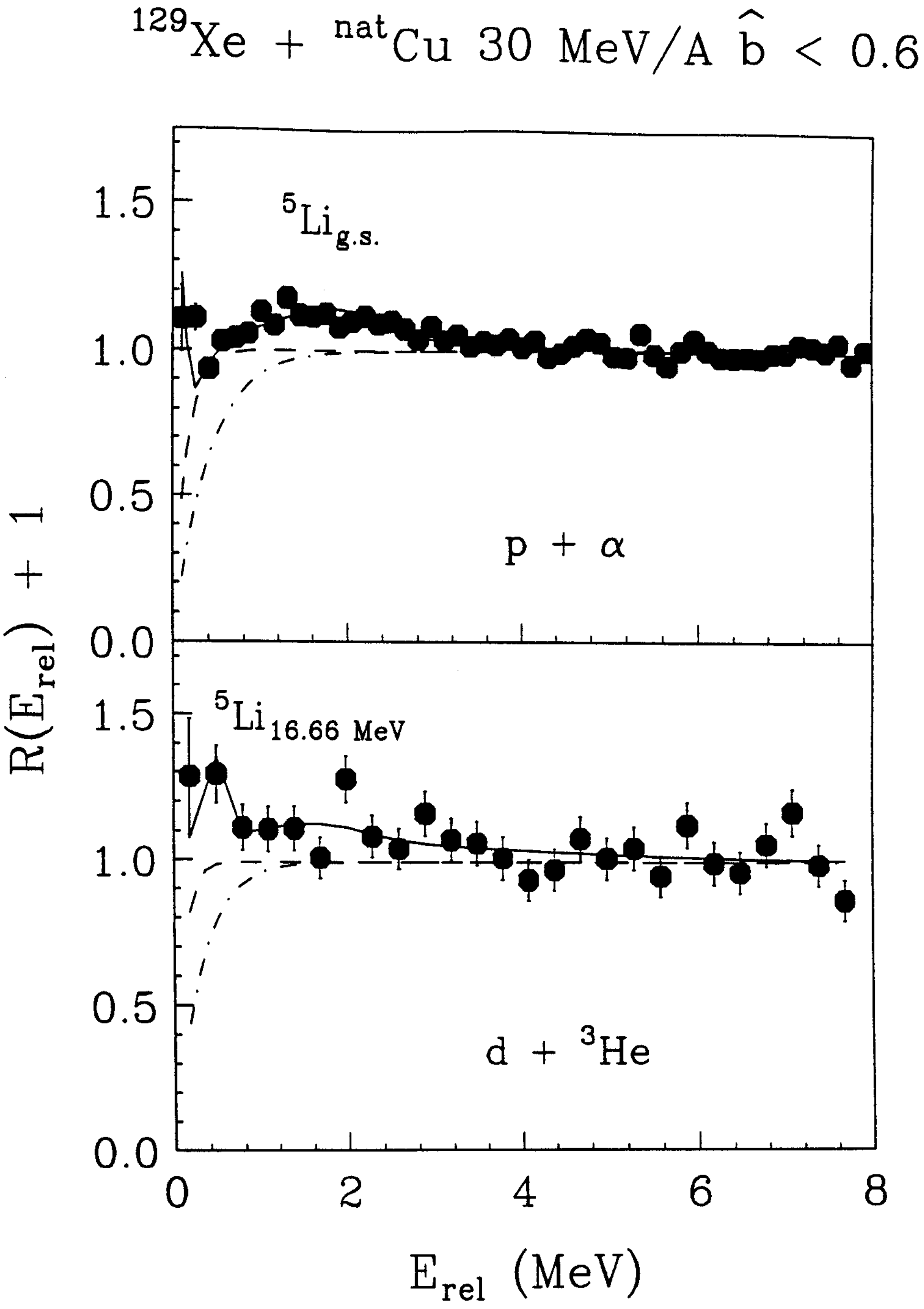

Figure 4.8: p - α (top panel) and d - ^{3}He (bottom panel) correlation functions as a function of relative energy for 30 AMeV Xe + Cu central collisions. The solid curves show the best fits. The dashed and dot-dashed lines depict two extreme backgrounds.

the statistics and to select a single source. The solid lines are the best fit from the Breit-Wigner formula Eq. (3.22), the dashed and dot-dashed lines depict two extreme backgrounds used to extract the uncertainty due to background subtraction. At low relative energies of p - α correlations, there is frequently observed a narrow peak [Poch 85, Naya 92] at E_{rel} = 0.19 MeV due to the two stage decay of ^{9}B, where $^{9}B_{g.s} \rightarrow p + {}^{8}Be_{g.s} \rightarrow p + \alpha + \alpha$. This peak was not detected in the Au + Au reactions perhaps because of large contribution to the background. The broad peak at 1 MeV $\leq E_{rel} \leq$ 3 MeV in the p - α correlation functions is due to the decay of the particle unbound ground state of ^{5}Li ($J^{\pi} = \frac{3}{2}^{-}, \Gamma = 1.5MeV, \Gamma_p/\Gamma = 1.0$) [Ajze 88]. Because the state is rather broad, the Boltzmann factor distorts the shape of the peak as described by Eq. (3.20). To address this distorted spectrum, a value of T = 4 MeV Boltzmann factor was included in the fitting. The d - ^{3}He correlation functions are shown at bottom panels. A peak corresponding to the 16.66 MeV state in ^{5}Li ($J^{\pi} = \frac{3}{2}^{-}, \Gamma = 200KeV, \Gamma_d/\Gamma = 0.86$) [Ajze 88] can be seen at $E_{rel} \sim$ 0.4 MeV. Because ^{5}Li has no particle stable states, the efficiency was calculated by assuming ^{5}Li to be characterized by the energy spectra of particle stable ^{6}Li. The uncertainties in the population probability reflect uncertainties due to statistics, background subtraction, and as well as uncertainties in the efficiency calculations.

4.4.2 Particle Unstable State of ^{10}B

Fig. 4.9 and Fig. 4.10 show the correlation functions for the decay of $^{10}B^{*} \rightarrow \alpha + {}^{6}Li$ (top panel) and $^{10}B^{*} \rightarrow p + {}^{9}Be$ (bottom panel) for central Au + Au and Xe + Cu collisions. At top panels, the first peak in the α - ^{6}Li correlation function is the ^{10}B excited state at E* = 4.774 MeV with spectroscopic parameters $J^{\pi} = 3^{+}, \Gamma = 0.0084$ KeV, $\Gamma_{\alpha}/\Gamma =$

1.0. The second peak consists of three excited states at E* = 5.1103 MeV ($J^\pi = 2^-, \Gamma = 0.98$ KeV, $\Gamma_\alpha/\Gamma = 1.0$), E* = 5.1639 MeV ($J^\pi = 2^+, \Gamma = 0.00176$ KeV, $\Gamma_\alpha/\Gamma = 0.13$), and E* = 5.18 MeV ($J^\pi = 1^+, \Gamma = 110$ KeV, $\Gamma_\alpha/\Gamma = 1.0$). The third peak also consists of three excited states: E* = 5.9159 MeV ($J^\pi = 2^+, \Gamma = 6$ KeV, $\Gamma_\alpha/\Gamma = 1.0$), E* = 6.0250 MeV ($J^\pi = 4^+, \Gamma = 0.05$ KeV, $\Gamma_\alpha/\Gamma = 1.0$), and E* = 6.1272 MeV ($J^\pi = 3^-, \Gamma = 2.36$ KeV, $\Gamma_\alpha/\Gamma = 0.97$). The fourth small peak is at E* = 6.56 MeV with spectroscopic parameters $J^\pi = 4^-, \Gamma = 25.1$ KeV, $\Gamma_\alpha/\Gamma = 1.0$. Two more excited states of ^{10}B at E* = 8.889 MeV and E* = 8.895 MeV, which decay to the 3.563 MeV excited state of ^{6}Li via α emission, were also included in the fitting but had little influence on the fit parameters of the other peaks and could not be accurately determined.

Shown in the bottom panels are the p - ^{9}Be correlation functions. The first peak around $E_{rel} = 0.4$ MeV is near the threshold and consists of two excited states of 6.873 and 7.002 MeV. This peak is included in the fit but not analyzed because the branching ratio information is not accurately known and because the peak lies close to the detection threshold. The second peak at $E_{rel} \sim 1$ MeV consists a group of four excited states at E* = 7.43 MeV ($J^\pi = 2^-, \Gamma = 100$ KeV, $\Gamma_p/\Gamma = 0.70$), E* = 7.467 MeV ($J^\pi = 1^+, \Gamma = 65$ KeV, $\Gamma_p/\Gamma = 1.0$), E* = 7.478 MeV ($J^\pi = 2^+, \Gamma = 74$ KeV, $\Gamma_p/\Gamma = 0.65$), and E* = 7.5595 MeV ($J^\pi = 0^+, \Gamma = 2.65$ KeV, $\Gamma_p/\Gamma = 1.0$). The third peak in the p - ^{9}Be correlation functions is close to the second peak and has three excited states: E* = 7.67 MeV ($J^\pi = 1^+, \Gamma = 250$ KeV, $\Gamma_p/\Gamma = 0.30$), E* = 7.819 MeV ($J^\pi = 1^-, \Gamma = 260$ KeV, $\Gamma_p/\Gamma = 0.9$), and E* = 8.07 MeV ($J^\pi = 2^+, \Gamma = 800$ KeV, $\Gamma_p/\Gamma = 0.1$). The fourth peak consists of two excited states: E* = 8.889 MeV ($J^\pi = 3^-, \Gamma = 84$ KeV, $\Gamma_p/\Gamma = 0.95$), and E* = 8.895 MeV

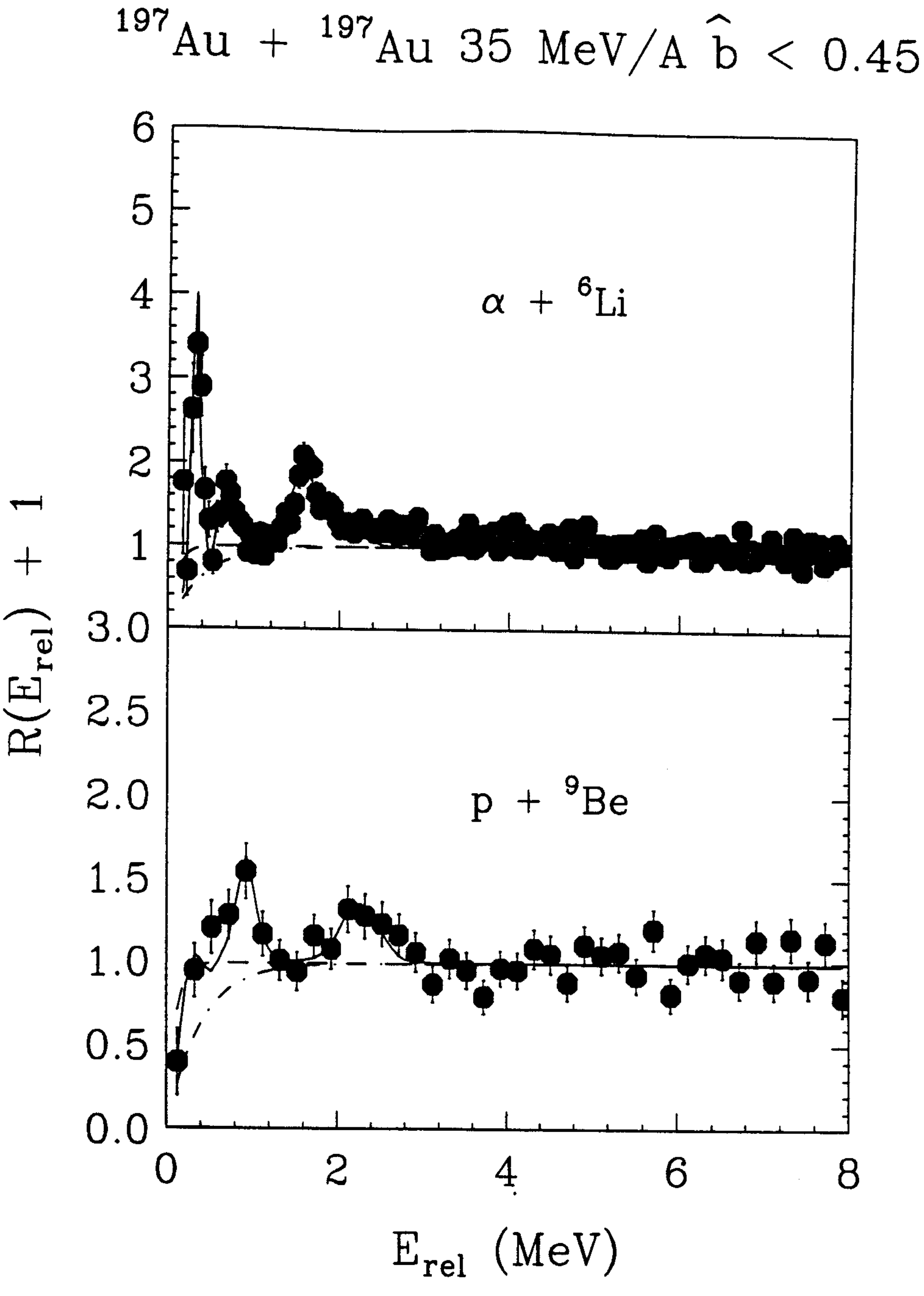

Figure 4.9: α - ^{6}Li (top panel) and p - ^{9}Be (bottom panel) correlation functions as a function of relative energy for 35 AMeV Au + Au central collisions. The solid curves show the best fits. The dashed and dot-dashed lines depict two extreme backgrounds.

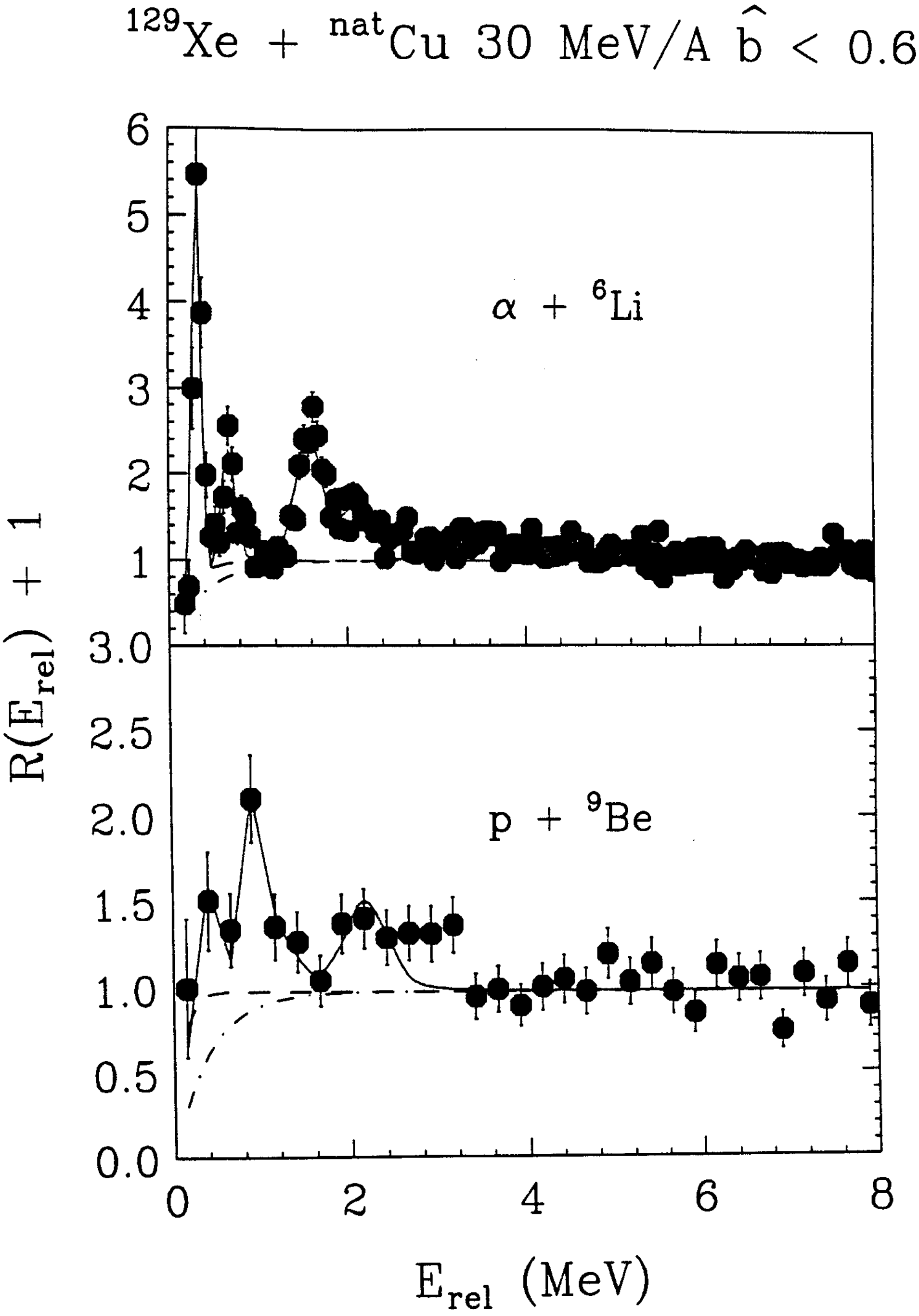

Figure 4.10: α - ^{6}Li (top panel) and p - ^{9}Be (bottom panel) correlation functions as a function of relative energy for 30 AMeV Xe + Cu central collisions. The solid curves show the best fits. The dashed and dot-dashed lines depict two extreme backgrounds.

($J^{\pi} = 2^{+}, \Gamma = 40$ KeV, $\Gamma_p/\Gamma = 0.19$).

Population probabilities of ^{10}B decay (n_i) are shown in Fig. 4.11 as a function of excitation energy for central Au + Au collisions (top panel) and central Xe + Cu collisions (bottom panel). The first three groups of excited states in the α - ^{6}Li correlation functions and the second group of excited states in p - ^{9}Be correlations functions are plotted as solid points in Fig. 4.11. The solid line in the top (bottom) panel of Fig. 4.11 shows an exponential dependence corresponding to a Boltzmann factor in Eq. (3.2) for a temperature of T = 4 (3.5) MeV normalized arbitrarily to the excited state E* 4.74 MeV. The population probability for the third group of states is similar to that of the second group. Such a trend was observed for central ^{36}Ar + ^{197}Au collisions at E/A = 35 MeV [Zhu 92] where it was attributed to the possible additional yield from a 3^{+} state predicted in shell model calculations [Brow 88]. The population of this third group of states does not display an inversion observed in ^{14}N + Ag inclusive measurements of E/A = 35 MeV [Naya 89] and peripheral ^{36}Ar + ^{197}Au collisions at E/A = 35 MeV [Zhu 92] where they were attributed to non-equilibrium effects.

4.4.3 Particle Unstable State of ^{4}He

Fig. 4.12 shows the correlations functions for the decay $^{4}\text{He} \rightarrow \text{p} + \text{t}$ as a function of relative momentum at central collision for Au + Au and Xe + Cu reactions. The correlation function was plotted as a function of the relative momentum because it effectively expands the region at small relative energy (The peak of the first ^{4}He excited states is at a relative energy about 0.2 MeV). Three excited states were included in the fitting of the correlation functions [Fiar 73, Feld 90, Kund 91]: E* = 20.1 MeV ($J^{\pi} = 0^{+}, \Gamma = 270$ KeV, $\Gamma_p/\Gamma = 1.0$),

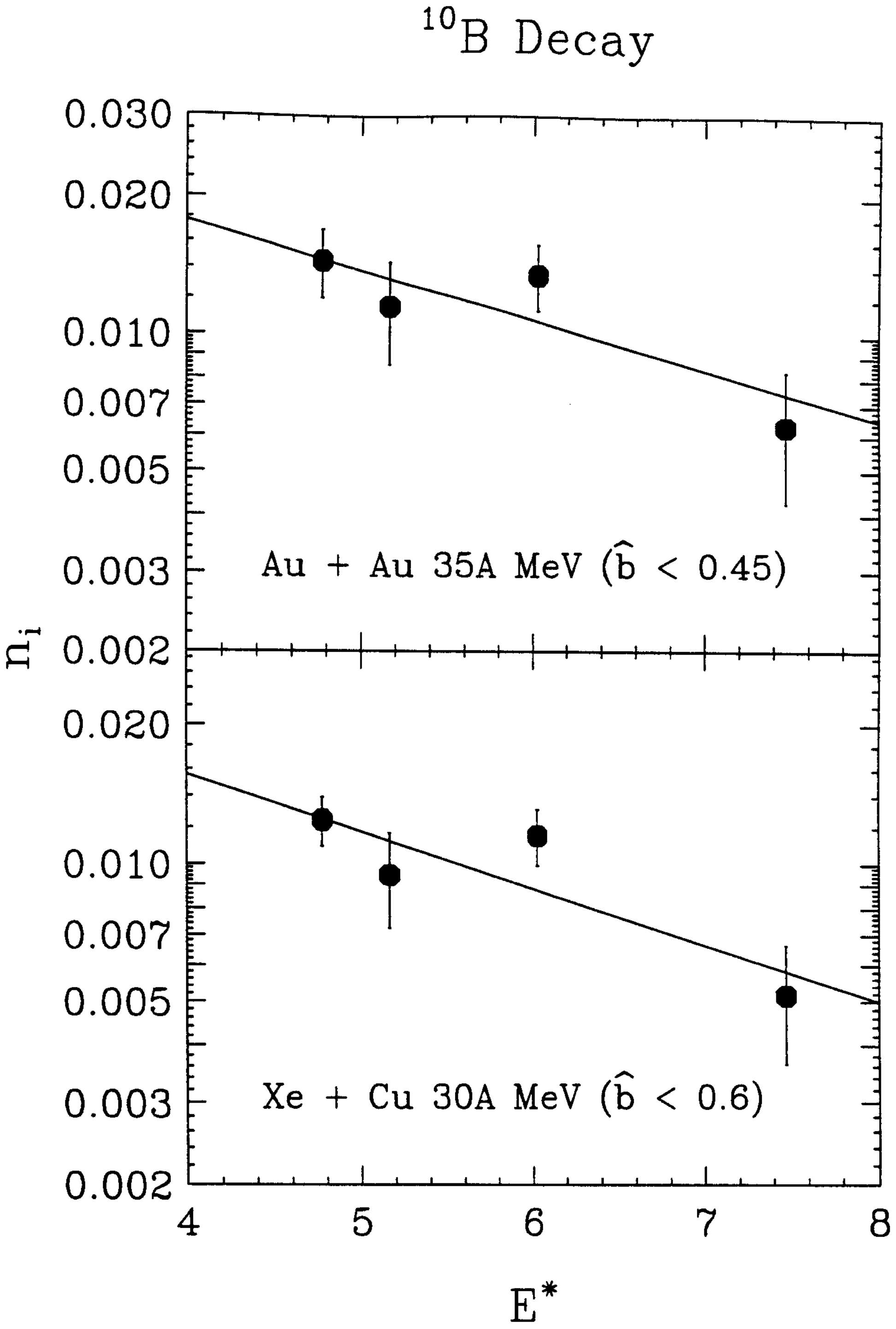

Figure 4.11: Population probabilities (n_i) as a function of excitation energy for Au + Au central collisions (top panel) and Xe + Cu central collisions (bottom panel). The lines denote exponential $\exp(-E^*/T)$ factor with T = 4 (3.5) MeV in the top (bottom) panel.

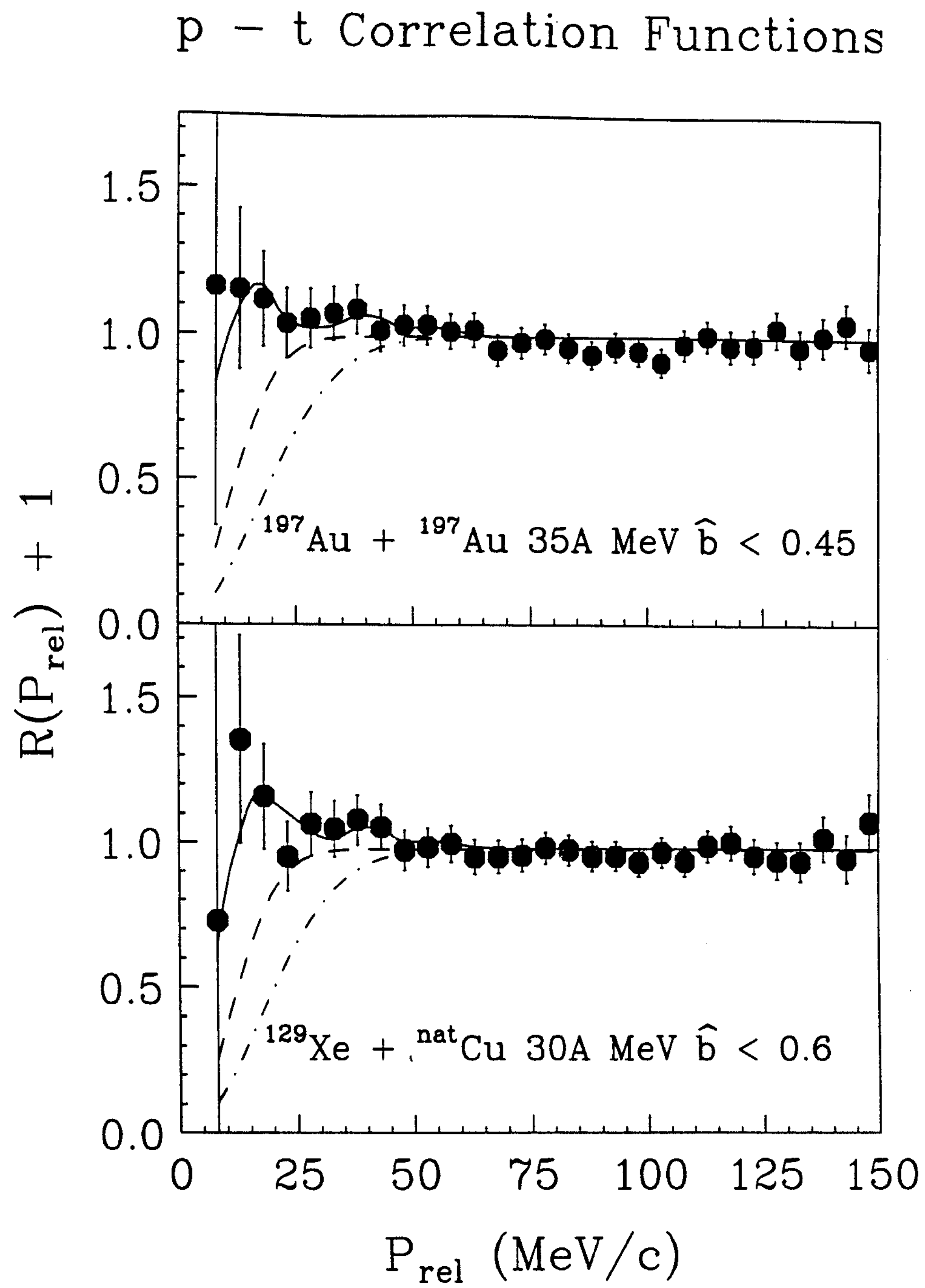

Figure 4.12: proton - triton correlation functions as a function of relative momenta for 35 AMeV Au + Au central collisions (top panel) and 30 AMeV Xe + Cu central collisions (bottom panel). The solid curves show the best fits. The dashed and dot-dashed lines depict two extreme backgrounds.

E* = 21.1 MeV ($J^\pi = 0^-, \Gamma = 300$ KeV, $\Gamma_p/\Gamma = 0.6$), and E* = 22.1 MeV ($J^\pi = 2^-, \Gamma = 300$ KeV, $\Gamma_p/\Gamma = 0.6$). However, only the yield of the first peak of E* = 20.1 MeV is significant when compared to the background which increase rapidly with E_{rel} and therefore only it is used in the measurement of temperatures.

4.4.4 Temperatures from Excited State Populations

The "apparent temperatures" obtained from the relative populations of the specific states of ^{5}Li, ^{4}He, and ^{10}B fragments by inverting Eq. (3.2) are shown in Fig. 4.13 for central 35 AMeV Au + Au (left panel) and 30 AMeV Xe + Cu (right panel) collisions. The leftmost data point in both panels of Fig. 4.13 indicates the measured apparent temperature consistent with the ratio of the yield of ^{5}Li in its ($E_j^* = 16.66 MeV, J_j = 3/2^+$) excited state divided by the yield in its ($E_i^* = 0 MeV, J_i = 3/2^-$) ground state. The middle data point shows the measured apparent temperature corresponding to the yield of ^{4}He in its ($E_j^* = 20.1 MeV, J_j = 0^+$) excited state divided by the yield in its ($E_i^* = 0 MeV, J_i = 0^+$) ground state. Since the intrinsic relative energy resolution of the detector is 120 KeV at E*=7.5 MeV, the four excited states of ^{10}B ($7.43 MeV, 2^-$; $7.467 MeV, 1^+$; $7.478 MeV, 2^+$; $7.5599 MeV, 0^+$) are unresolved. The rightmost data point in the left panel shows the measured apparent temperature corresponding to the sum of the yield of ^{10}B in this group of four excited states divided by the yield in the ($4.77 MeV, 3^+$) excited state. The error bars of the apparent temperature reflect both the statistical uncertainty and the uncertainty due to background subtraction.

To extract the emission temperatures from the apparent temperatures, sequential decay calculations described in Section 3.3 are used to calculate the modifications to the

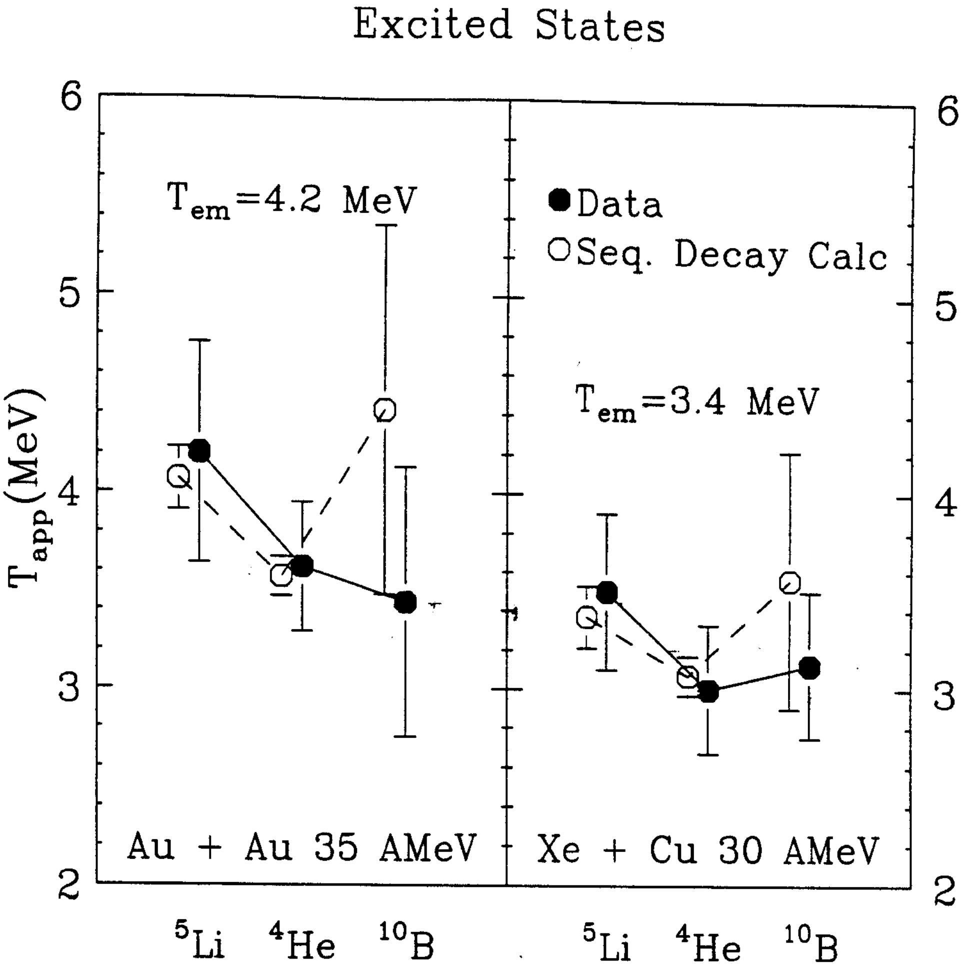

Figure 4.13: Apparent temperatures for 35 AMeV Au + Au (left panel) and 30 AMeV Xe + Cu (right panel) central collisions. The temperatures were obtained from relative populations of excited states for ^{5}Li, ^{4}He and ^{10}B nuclei using Eq. (3.2) The closed points are the data and the open points are the predictions of sequential decay calculations.

initial populations of excited states caused by the sequential feeding from heavier particle unstable nuclei. In these calculations, the excited states of primary emitted fragments are populated thermally, and then allowed to decay. Unknown spins or parities of low lying discrete states were assigned randomly and the calculations were repeated to assess the sensitivities of the population probabilities and isotope ratios to these spectroscopic uncertainties. This unknown spectroscopic information contributes a 5% uncertainty to the calculated ratios. An additional 8% uncertainty stemming from the unknown isotopic composition of the emitting system at freeze-out was assessed by varying the assumed N/Z ratio of the decaying system.

These calculations were performed for initial temperatures ranging from 2 MeV to 6 MeV and the agreement between theory and experiment was assessed by calculating corresponding values for the reduced χ^2 using the expression,

$$\chi^2_\nu(T_{em}) = \frac{1}{\nu}\sum_{i=1}^{\nu} \frac{[R_{expt,i} - R_{calc,i}(T_{em})]^2}{\sigma^2_{expt,i} + \sigma^2_{calc,i}} \tag{4.5}$$

independently for the excited state populations. Here the $\sigma_{expt,i}$ and $\sigma_{calc,i}$ are the experimental and theoretical uncertainties and the summation runs over the relevant excited state populations. The solid lines in the both panels of Fig. 4.14 show the χ^2_ν values for the excited state populations at $0 \leq \hat{b} \leq 0.45$ (Au + Au) and $0 \leq \hat{b} \leq 0.6$ (Xe + Cu). From the shape and minima of the calculated curves, best fit values of $4.2 \pm 0.6 MeV$ and $3.4 \pm 0.7 MeV$ are determined for the central Au + Au reactions and central Xe + Cu reactions, respectively. The best fit values for the calculated "apparent temperatures" are shown as the open points in Fig. 4.13.

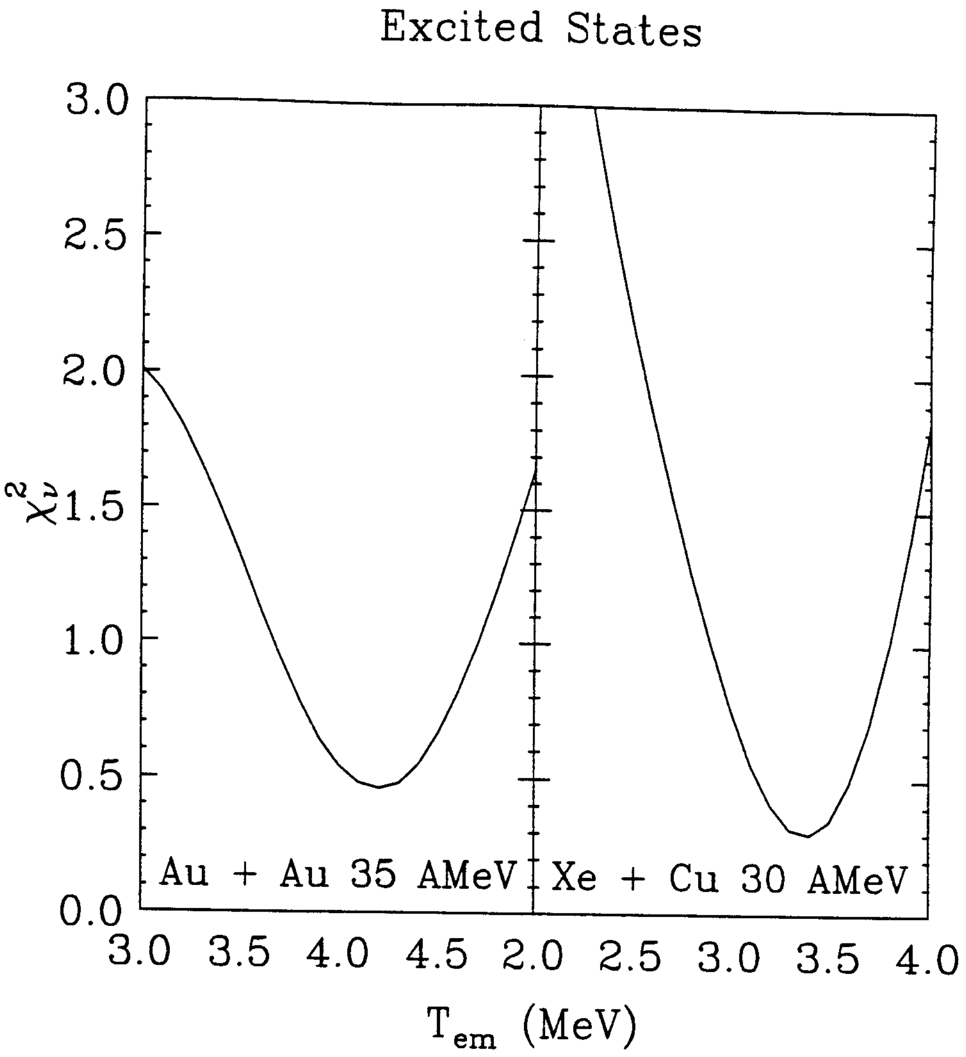

Figure 4.14: Results of the least squares analysis (Eq.4.5) for the relative populations of excited states of ^{5}Li, ^{4}He and ^{10}B nuclei at $\hat{b} < 0.45$ (left panel: Au + Au) and $\hat{b} < 0.6$ (right panel: Xe + Cu).

4.5 Nuclear Temperatures for Central Collisions from Isotope Double Ratios

Double isotope ratio temperatures can be obtained from Eq. (3.26). The same central gates used in populations of excited states method is used here for comparison purposes. Following Ref. [Tsan 96a], we restrict our investigation to thermometers with B values in excess of 10 MeV to reduce fluctuations in the temperature measurement. Table 4.3 lists the nine double isotope yield ratios with values of a and B computed from the relevant ground state spectroscopic information for 35 AMeV Au + Au and 30 AMeV Xe + Cu reactions. Also listed in Table 4.3 and shown in Fig. 4.15 are the corresponding "apparent temperatures" obtained from Eq. (3.26). The uncertainties reflect the changes in double isotope ratio R_{iso} (Eq. (3.26)) observed for different gates on the velocity of the emitted fragments in the center of mass and by considering the sensitivity of the isotopic yields to uncertainties in the precise placement of the isotope gates.

The fluctuations in the "apparent temperatures" from ratio to ratio, shown in Fig. 4.15, are not a manifestation of non-equilibrium effects but instead are the direct consequences of the secondary decay of highly excited fragments whose decay feeds the measured yields. The same sequential decay calculations used in the previous section are used for these isotope thermometers and the reduced χ^2_ν fits by using Eq. (4.5) are shown in Fig. 4.16 for the Au + Au at $0 \leq \hat{b} \leq 0.45$ (left panel) and Xe + Cu at $0 \leq \hat{b} \leq 0.6$ (left panel). The best fit values of 4.4 ± 0.2 MeV and 3.9 ± 0.3 MeV are determined for the central Au + Au reactions and central Xe + Cu reactions, respectively. The consistency of temperatures measured from excited state populations and double isotope ratios for both

Au + Au	a	B	$T_{app}(\hat{b} < 0.45)$	$T_{app}(\hat{b} \approx 0)$
		(MeV)	(MeV)	(MeV)
$^{13,14}C/^{3,4}He$	0.72	12.39	4.04 ± 0.10	4.04 ± 0.16
$^{6,7}Li/^{3,4}He$	2.18	13.32	4.51 ± 0.02	4.64 ± 0.05
$^{9,10}Be/^{3,4}He$	0.38	13.76	7.00 ± 0.24	7.80 ± 0.30
$^{2,3}H/^{3,4}He$	1.59	14.29	4.21 ± 0.01	4.42 ± 0.04
$^{12,13}C/^{3,4}He$	2.94	15.62	4.00 ± 0.05	4.15 ± 0.08
$^{11,12}B/^{3,4}He$	1.95	15.69	3.48 ± 0.02	3.47 ± 0.03
$^{8,9}Li/^{3,4}He$	1.24	16.51	3.71 ± 0.02	3.79 ± 0.07
$^{10,11}B/^{3,4}He$	1.11	17.20	4.02 ± 0.03	4.20 ± 0.08
$^{7,8}Li/^{3,4}He$	1.98	18.54	3.94 ± 0.01	4.04 ± 0.03

Xe + Cu	a	B	$T_{app}(\hat{b} < 0.6)$	$T_{app}(\hat{b} \approx 0)$
		(MeV)	(MeV)	(MeV)
$^{13,14}C/^{3,4}He$	0.72	12.39	3.47 ± 0.03	3.60 ± 0.05
$^{6,7}Li/^{3,4}He$	2.18	13.32	3.98 ± 0.02	3.91 ± 0.05
$^{9,10}Be/^{3,4}He$	0.38	13.76	5.42 ± 0.04	5.45 ± 0.07
$^{2,3}H/^{3,4}He$	1.59	14.29	3.73 ± 0.01	3.61 ± 0.06
$^{12,13}C/^{3,4}He$	2.94	15.62	3.67 ± 0.03	3.75 ± 0.08
$^{11,12}B/^{3,4}He$	1.95	15.69	3.14 ± 0.03	3.31 ± 0.05
$^{8,9}Li/^{3,4}He$	1.24	16.51	3.33 ± 0.02	3.27 ± 0.04
$^{10,11}B/^{3,4}He$	1.11	17.20	3.57 ± 0.02	3.56 ± 0.04
$^{7,8}Li/^{3,4}He$	1.98	18.54	3.77 ± 0.01	3.90 ± 0.04

Table 4.3: List of isotope ratio thermometers with $B > 10MeV$ and the corresponding measured apparent temperatures. The uncertainties in T_{app} are larger for $\hat{b} \approx 0$ than for the broad impact parameter gate; reflecting uncertainties in the extrapolation to $\hat{b} \approx 0$.

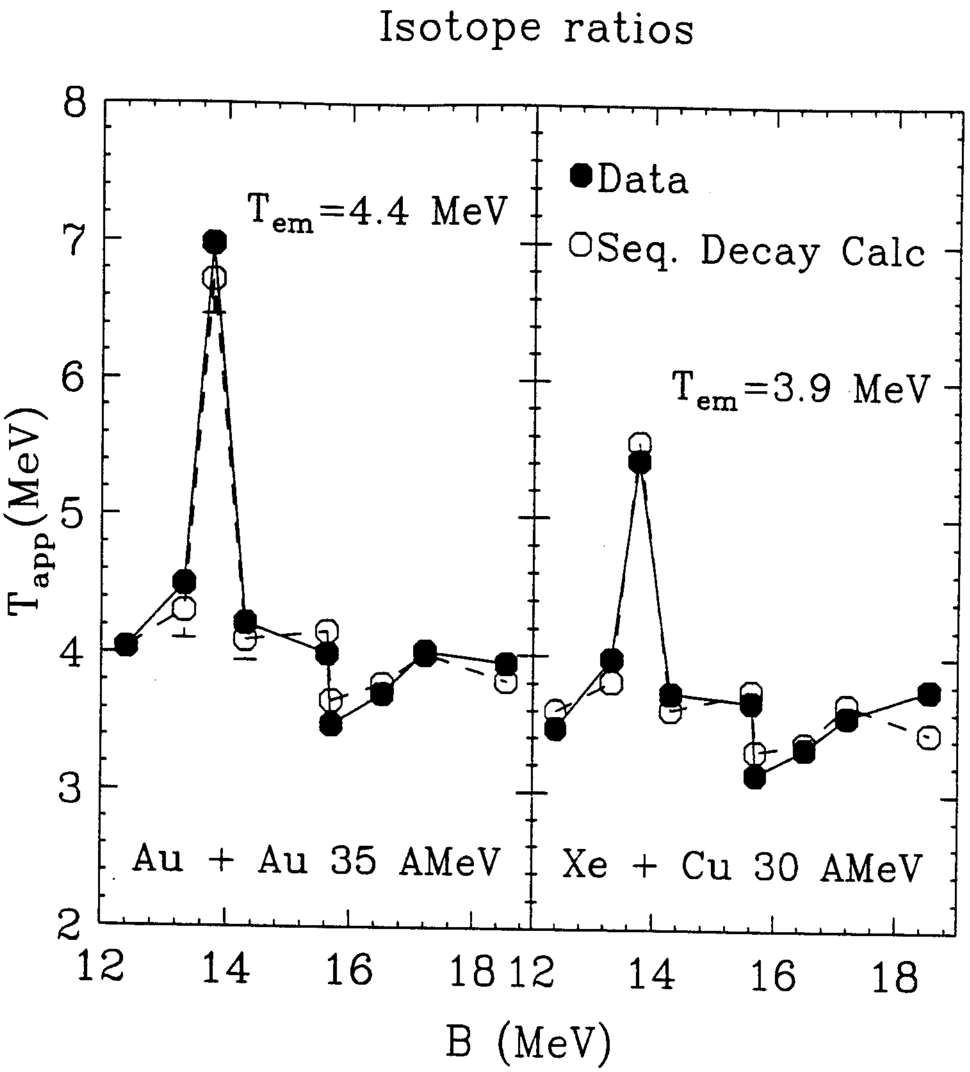

Figure 4.15: Apparent temperatures for 35 AMeV Au + Au (left panel) and 30 AMeV Xe + Cu (right panel) central collisions. The temperatures were obtained from double isotope ratios using Eq. (3.26) The closed points are the data and the open points are the predictions of sequential decay calculations.

35 AMeV Au + Au and 30 AMeV Xe + Cu reactions indicate that the two thermometers provide equivalent information at E/A= 30 and 35 MeV, in contrast to the results reported at significantly higher energies [Poch 96, Serf 96].

The best fit values for the calculated "apparent temperatures" are shown as the open points in Fig. 4.15. The fluctuations for these nine thermometers are well reproduced by the sequential decay calculations. The calculated χ_ν^2 curves in Fig. 4.16 are asymmetric, reflecting a gradual reduction of the sensitivity of $R_{calc}(T_{em})$ to T_{em} with increasing temperature [Xi 96].

4.6 Central Au + Au Collisions at E/A = 35 MeV

The selection of a single source is important for the nuclear temperature measurements because different sources are formed by different dynamics and the temperatures of these sources may not be the same. The velocity distributions of this Au + Au reaction for Z = 7 are shown in Fig. 4.17 for peripheral ($\hat{b} \geq 0.7$, upper panel) and central collisions ($\hat{b} \leq 0.1$, lower panel), respectively [Dago 95]. Fragments are formed primarily in peripheral collisions by the fragmentation of a neck which momentarily join projectile-like and target-like residues [Mont 94]. This "neck" or "overlap region" forms a participant source that grows in size and importance with decreasing impact parameter until it encompasses the entire system. In central Au + Au collisions, the IMF distributions have a major component centered about the center of mass velocity v_{cm} (v_{cm} = 0.14c in this reaction) and projectile-like and target-like sources are only weakly observed. In central Xe + Cu collisions, pre-equilibrium IMF emission was observed at $v_{lab} < v_{cm}$. (v_{cm} = 0.17c for Xe + Cu

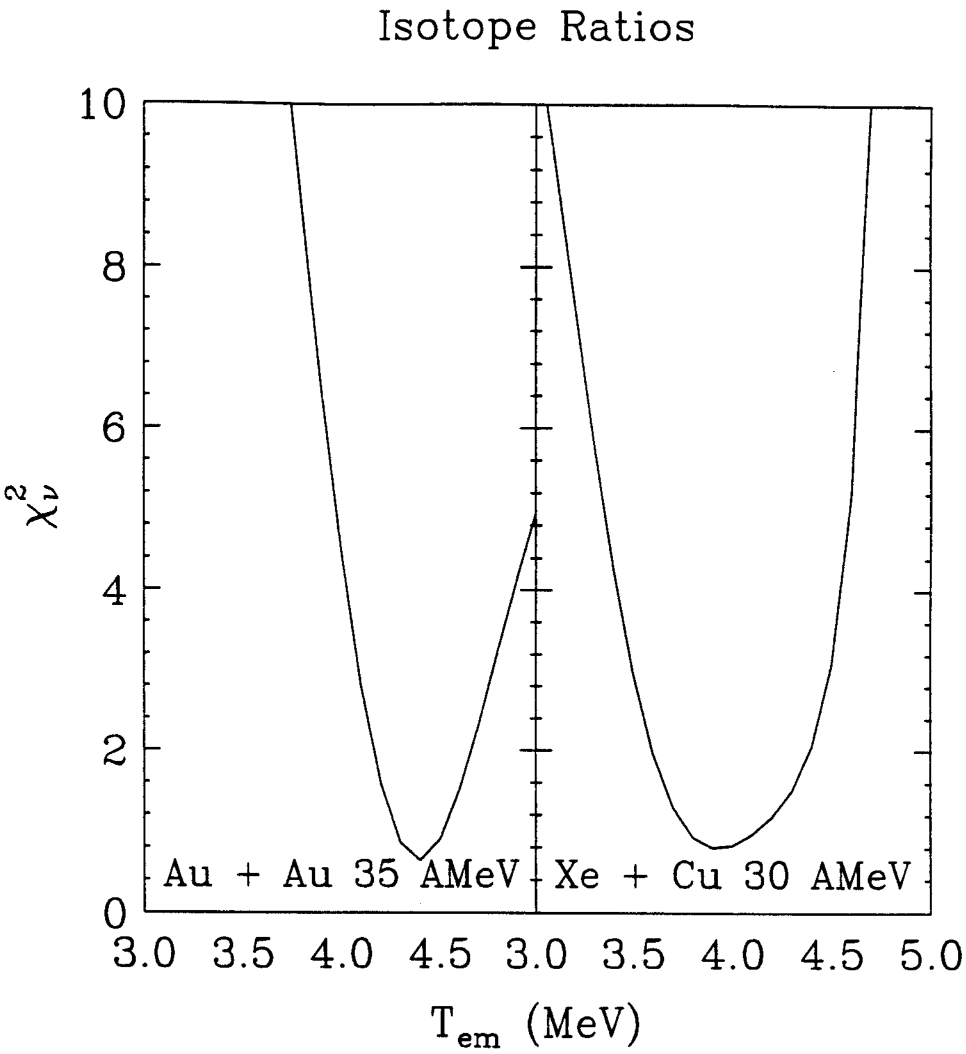

Figure 4.16: Results of the least squares analysis (Eq.4.5) for the double isotope ratios method at $\hat{b} < 0.45$ (left panel: Au + Au) and $\hat{b} < 0.6$ (right panel: Xe + Cu).

collisions at E/A = 30 MeV.) To reduce the contamination from other sources, the velocity cut ($v_{lab} > v_{cm}$) in the Multics array was used to extract temperatures.

A statistical equilibrium calculation performed with the Statistical Multifragmentation Model (SMM) [Botv 87, Bond 95] was used to describe fragment-fragment correlations, charge distributions, and kinetic energy spectra for this Au + Au system [Dago 96, Dago 96a]. The SMM is based upon the assumption of statistical equilibrium at a low-density freeze-out stage of the reaction at which the primary fragments are formed according to their equilibrium partitions. The equilibrium partitions are calculated according to the micro-canonical ensemble of all break-up channels composed of nucleons and excited fragments of different masses [Bond 94]. The model conserves total excitation energy, momentum, mass and charge number. The statistical weight of decay channel j is given by $W_j \propto \exp S_j(E_S^*, A_S, Z_S)$, where S_j is the entropy of the system in channel j and E_S^*, A_S, and Z_S are the excitation energy, mass and charge number of the source. Different break-up configurations are initialized according to their statistical weights. The fragments are then propagated in their mutual Coulomb field and are allowed to undergo secondary decays. Light fragments with mass number $A_f \leq 4$ are considered as stable particles ("nuclear gas") with only translational degrees of freedom; fragments with $A_f \geq 4$ are treated as heated nuclear liquid drops. The secondary decay of large fragments ($A_f \geq 16$) is calculated from an evaporation-fission model, and that of smaller fragments from a Fermi break-up model [Botv 87, Dago 96a].

Information about the freeze-out density in nuclear reactions can be accessed by two-fragment correlation functions because the correlation functions are sensitive to the

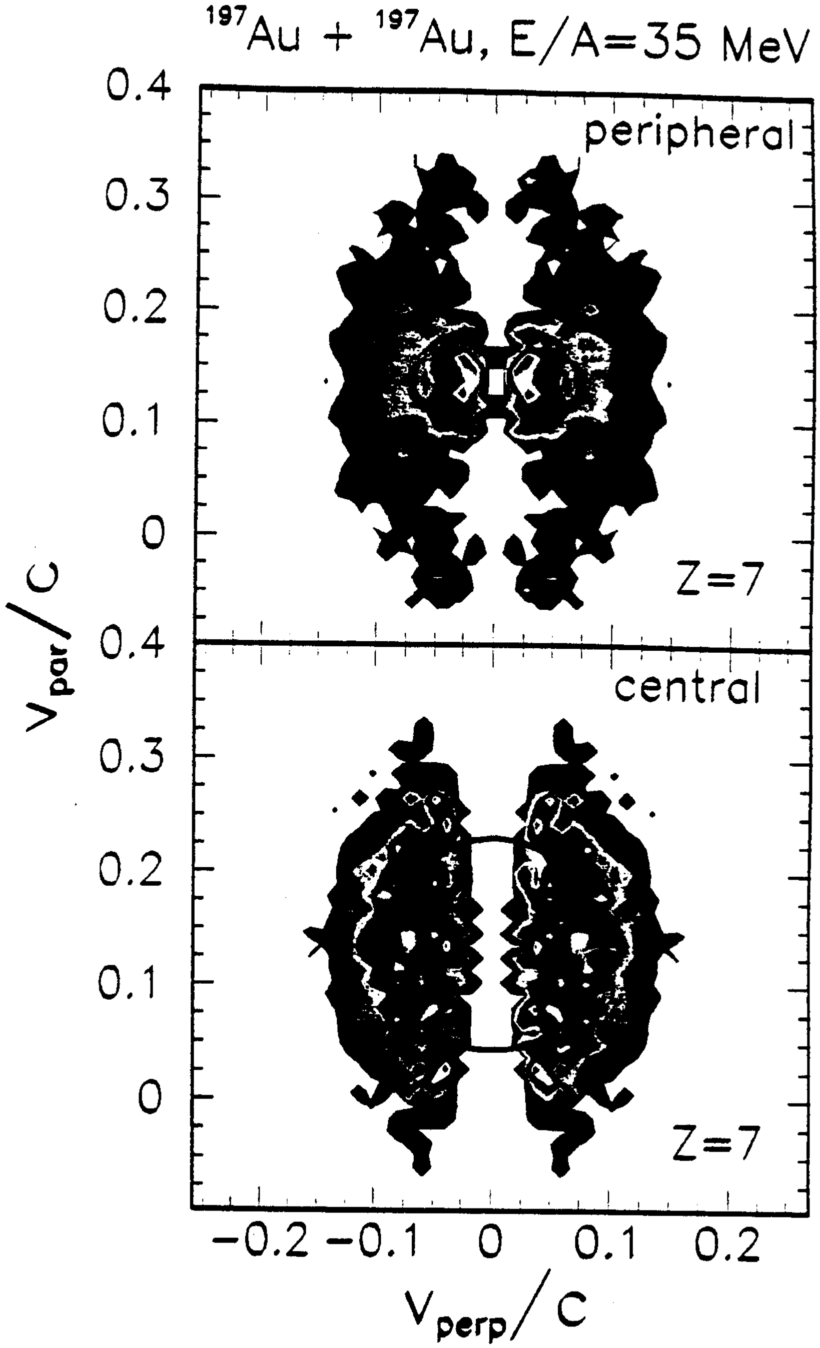

Figure 4.17: Velocity distributions $d^2P/v_\perp dv_\parallel dv_{perp}$ for Z = 7 fragments emitted in peripheral collisions ($\hat{b} \geq 0.7$, upper panel) and central collisions ($\hat{b} \leq 0.1$, lower panel). The velocity axes are in units of the speed of light, and the intensity scale is linear. The circle corresponds to a fixed velocity of 0.1c in the center of mass. [Dago 95]

spatial separation of emitted fragments. The correlation functions $1 + R(v_{red})$ are defined as:

$$1 + R(v_{red}) = C\frac{Y(v_{red})}{Y_{back}(v_{red})} \tag{4.6}$$

where $v_{red} = |\mathbf{v_i}-\mathbf{v_j}|/\sqrt{Z_i + Z_j}$ is the "reduced" relative velocity of fragments i and j $(i \neq j)$ with charge Z_i and Z_j; $Y(v_{red})$ and $Y_{back}(v_{red})$ are the coincidence and background yields for fragment pairs of reduced velocity v_{red} and $C = N_{back}/N_{coinc}$, where N_{back} and N_{coinc} are the total number of background and coincidence pairs. The two-fragment correlation functions for 35 AMeV central Au + Au reactions are shown in Fig. 4.18 as solid points for panel (a) in the Multics array ($3 \leq Z \leq 30$, $8° \leq \theta_{lab} \leq 23°$) and for panel (b) in the Miniball array ($3 \leq Z \leq 10$, $23° \leq \theta_{lab} \leq 40°$). The solid and dashed curves in Fig. 4.18 depict the results of SMM calculations performed for $\rho_s = \rho_0/3$ and $\rho_s = \rho_0/6$, respectively, where ρ_0 is the normal nuclear matter density and ρ_s is the freeze-out density. Overall, the measured correlation functions are reasonably well reproduced by the SMM calculations wherein the fragments are produced via a bulk multifragmentation at a density of $\rho_0/6 \leq \rho_s \leq \rho_0/3$ and a temperature of $T \approx 6$ MeV [Dago 96, Dago 96a].

Using the inherent symmetry of the Au + Au reaction, the detection efficiency was determined and an efficiency corrected mean IMF multiplicity $\langle N_{IMF}\rangle = 10.8 \pm 1$ was obtained [Dago 95]. The corresponding efficiency corrected charge distribution, shown by the solid points in Fig. 4.19, is surprisingly flat. A similar flat charge distribution, shown by the open points, is also observed for fragments emitted at center of mass angles of $\theta_{c.m.} = 90° \pm 20°$, suggesting that the large abundance of heavier fragments does not originate from the decay of projectile-like and target-like remnants [Dago 95]. (Differences

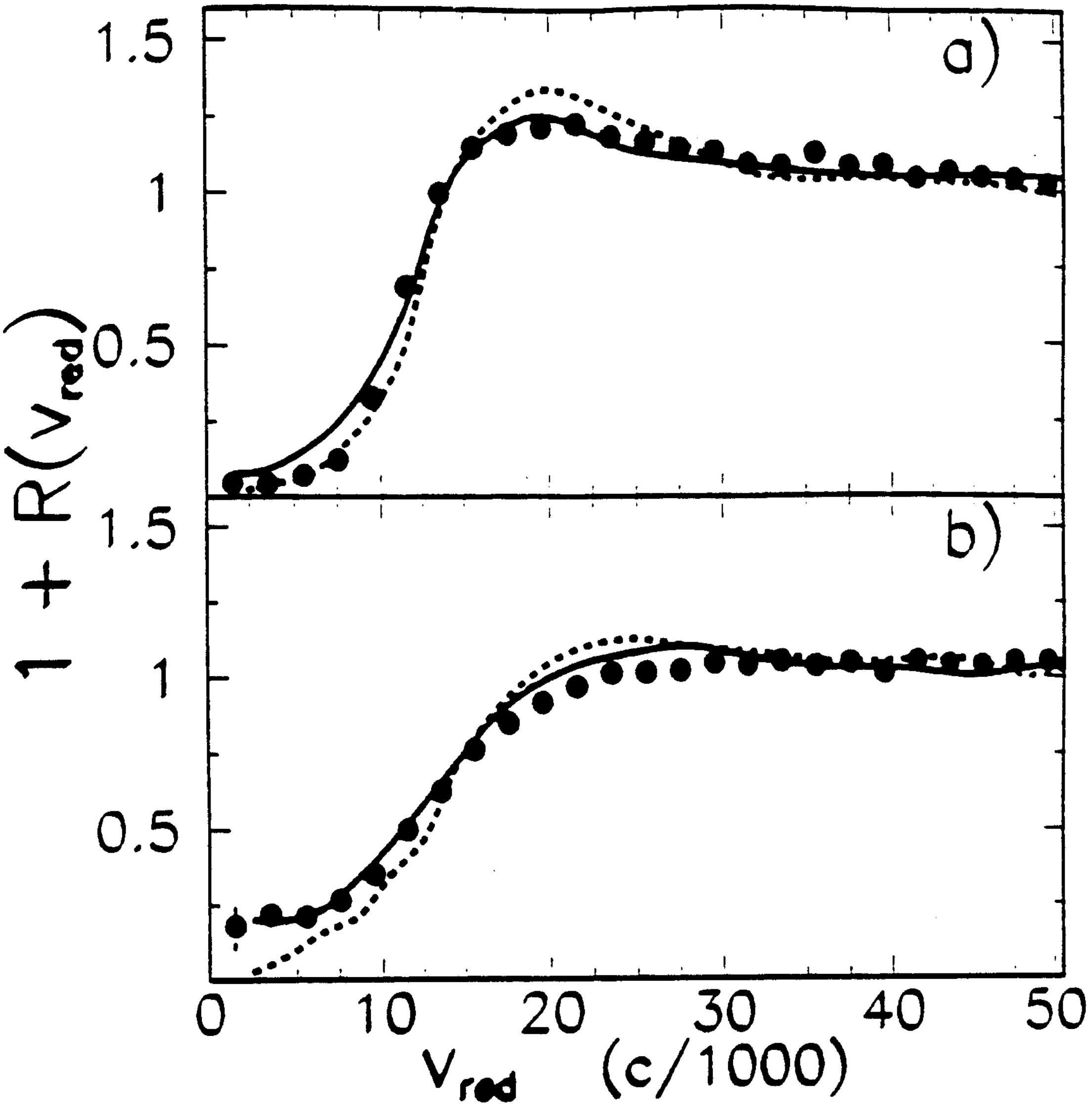

Figure 4.18: Two-fragment correlation functions $1+R(v_{red})$ for $3 \leq Z \leq 30$ and $8° \leq \theta_{lab} \leq 23°$ (part a) and for $3 \leq Z \leq 10$, $23° \leq \theta_{lab} \leq 40°$ (part b). Full points are experimental data. The solid and dashed lines are SMM predictions for $\rho_s = \rho_0/3$, and $\rho_s = \rho_0/6$ [Dago 96a]

between the two sets of data are comparable to the systematic uncertainties in the efficiency correction.) For comparison, Fig. 4.19 also shows the charge distribution measured for central collisions at E/A = 100 MeV (solid squares) [Kund 95] and the charge distribution measured in peripheral collisions at E/A = 1000 MeV (open squares) for the same system [Kund 95]. Both of these charge distributions measured at higher energies decrease much more steeply with fragment charge.

Early investigations of high-energy hadron-nucleus collisions revealed a power-law behavior, $P(A) \propto A^{-\tau}$, of the inclusive mass distributions [Hirs 84], similar to that observed for the distributions of droplets for near-critical, macroscopic systems exhibiting a liquid and a gaseous phase [Fish 67]. Consistent with this macroscopic analogy, values for the "critical parameter" of τ have been extracted from analyses of charge distributions measured for smaller systems containing 80 - 200 nucleons [Mahi 88, Li 93]. After correction for finite size effects and detection efficiency, values for $\tau \approx 2.2$ are obtained for peripheral collisions in the domain of limiting fragmentation; one such example is provided by the data for slowly expanding systems produced via peripheral collisions at E/A = 1000 MeV shown in Fig. 4.19. Similar data have been interpreted as evidence for near critical behavior [Mahi 88, Li 93, Gilk 94].

Such attempts to extract critical exponents from scaling laws have relied heavily upon the assumption that the charge or mass distributions of systems at thermal equilibrium display minimum values for τ at the critical point. The charge distribution in Fig. 4.19 for E/A = 35 MeV can be described in the range of $3 \leq Z \leq 20$ by a χ^2 fit of a power law with values for τ of $\tau = 1.22 \pm 0.05$. This value is much smaller than the value $\tau \approx 2.2$ expected

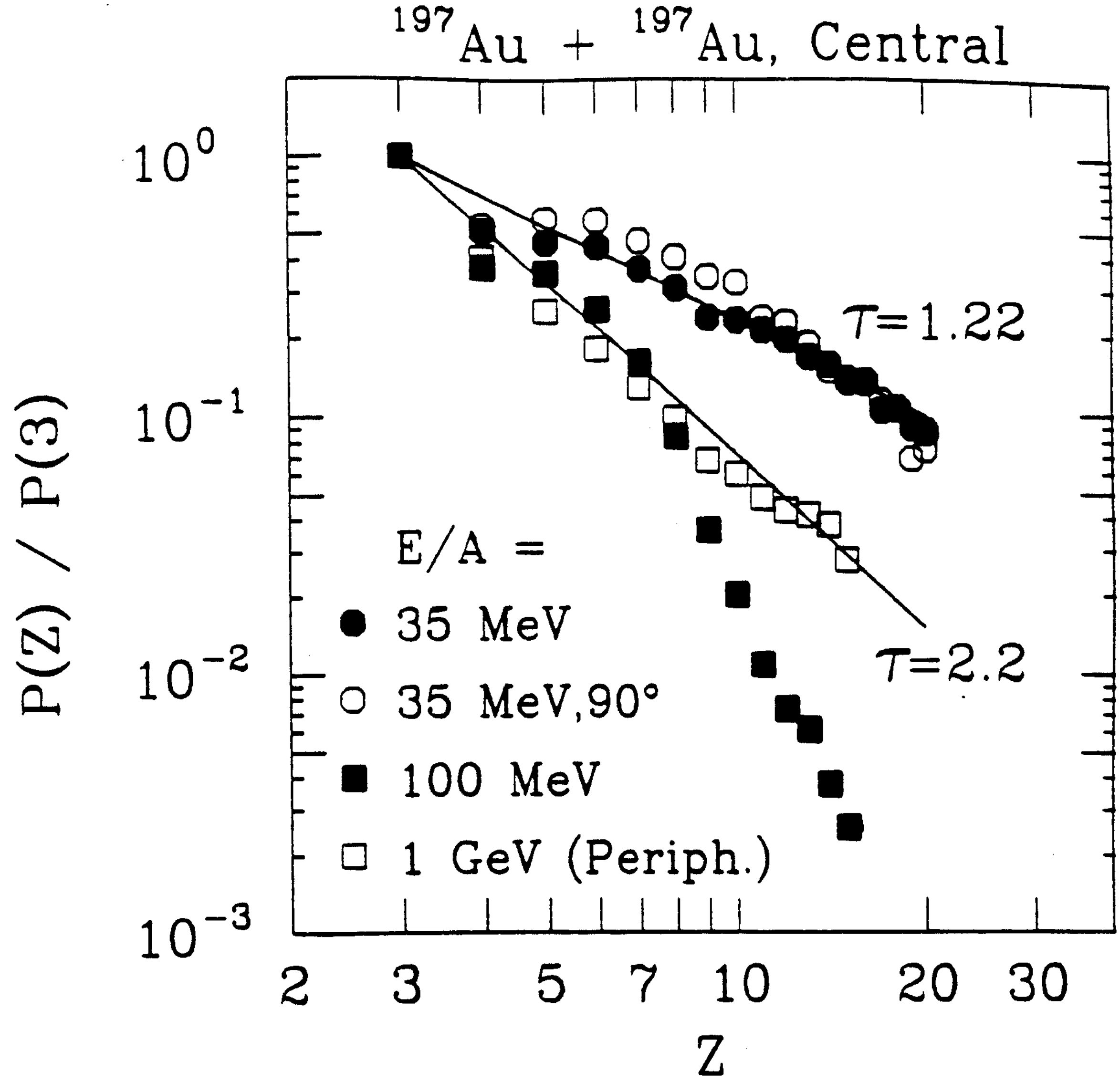

Figure 4.19: Efficiency corrected relative elemental probability distribution P(Z)/P(3) for fragments emitted in central collisions ($\hat{b} \leq 0.1$) for the reaction Au + Au at E/A = 35 MeV (solid points). The corresponding differential distribution at $\Theta_{c.m.} = 90° \pm 20°$ is shown as open points. Relative elemental yields for central collisions at E/A = 100 MeV and peripheral collisions at E/A = 1000 MeV from Ref. [Kund 95] are shown by the solid and open squares, respectively. [Dago 95]

from scaling laws at the critical point of the liquid gas phase diagram. Such small value of τ can be explained with the inclusion of the destabilizing Coulomb interaction in a single spherical source [Dago 95].

The efficiency corrected charge distributions of this central Au + Au collisions are shown in Fig. 4.20. Solid points show the experimental data and the solid lines show the results of SMM predictions for sources with parameters $A_S = 343$, $Z_S = 138$, $E^*_S/A = 6.0$ MeV, $\rho_s = \rho_0/3$ (panel a)) and $A_S = 315$, $Z_S = 126$, $E^*_S/A = 4.8$ MeV, $\rho_s = \rho_0/6$ (panel b)). The dot-dashed and dotted curves present the calculations for thermal excitations E^*_S/A + 1 MeV/A and E^*_S/A - 1 MeV/A, respectively. The calculations reproduce the measured observables, qualitatively and in absolute magnitude [Dago 96a].

Beside reproducing the fragment-fragment correlations and charge distributions, SMM calculations also describe the kinetic energy spectra for this Au + Au reaction to a reasonable extent [Dago 96, Dago 96a]. This model was also successfully applied at higher energies to the interpretation of Au-induced projectile fragmentation reactions [Botv 95]. In these calculations, the temperature and the density are treated as free parameters and have the best fit with a density of $\rho_0/6 \leq \rho \leq \rho_0/3$ and a temperature of $T \approx 6$ MeV for central Au + Au collisions at E/A = 35 MeV.

The good agreement of temperature measurements between excited state population method and double isotope ratio method implies that the ensemble of emitted particles are well described by the assumption of local thermal equilibrium provided that T_{em} is not strongly impact parameter dependent. To investigate this impact parameter dependence using the high statistics of the isotope ratio data, we analyzed the isotope ratios as a func-

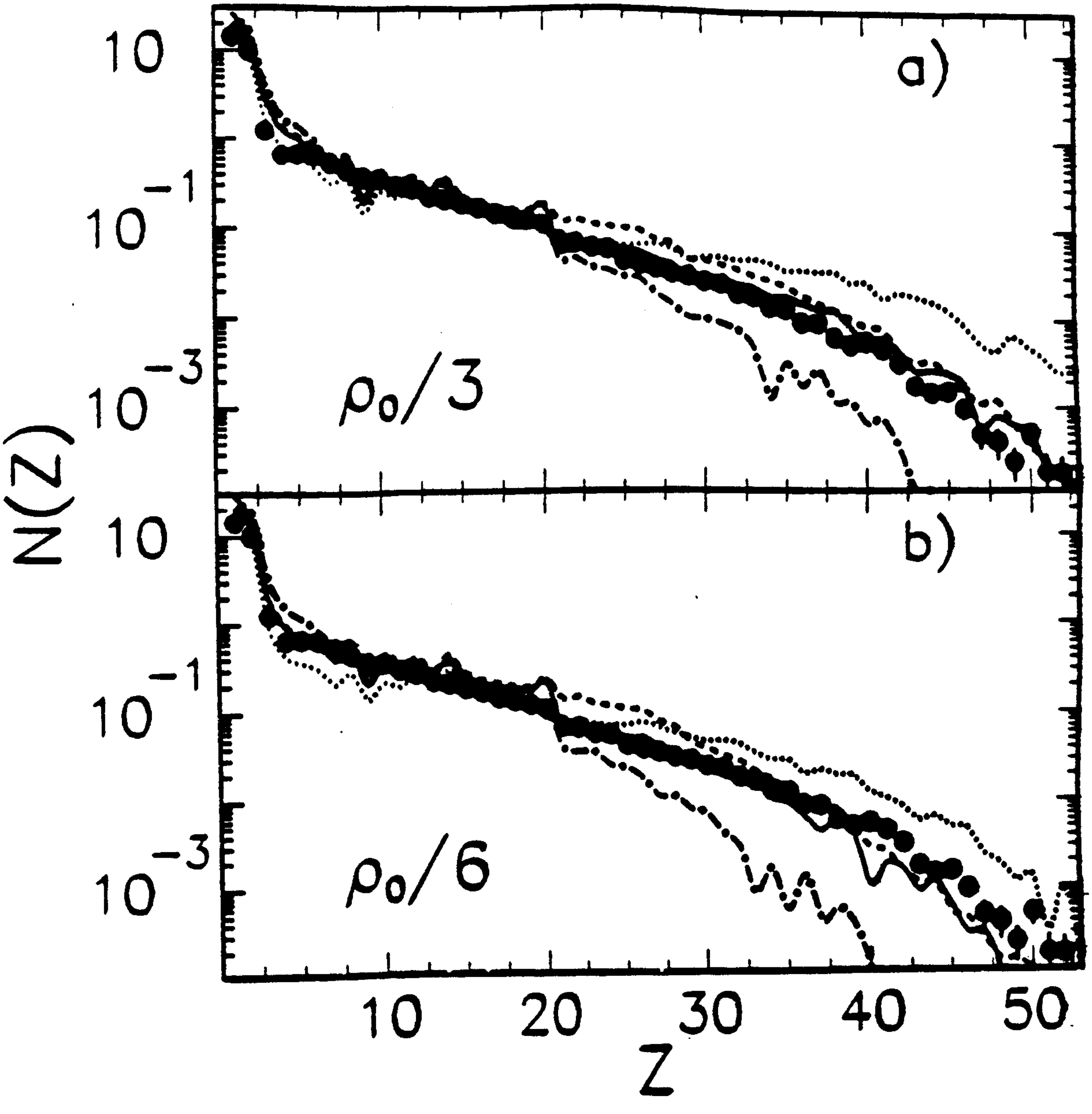

Figure 4.20: Charge distribution N(Z). Solid points show the experimental data and the solid lines show the results of SMM predictions for sources with parameters A_S = 343, Z_S = 138, E_S^*/A = 6.0 MeV, $\rho_s = \rho_0/3$ (panel a)) and A_S = 315, Z_S = 126, E_S^*/A = 4.8 MeV, $\rho_s = \rho_0/6$ (panel b)). Dashed curves are the unfiltered calculations. The dot-dashed and dotted curves present the calculations for thermal excitations E_S^*/A + 1 MeV/A and E_S^*/A - 1 MeV/A, respectively. [Dago 96a]

tion of $\hat{b}$ for gates on $\hat{b}$ of $\hat{b} \approx 0.08, 0.16, 0.25, 0.35, 0.45 \pm 0.05$ as shown in Fig. 4.21, and obtained the approximate values of R_{iso} for $\hat{b} \approx 0$ via the straight line extrapolation.

The minimum in the corresponding χ^2_ν function for $\hat{b} \approx 0$ shown in Fig. 4.22 provides a temperature of $T_{em} = 4.6 \pm 0.4$ MeV, which is similar to the result at $0 \leq \hat{b} \leq 0.45$. This indicates a weak impact parameter dependence of T_{em} consistent with, but not requiring, dominant emission by a central participant source formed by the overlap of projectile and target nuclei. Significant differences between an ideal measurement at zero impact parameter and the present data at $\hat{b} \approx 0$ are rendered unlikely by this weak impact parameter dependence even though impact parameter scales become imprecise at small impact parameters. The extracted value $T_{em} = 4.6 \pm 0.4$ MeV at $\hat{b} \approx 0$ [Huan 97] is compared with SMM calculations and is shown in Fig. 4.23. The temperature obtained from the experiment is about 1.5 MeV lower than the value required by SMM calculations which reproduce fragment-fragment correlations, charge distributions, and the kinetic energy spectra in this reaction [Dago 95, Dago 96, Dago 96a]. While this discrepancy may reflect deficiencies in the thermodynamical assumptions of the Statistical Multifragmentation Model (SMM), it could also reflect the neglect of additional cooling mechanisms such as the Fermi breakup assumed by the SMM [Botv 87, Bond 95] or the emission of particles by the entire system prior to thermal freeze-out [Tsan 96a]. These issues need to be addressed by future experimental and theoretical investigations.

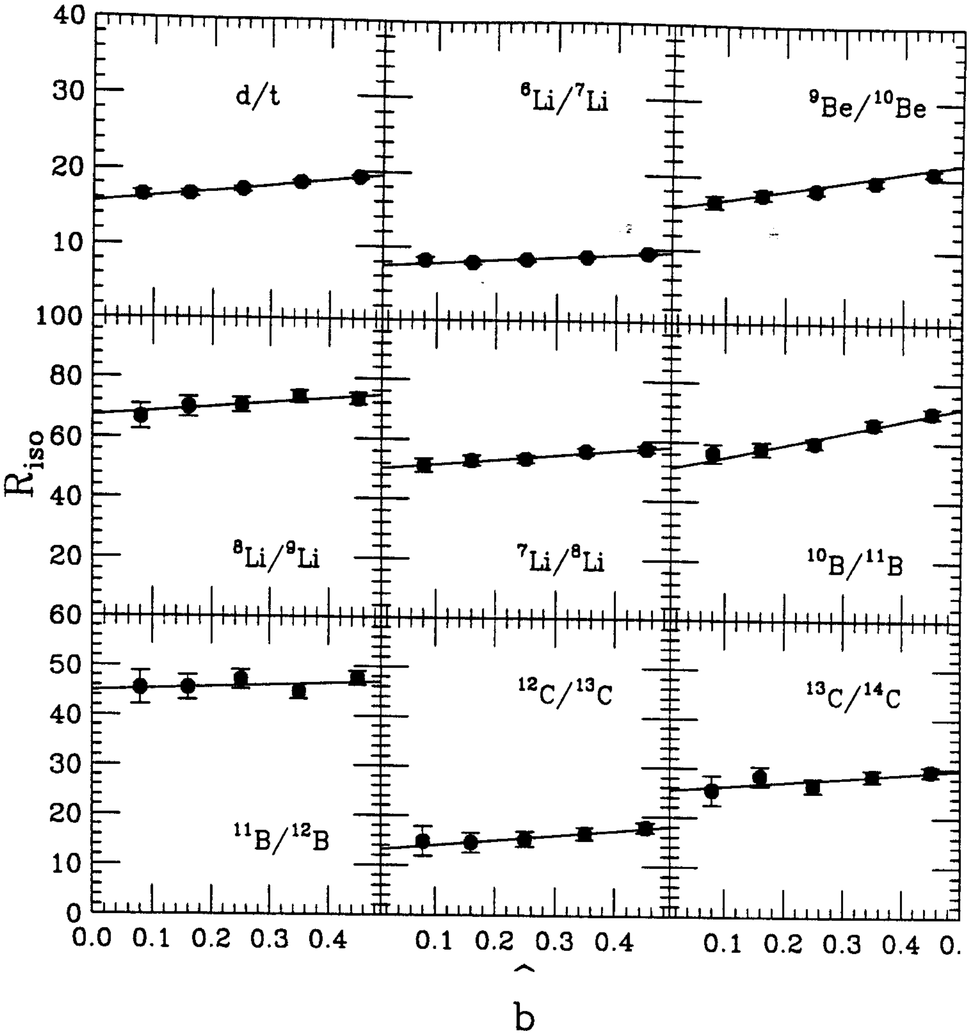

Figure 4.21: The nine isotope ratios as a function of $\hat{b}$ for gates on $\hat{b} \approx 0.08$, 0.16, 0.25, 0.35, and 0.45 of Au + Au collisions at E/A = 35 MeV. The solid lines are the straight line fit.

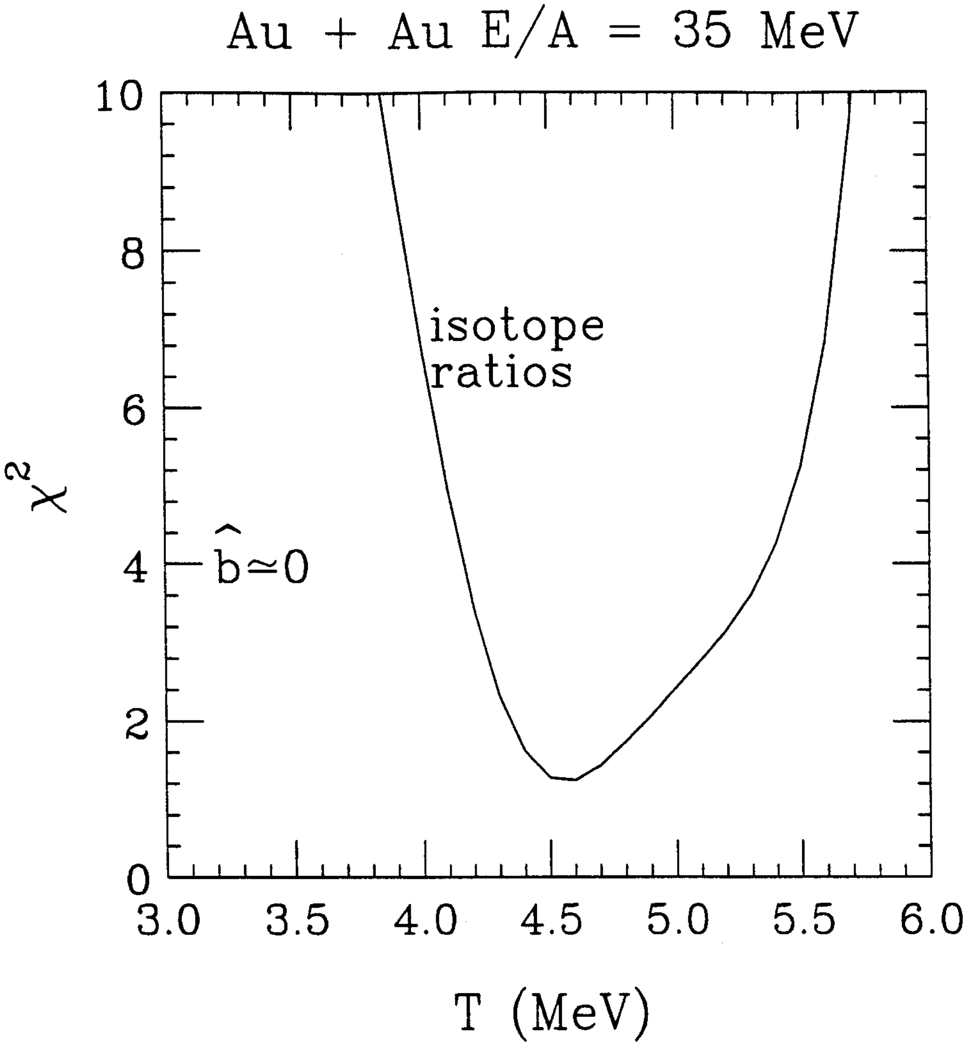

Figure 4.22: Results of the least squares analysis (Eq. 4.5) for the double isotope ratio of Au + Au collisions at b ≈ 0.

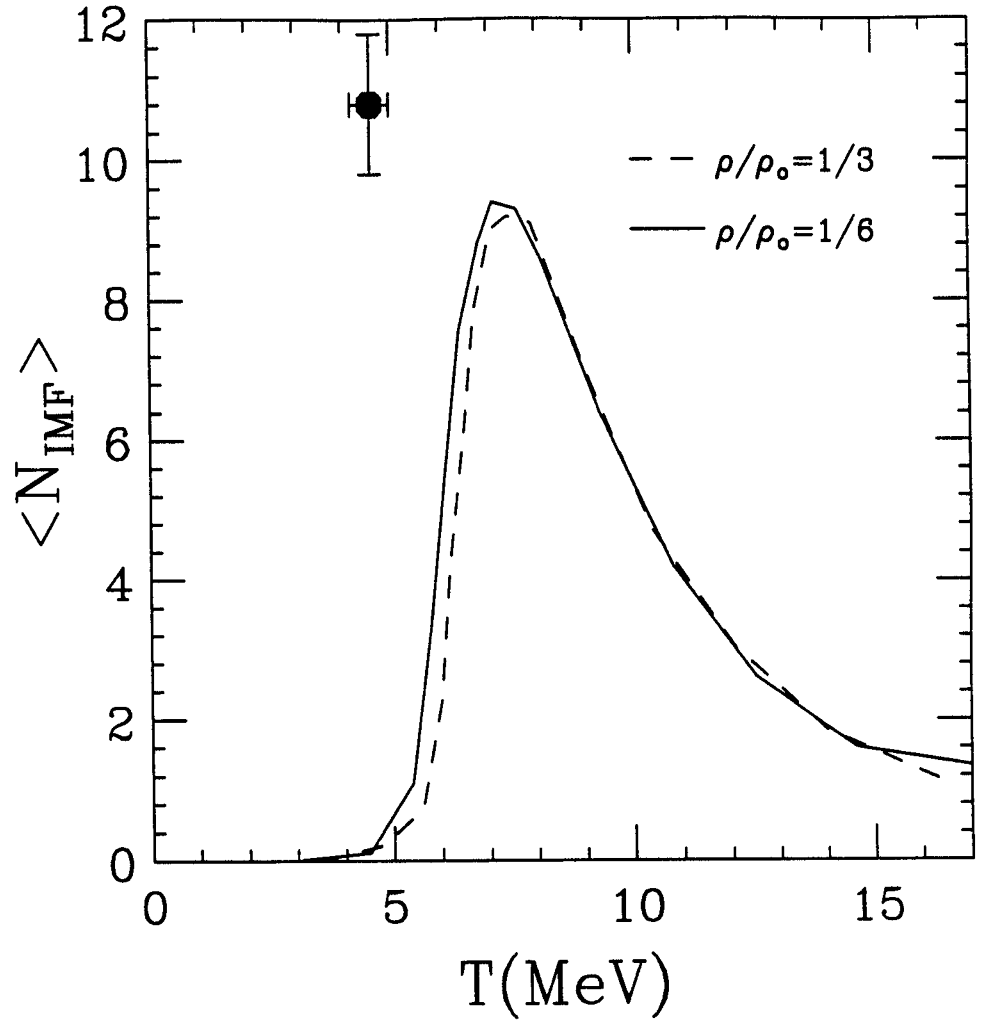

Figure 4.23: The comparison of data (Au + Au at 35 AMeV central collisions) with SMM calculations. The temperature extract from the experiment is about 1.5 MeV lower than the SMM calculations.

4.7 Central Xe + Cu Collisions at E/A = 30 MeV

To investigate the sensitivity of residue temperatures to the nuclear equation of state (EOS), calculations were performed with the Boltzmann-Uehling-Uhlenbeck (BUU) model for Cu + Xe reactions at 30 MeV/nucleon. In these calculations, the BUU equation [Aich 85, Bert 88]

$$\begin{aligned} \frac{\partial f_1}{\partial t} + \mathbf{v} \cdot \nabla_r f_1 - \nabla_r U \cdot \nabla_p f_1 &= \frac{4}{(2\pi)^3} \int d^3k_2 d\Omega \frac{d\sigma_{nn}}{d\Omega} v_{12} \\ &\times [f_3 f_4 (1 - f_1)(1 - f_2) - f_1 f_2 (1 - f_3)(1 - f_4)] \quad (4.7) \end{aligned}$$

was solved via the lattice Hamiltonian method of Lenk and Pandharipande [Lenk 89, Xu 90, Xu 91] using the code of Ref. [Xu 91]. In Eq. (4.7), f is the Wigner transform of the one body density matrix, v_{12} is the relative velocity for the colliding nucleons, $d\sigma_{nn}/d\Omega$ is the in-medium nucleon-nucleon cross section, and U consists of the Coulomb potential and a nuclear potential which contained both isoscalar and symmetry terms. Here, $d\sigma_{nn}/d\Omega$ is chosen to be consistent with the cross section table from the experimental data of nucleon-nucleon collisions [Bald 88]. Calculations were performed for two different isoscalar mean fields, one corresponding to a stiff EOS with a compressibility $K = 380$ MeV and the other to a soft EOS with a compressibility $K = 200$ MeV.

Fig. 4.24 shows the sensitivity of the predicted residue excitation energies as a function of N_{test}, the number of parallel ensembles, over the range $200 \leq N_{test} \leq 800$ for 30 AMeV Cu + Xe collisions at impact parameter b = 0 fm. The thermal energies increase with N_{test}, an effect which may be related to the improvements in the accuracy of the Pauli blocking with increasing N_{test}. This sensitivity to N_{test} becomes very small for $N_{test} \geq 600$. $N_{test} = 800$ was used in this BUU calculation; larger N_{test} consumes too much CPU time to allow exploration of the relevant issues.

The time evolution of the thermal energy of BUU calculations is shown in Fig. 4.25 with the stiff EOS (top panel) and soft EOS (bottom panel) at $b = 0$ fm and $N_{test} = 800$. There is a global maximum at $t \approx 60 fm/c$ for both stiff EOS and soft EOS. This is an artifact of the initial momentum distribution, in which the longitudual velocities of the projectile and target nuclei cancel each other, causing a minimum in the computation of the collective energy. The second maximum occurs at $t \approx 120 fm/c$ for the stiff EOS and $t \approx 160 fm/c$ for the soft EOS after the initial pre-equilibrium stages of the collision; this maximum provides an estimate of the maximum or initial thermal excitation energy of the reaction residue. The corresponding time provides an estimate of the freeze-out time t_{free} which marks the cessation of pre-equilibrium emission. After this second maximum the thermal excitation energy decreases slowly with time, reflecting the well studied evaporative cooling mechanisms operate in hot equilibrated nuclei.

To obtain the relation between residue temperature and excitation energy, we approximate the thermal excitation energy of the residue by integrating the Fermi-gas expression $\varepsilon^*(T, \varepsilon_F(\rho(\mathbf{r})))$ for the excitation energy per nucleon over the nuclear density and by equating this value to the thermal energy provided by the numerical simulations [Xu 93, Xu 94a],

$$E^*_{the} = \int_C d^3r \{\rho_p \varepsilon^*(T, \varepsilon_F(\rho_p)) + \rho_n \varepsilon^*(T, \varepsilon_F(\rho_n))\} \tag{4.8}$$

Here, ρ_p and ρ_n are the matter densities for protons and neutrons, respectively. $\varepsilon^*(T, \varepsilon_F(\rho))$ can be further approximated when at low temperature limit, and E^*_{the} can be written as

$$E^*_{the} = aT^2 \tag{4.9}$$

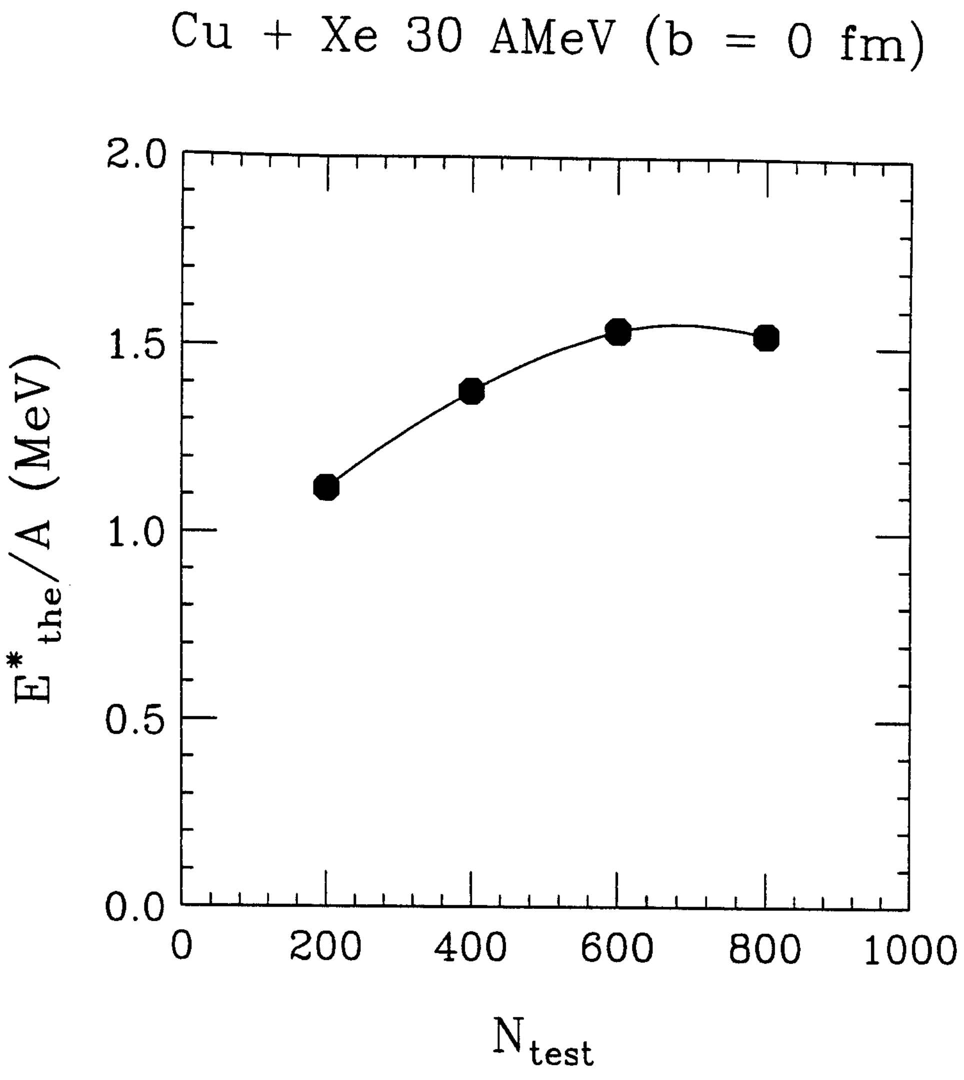

Figure 4.24: The residue excitation energies as a function of N_{test} for BUU calculations at zero impact parameters (Cu + Xe reactions)

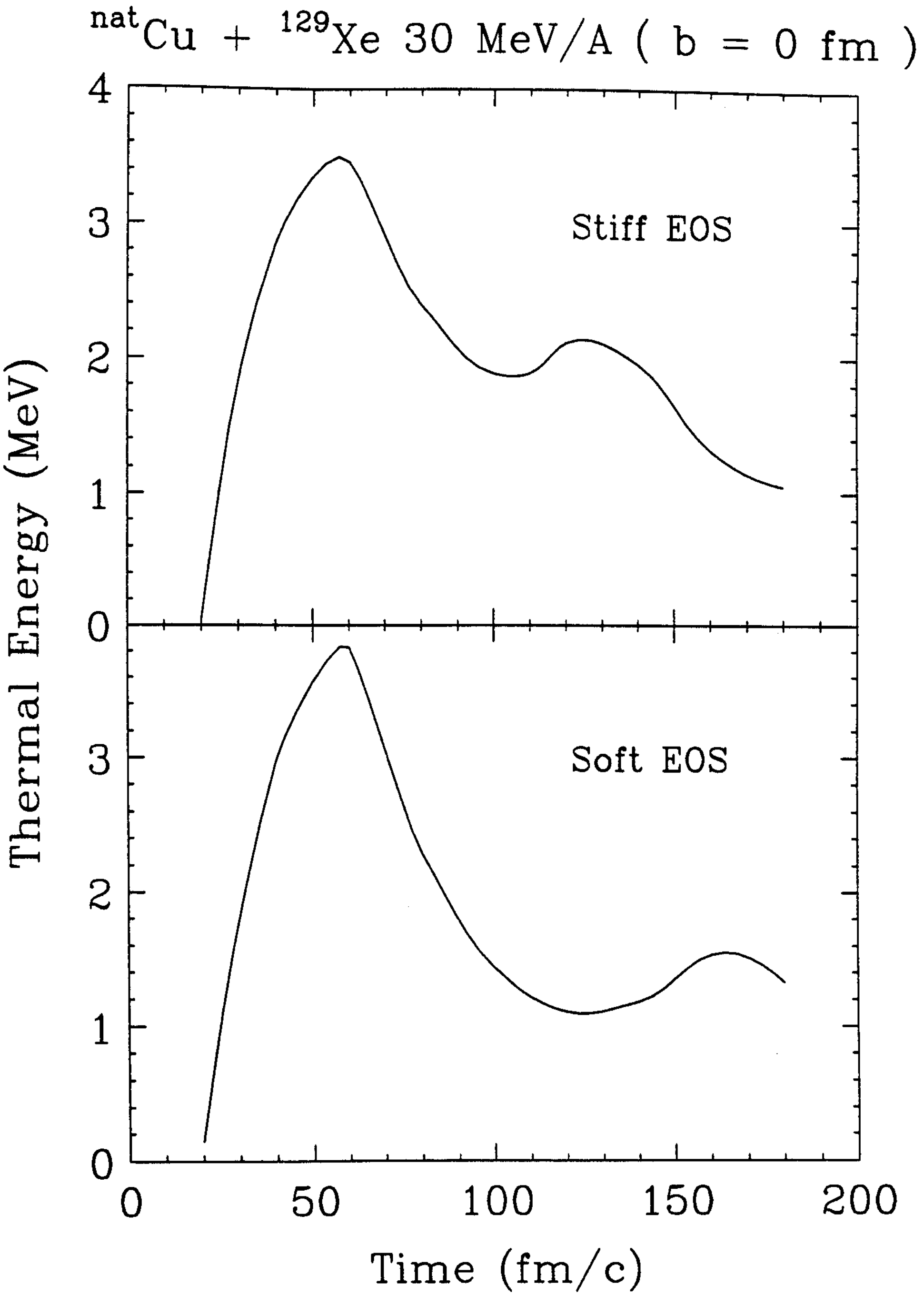

Figure 4.25: The time evolution of the thermal energy of BUU calculations for Cu + Xe 30 AMeV, using stiff EOS (top panel) and soft EOS (bottom panel)

with the level density parameter a is given by

$$a = \frac{m}{3\hbar^2}\left(\frac{3\pi^2}{2}\right)^{1/3}\int_C d^3r\rho^{1/3}(\mathbf{r}) \tag{4.10}$$

To get Eq. (4.9) and Eq. (4.10), Fermi energies for protons and neutrons are assumed to be equal, and the local density approximation

$$\varepsilon_F(\rho) = \frac{\hbar^2}{2m}\left(\frac{3\pi^2\rho}{2}\right)^{2/3} \tag{4.11}$$

is used. In the calculations, the level density parameter is evaluated from the density distribution produced by the BUU calculations at freeze-out. A value of level density parameter $a \approx A/8 - A/9$ is obtained from the calculations.

Significantly larger values of residue temperatures and thermal excitation energies are obtained for calculations with the stiff EOS. The observed dependence upon the equation of state is partly due to the fact that pre-equilibrium emission is suppressed in calculations with the stiff EOS because the stiff EOS has a larger surface restoring force, and systems simulated with the stiff EOS remain closer to normal nuclear matter density and emit fewer pre-equilibrium test particles. Also, the stiff EOS has a larger sound velocity, leading to an earlier thermal freeze-out and consequently less time for cooling via pre-equilibrium emission.

The comparisons of data with two different equation of state are shown in Fig. 4.26. Independent of impact parameter, the residue temperatures calculated from the stiff EOS are about 0.7 MeV higher than those calculated from the soft EOS. The data show little impact parameter dependence and are closer to the soft equation of state. However, cooling dynamics plays an important role in the determination of emission temperature [Xi 97].

This cooling effect was not included in our BUU calculations and further investigation will be necessary to have better comparison for the data with the nuclear equation of state.

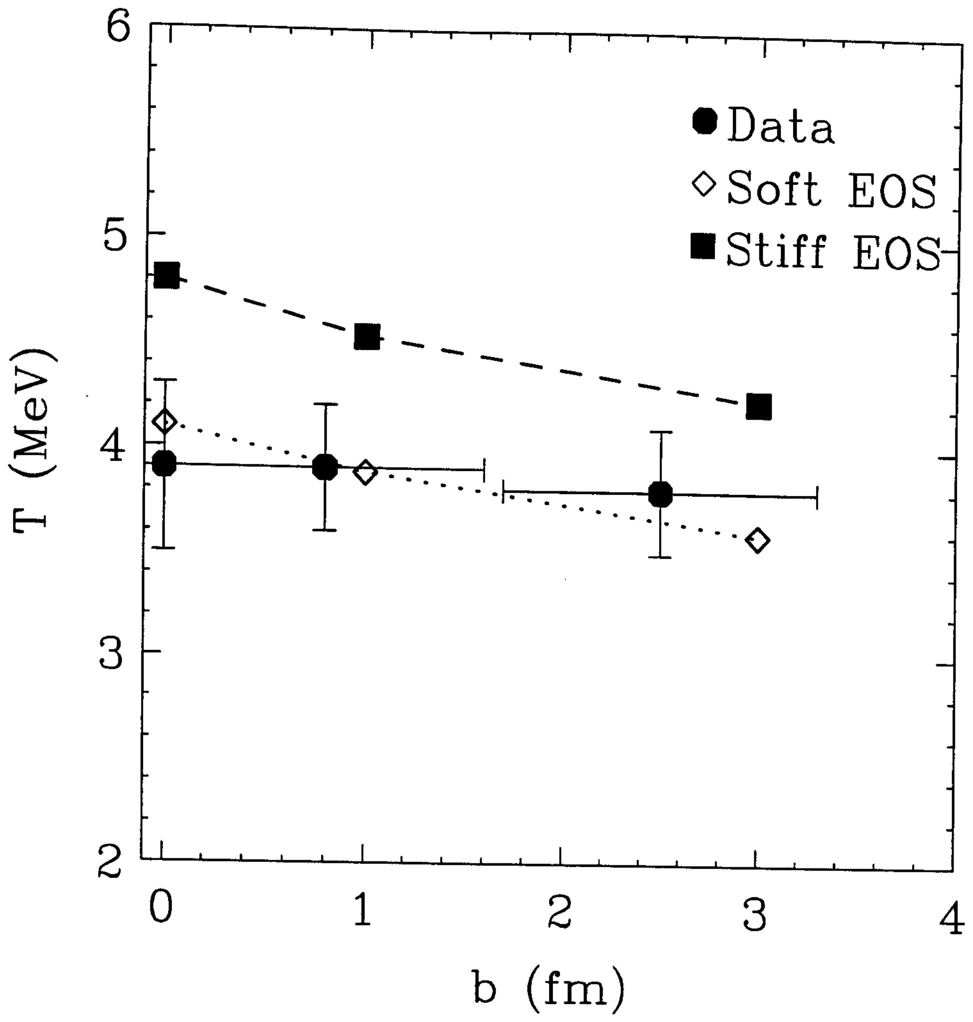

Figure 4.26: Residue temperatures for Xe + Cu 30 AMeV data and BUU calculations with soft and stiff equation of state. Solid circles are the data. Open diamonds are the BUU calculations using soft EOS. Solid diamonds are the BUU calculations using stiff EOS. Lines are drawn to guide the eye.

Chapter 5

Directed Transverse Flow for Kr + Au Reactions

5.1 Introduction

The determination of the equation of state of nuclear matter is one of the main objectives in relativistic heavy-ion physics. Insight into the high density equation of state has been mainly gained through the study of collective flow. The flow was initially described years ago via the macroscopic thermodynamic/hydro-dynamical picture [Stöc 80] and via the more microscopic cascade model [Cugn 80]. As two nuclei collide at incident energies of E/A $\geq$ 200 MeV, the pressure and density increase in the interaction region, and after an initial compression, systems begin to expand rapidly. At zero impact parameter, the expansion is azimuthally symmetric and is sometimes reflected to as a "radial expansion" or "radial flow". At a finite impact parameter, there is an inherent asymmetry in the pressure, which results in the flow of matter in the direction of lowest pressure both out of the reaction plane where it is sometimes called "squeeze-out" and in the reaction plane where it is often called "directed transverse flow". The amount of transverse flow is directly related to the incompressibility of the nuclear equation of state and transport properties of the nuclear medium [Bert 87]. While radial flow is not very sensitive to the nuclear equation of state [Lisa 95], directed transverse flow has shown to be sensitive to both the incompressibility and other transport properties of the nuclear matter such as momentum dependence of the mean field potential or the in medium nucleon-nucleon cross section [Moli 85, Stöc 86, Bert 87, Dani 88, Gutb 89, Peil 89, Pan 93, Peil 94].

Heavy ion collisions provide key information on the interplay of two different kinds of forces. At low incident energies (E/A ≤ 50 MeV) and if the total charge of the system is not too large, the attractive nuclear mean field force dominates and particles are emitted preferentially to negative scattering angles [Tsan 86]. At higher incident energies (E/A ≥ 100 MeV), the mean field becomes less attractive and eventually repulsive, collisions by the repulsive nucleon-nucleon (n-n) residual interaction prevail and particles are emitted preferentially to positive scattering angles. Between these two extremes there is a beam energy (balance energy) E_{bal}/A for which the transverse flow disappears [Krof 89, Ogil 90, Sull 90, Zhan 90, Krof 91, Krof 92, West 93]. Systematic measurements of collisions between equal mass projectile and target nuclei indicate that E_{bal} scales with the total mass as $A^{-1/3}$ [West 93]. Transport model calculations show the balance energy is sensitive to the in-medium nucleon-nucleon cross sections but insensitive to the incompressibility of the nuclear equation of state [West 93].

Most transverse flow measurements have been performed for mass symmetric ($A_{projectile} = A_{target}$) systems. Such systems have the advantage that the center of mass frame is more clearly defined and it is easier to correct data for deficiencies in the detector acceptance. However, the transverse flow measured in mass symmetric systems have been shown to be sensitive to both the incompressibility of the nuclear EOS and to the momentum dependent mean field, so that the determinations of incompressibility of the nuclear equation of state have some ambiguities [Pan 93]. Mass asymmetric systems, on the other hand, retain a sensitivity to the momentum dependence of the nuclear mean field, but the sensitivity to the incompressibility of the nuclear EOS is reduced because very large densities are not achieved in such collisions [Pan 93, Huan 96]. Measurements of transverse flow for mass asymmetric systems such as Kr + Au reactions can help us to constrain the form of the momentum dependence of the nuclear mean field and therefore remove the ambiguity on the determination of the incompressibility from the data for mass symmetric systems.

Discussions of impact parameter selection and azimuthal correlations for the ^{84}Kr + ^{197}Au reactions will be given in Section 5.2. In Section 5.3, techniques for the extraction of directed transverse flow will be discussed. In Section 5.4, the experimental data for Kr + Au reactions at E/A = 200 MeV are compared to BUU calculations.

5.2 Impact Parameter Selection and Azimuthal Correlations for ^{84}Kr + ^{197}Au Reactions

To extract the directed transverse flow in nucleus-nucleus collisions, one must determine the impact parameter b and sometimes the reaction plane as well. For this dissertation, a "reduced" impact parameter $\hat{b}$ is constructed from the charged particle multiplicity by means of the geometric formula Eq. (4.1) as described in Section 4.2 and Ref. [Phai 92]. The measured charged particle multiplicity distributions for ^{84}Kr +^{197}Au reactions at E/A = 35 - 400 MeV are shown in Fig. 5.1. Similar to Fig. 4.1, the charged particle multiplicity distributions for Kr + Au reactions exhibit a structureless plateau and a near exponential falloff at the highest multiplicities. The corresponding reduced impact parameter $\hat{b}$ obtained via Eq. (4.1) is shown at the top of each panel.

Besides directed transverse flow and radial flow, a form of "rotational" flow is often observed in heavy ion reactions at low incident energies when the particle emission is dominated by the attractive mean field potential. In general, particle emission from a rotating system is focused in the plane perpendicular to the angular momentum vector, i.e. for "rotational" flow the emission will be enhanced in the reaction plane [Chit 86].

Azimuthal correlations have been shown to be sensitive to both directed transverse flow and rotational flow [Tsan 84, Gutb 87, Wils 90] and hence provide a simple method to probe for collective flow [Tsan 84a, Chit 86a, Fiel 86, Tsan 90, Wang 91, Phai 92]. One can define an azimuthal correlation function $[1 + R(\Delta\phi)]$ by the ratio [Tsan 90, Phai 92]

$$\left.\frac{Y(\Delta\phi)}{Y'(\Delta\phi)}\right|_{\hat{b}} = C[1 + R(\Delta\phi)]|_{\hat{b}} \tag{5.1}$$

Here, $Y(\Delta\phi)$ is the coincidence yield of two identical particles emitted at a relative angle $\Delta\phi$ in collisions selected by a specific cut on reduced impact parameter $\hat{b}$; $Y'(\Delta\phi)$ is the background yield constructed by taking each of the two particles from different coincidence events, where each particle is selected by the same cut on the reduced impact parameter as for the coincidence events; C is a normalization constant such that the average value of the

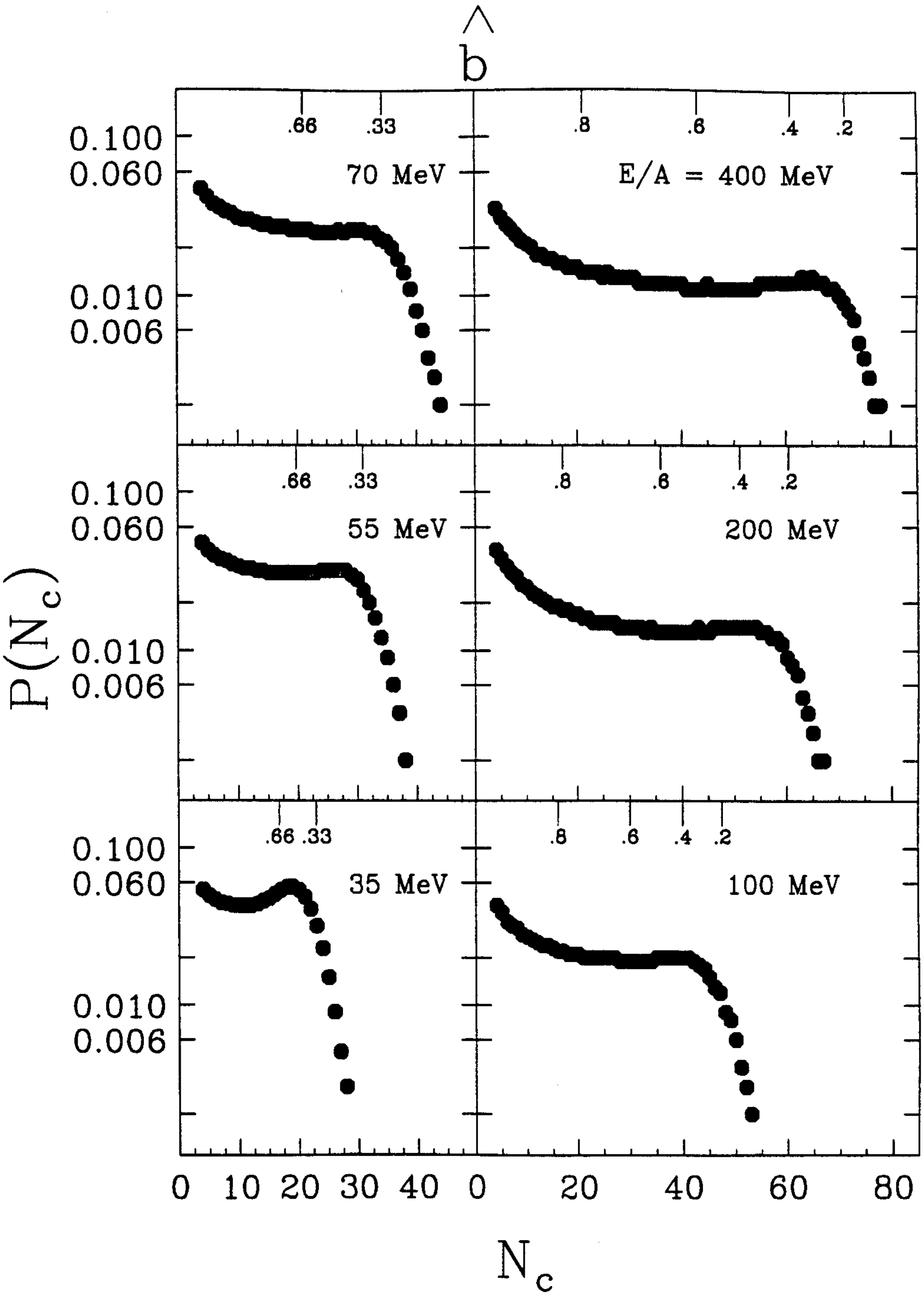

Figure 5.1: The probability distributions for the charged particle multiplicity measured for ^{84}Kr +^{197}Au collisions at E/A = 35 - 400 MeV. The corresponding reduced impact parameter $\hat{b}$ is shown on the top of each panel.

correlation $1 + R(\Delta\phi)$ is one.

Such correlation functions have the advantages that they do not require knowledge of the reaction plane [Wang 91] and systematic uncertainties associated with detector acceptance and efficiency can be minimized. Fig. 5.2 shows the azimuthal $\alpha - \alpha$ correlation functions for ^{84}Kr + ^{197}Au reactions at 35 - 200 MeV/nucleon. The two α particles are selected to be $v_{1z} > v_c$ and $v_{2z} < v_c$ to eliminate the effects of ^{8}Be decay, which could lead to enhanced values of the correlation function at small $\Delta\phi$ for α's emitted to nearly the same angle, and v_{iz} is the component of the velocity of the ith α particle in the beam direction; v_c is the center of mass velocity. At low incident energies where the attractive mean field interaction dominates, charged particles are emitted mainly in the reaction plane [Wils 90, Tsan 90, Tsan 91, Tsan 92] and the correlation functions exhibit a characteristic "V" shape which flattens with increasing incident energies. This "V" shape occurs because mean field attraction dictates a strong preference for the emission of both α particles in the reaction plane; this effect is often called "rotational flow". There is a left-right anisotropy of the correlations which increases with increasing incident energy. This anisotropy may be related to the directed transverse flow. The correlations in Fig. 5.2 are fitted with the following function:

$$1 + \lambda_1 \cos(\Delta\phi) + \lambda_2 \cos(2\Delta\phi) \tag{5.2}$$

where λ_1 and λ_2 are treated as free parameters. Large values of λ_2 may indicate some "rotational" flow and λ_1 may indicate some directed transverse flow [Lace 93]. For an isotropic distribution, $\lambda_1 = \lambda_2 = 0$.

Fig. 5.3 presents the values of the parameters λ_1 and λ_2, extracted for ^{84}Kr + ^{197}Au

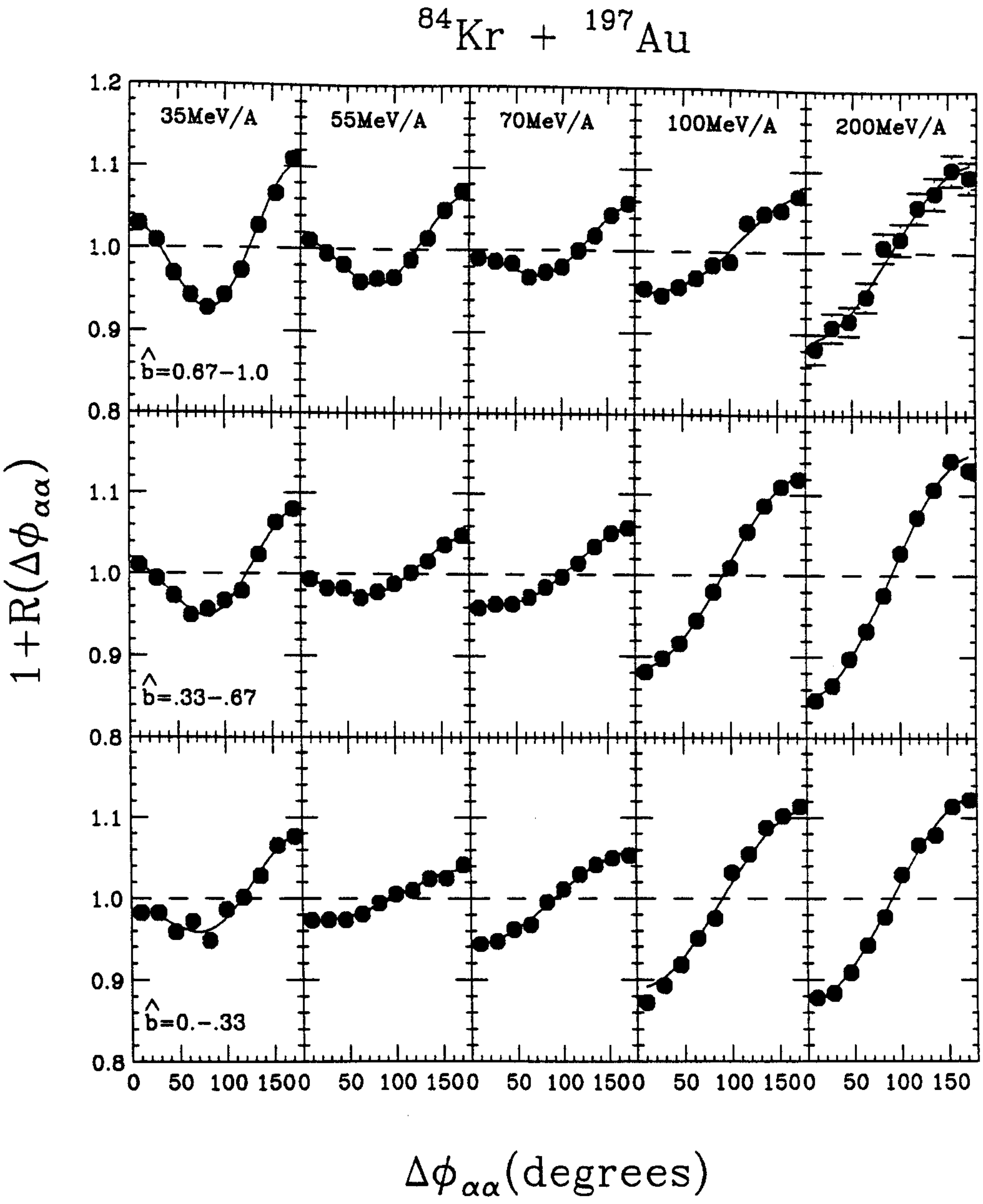

Figure 5.2: α - α correlation functions for Kr + Au reactions at E/A = 35 - 200 MeV for three impact parameter gates. The points are the experimental data and the solid lines are the fits to the parameterization given by Eq. (5.2).

collisions at incident energies ranging from 35 to 200 AMeV at three gates on reduced impact parameter $\hat{b} < 0.33$ (central), $0.33 < \hat{b} < 0.67$ (mid-central), and $0.67 < \hat{b}$ (peripheral). At all incident energies, λ_2 increases as a function of reduced impact parameter as one might expect if non-zero λ_2 is in some sense proportional to angular momentum as implied by its connection to "rotational" flow. On the other hand, λ_2 decreases with incident energy and disappears at 100 - 200 AMeV, consistent with mean field attraction playing a negligible role at all impact parameters for incident energies $E/A > 100$ - 200 MeV. The absolute magnitude of the directed flow parameter λ_1 increases with incident energy for energies greater than 70 AMeV. This may indicate the increasing importance of repulsive momentum transfers due to nucleon-nucleon collisions at higher incident energies. Note that λ_1 changes little between 35 and 70 AMeV and never vanishes. This probably indicates that the mean field attraction is roughly balanced by the repulsive effect of nucleon-nucleon collisions and one may be observing non-zero values for λ_1 that result simply from momentum conservation effects between the 2α particles.

Although azimuthal correlation functions provide a clear picture of the evolution of reaction dynamics, because quantitative correlation functions can not presently be accurately calculated theoretically, these data can not provide any quantitative information about the compressibility of the mean field or its momentum dependence. In the next section, however, an alternative correlation technique will be presented that provides quantitative information that can be compared to theoretical predictions, and such comparisons will be performed at $E/A = 200$ MeV for ^{84}Kr + ^{197}Au collisions.

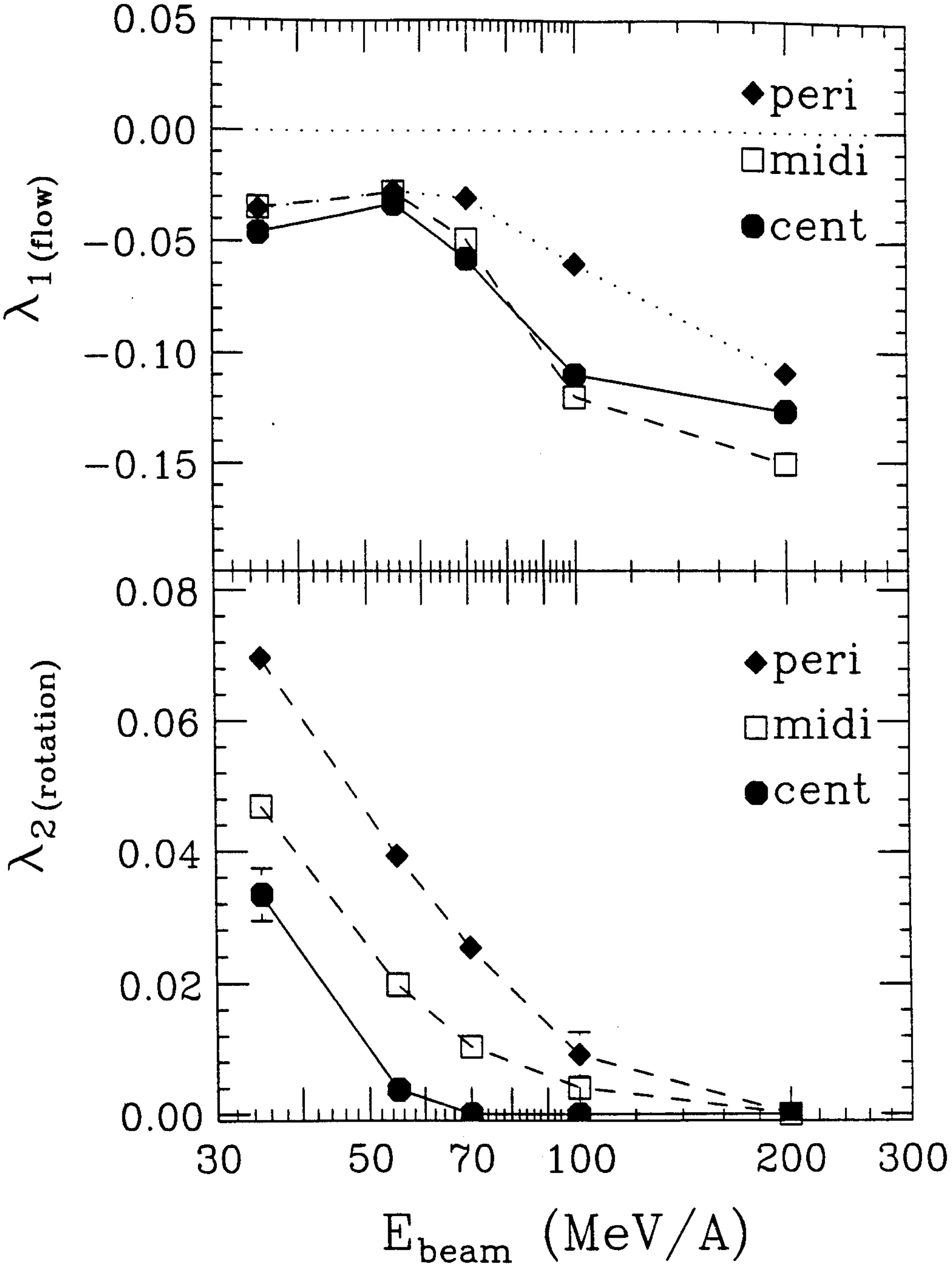

Figure 5.3: The parameters λ_1 and λ_2 obtained by fitting the angular correlations in Fig. 5.2 for ^{84}Kr + ^{197}Au collisions using Eq. (5.2) as a function of incident energy.

5.3 Techniques for Transverse Flow Measurements

Initial conditions for a heavy ion collision can be constructed from the knowledge of the impact parameter and the reaction plane. The reaction plane is the plane which contains the relative displacement and relative momentum of the projectile and target nuclei [Bert 87, Welk 88, Tsan 89, Xu 90]. Information about the orientation of the reaction plane can be obtained from the azimuthal anisotropies of the emitted particles. At higher incident energies, E/A $\geq$ 100 MeV, such anisotropies may occur due to directed transverse flow of nuclear matter caused by compressional effects [Dani 85, Dani 88]. At lower incident energies, E/A $\leq$ 100 MeV, azimuthal anisotropies can result from a collective deflection of light particles to negative angles caused by the attractive nuclear mean field, and manifested experimentally, either by "rotational" flow or directed transverse flow or both [Tsan 84, Tsan 84a, Chit 86, Tsan 86, Tsan 88, Tsan 90, Wils 90].

Very often experimentalists have deduced a reaction plane from the detected particles by using the transverse momentum method developed by P. Danielewicz and G. Odyniec [Dani 85]. In this method, a vector **Q** is constructed from the transverse momenta $\mathbf{p}_\nu^\perp$ of detected particles:

$$\mathbf{Q} = \sum_{\nu=1}^{M} \omega_\nu \mathbf{p}_\nu^\perp \tag{5.3}$$

where ν is a particle index; ω_ν is a weighting factor and $\omega_\nu = 0$ for pions. For baryons, one often chooses $\omega_\nu = 1$ for $y_\nu > y_c + \delta$, $\omega_\nu = -1$ for $y_\nu < y_c - \delta$, and $\omega_\nu = 0$ otherwise. Here, y_ν is the rapidity of particle ν; y_c is the center mass rapidity, and δ is inserted to remove particles from mid-rapidity which do not contribute to the determination of the reaction plane but do contribute to unwanted fluctuations. The direction of the vector **Q** is then used to estimate the projectile side of the reaction plane in an event; by convention it's usually taken to be the positive P_x axis. To obtain the P_x value for a specific detected particle, the selected particle is excluded from the determination of **Q** to remove auto-correlations. Then the P_x for the selected particle is obtained by projecting the momentum of the selected particle on the **Q** axis.

This transverse momentum method has been successfully used in high energy heavy ion collisions to determine the reaction plane and consequently values for P_x. However, when the incident energy is low (E/A < 100 MeV), the multiplicities of emitted particles are lower and the flow may also be small, therefore **Q** can have large fluctuations. Thus at low incident energies, the reaction planes determined from the transverse momentum method have a rather large uncertainty. To reduce the uncertainties in the flow measurements at low incident energies due to the reaction plane dispersion, other methods were developed.

When the directed flow values are small but the rotational flow values are not, one may apply the tensor method [Tsan 91]. For illustration, consider the transverse momentum tensor for an event

$$A_{nm} = \sum_i (p_{in} p_{im}) \omega_i \tag{5.4}$$

where $(p_{i1}, p_{i2}) = (p_i \sin\theta_i \cos\phi_i, p_i \sin\theta_i \sin\phi_i)$; p_i is the momentum of particle i. θ_i and ϕ_i are the polar angle and the azimuthal angle of that particle; and ω_i is the weighting factor which can depend on the masses of the particles. Here we assume $w_i = 1$.

Assuming a rotational flow, the reconstructed reaction plane will be the principle axis of this ellipse. The transverse momentum tensor can be rotated so that the principle axis lies along the x axis

$$A'_{nm} = \sum_i (p'_{in} p'_{im}) \tag{5.5}$$

where $(p'_{i1}, p'_{i2}) = (p_{i1} \cos \Phi + p_{i2} \sin \Phi, p_{i2} \cos \Phi - p_{i1} \sin \Phi)$ is the transverse momentum of particle i projected on the reaction plane, and Φ denotes the azimuthal angle of the reaction plane.

The most probable orientation of the reaction plane corresponds to the maximum of A'_{11}

$$\frac{dA'_{11}}{d\Phi} = 0 \tag{5.6}$$

The azimuthal orientation Φ of the constructed reaction plane is then given by the equation

$$\tan(2\Phi) = \frac{\sum_{i=1}^{N-1} p_i^2 \sin^2 \theta_i \sin 2\phi_i}{\sum_{i=1}^{N-1} p_i^2 \sin^2 \theta_i \cos 2\phi_i} \tag{5.7}$$

The tensor method does not give the sign of the transverse momentum, so the **Q** vector from transverse momentum method can be used to provide the required direction. Note that Tsang *et al.* [Tsan 91] have shown that Eq. (5.7) is mathematically equivalent to the method used by W.K. Wilson *et al.* [Wils 90] who proposed to reconstruct the orientation of the reaction plane by minimizing the sum of the squares of the momentum components perpendicular to the reaction plane.

One disadvantage of calculating $\langle P_x \rangle$ from either the transverse momentum analysis or the tensor method is the requirement that the reaction plane must be determined in either of these methods. The constructed reaction planes fluctuate about the true reaction plane from event to event. These fluctuations introduce uncertainties in the extracted transverse momenta. Corrections can be applied for this reaction plane dispersion, but can be large, especially when the flow is small and the dispersion large [Sull 92].

To avoid the uncertainties introduced by reaction plane reconstruction, an improvement upon transverse momentum analysis techniques has been proposed which involves constructing appropriate mean products of the measured momenta [Dani 88]. By averaging the inner product $p_\nu^\perp(y_\nu) \cdot p_\mu^\perp(y_\mu)$ of the transverse momentum $p_\nu^\perp(y_\nu)$ of a particle of type ν at rapidity y_ν with the transverse momentum $p_\mu^\perp(y_\mu)$ of a particle of type μ at rapidity y_μ, for example, the random fluctuations of the transverse momenta about the collective mean values average to zero. Choosing a coordinate system in which the non-vanishing mean collective transverse momenta lie along the x axis, this average inner product factorizes into the expression:

$$\langle p_\nu^\perp(y_\nu) \cdot p_\mu^\perp(y_\mu)\rangle \simeq \langle p_\nu^x(y_\nu)\rangle\langle p_\nu^x(y_\nu)\rangle \tag{5.8}$$

Momentum conservation gives rise to further correlations between particle transverse momenta, modifying Eq. (5.8) to read:

$$\langle p_\nu^\perp(y_\nu) \cdot p_\mu^\perp(y_\mu)\rangle \simeq \langle p_\nu^x(y_\nu)\rangle\langle p_\nu^x(y_\nu)\rangle - \alpha\langle {p_\nu^\perp}^2(y_\nu)\rangle\langle {p_\mu^\perp}^2(y_\mu)\rangle \tag{5.9}$$

where $\alpha^{-1} \simeq \langle \sum_\mu {p_\mu^\perp}^2\rangle$ and the sum runs over the entire distribution of emitted particles. Since the experimental detection efficiency is less than unity, the value for α^{-1} used in Eq. (5.9) was obtained by rescaling the experimental value with the ratio of the total to the detected charge. For small relative velocities, final state interactions such as the Coulomb repulsion and resonance excited states introduce additional correlations that can influence the extraction of the mean transverse momenta via Eq. (5.9). These effects can be taken into account using the prescription below,

$$\langle p_\nu^\perp(y_\nu)\cdot p_\mu^\perp(y_\mu)\rangle = \langle\frac{p_\nu^\perp(y_\nu)\cdot p_\mu^\perp(y_\mu)}{1+R(v_{red})}\rangle^{obs} - \langle p_\nu^\perp(y_\nu)\rangle^{lab}\cdot\langle p_\mu^\perp(y_\mu)\rangle^{lab} \tag{5.10}$$

where $\langle(p_\nu^\perp(y_\nu)\cdot p_\mu^\perp(y_\mu))/(1+R(v_{red})\rangle^{obs}$ is the mean product of transverse momentum of coincidence with final state correction factor $1+R(v_{red})$, $\langle p_\nu^\perp(y_\nu)\rangle^{lab}$ is the average transverse momentum of singles, and $1+R(v_{red})$ is the reduced velocity correlation functions which will be described later.

The final state interaction can be measured from reduced-velocity two-fragment correlation functions [Kim 92]. The reduced-velocity correlation function $1+R(v_{red})$ is defined as [Kim 92]

$$1+R(v_{red}) = C\frac{N_{corr}(v_{red})}{N_{uncorr}(v_{red})} \tag{5.11}$$

where v_{red} represents the reduced velocity of the pair,

$$v_{red} = v_{rel}/\sqrt{Z_1+Z_2} \tag{5.12}$$

Here, v_{rel} is the relative velocity, Z_i is the charge of fragment i, $N_{corr}(v_{red})$ is the measured coincidence yield and $N_{uncorr}(v_{red})$ is the background yield constructed by using fragments from different events [Lisa 91]. C is a normalization constant such that the average value of the correlation $1+R(\Delta\phi)$ is one.

The reduced-velocity correlation functions were measured for proton, deuteron, triton, ^{3}He, α, Li, Be, and B. The correlation functions for p + X and $\alpha + X$ are separated from other particles because they include many resonances. Fig. 5.4 shows the $\alpha + X$ correlation functions. The enhancements due to the resonance states of (α, X) can be seen in the correlation functions. Fig. 5.5 shows the $A + X$ correlation functions where A

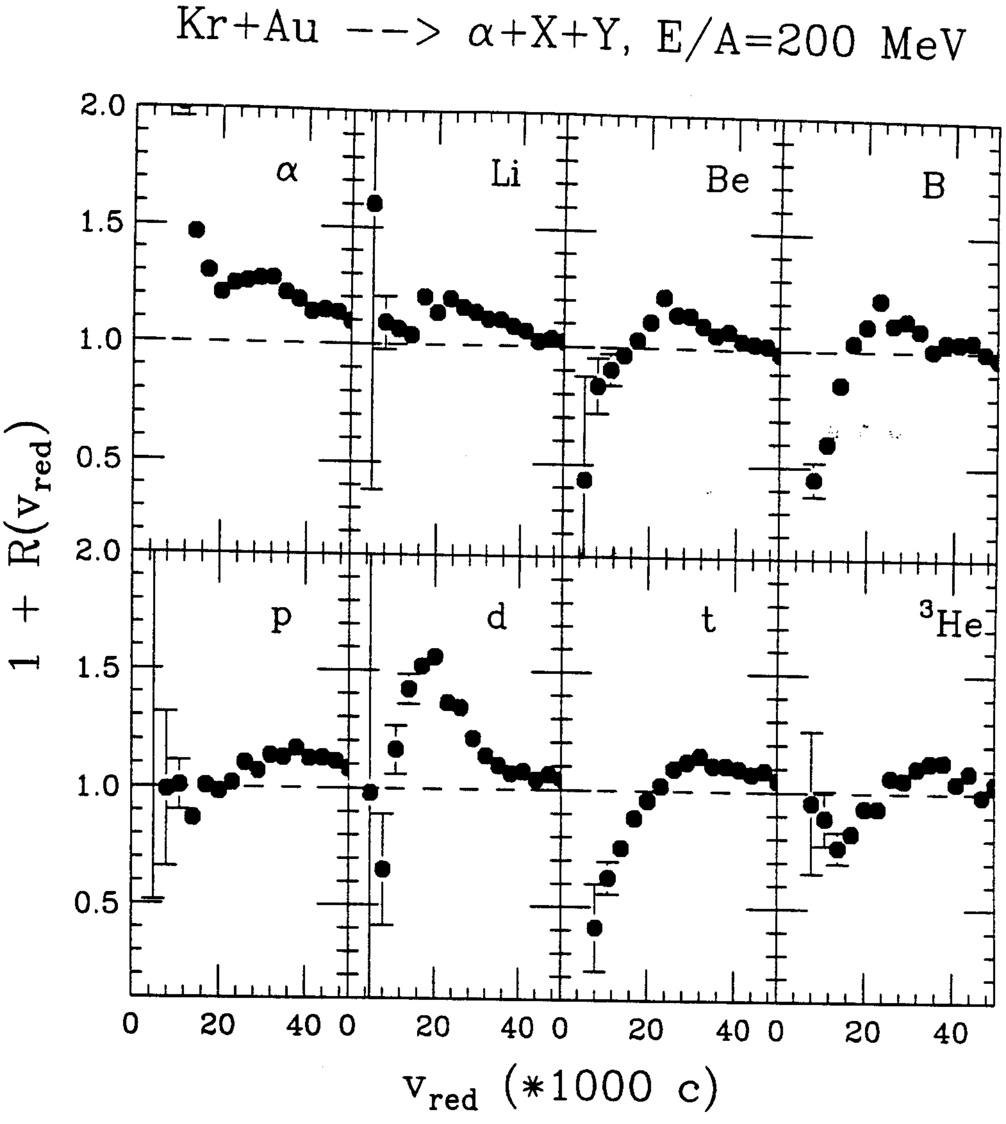

Figure 5.4: The reduced-velocity correlation functions of $\alpha + X$ for ^{84}Kr + ^{197}Au collisions at E/A = 200 MeV and $1 \leq \text{b} \leq 3$. X = p, d, t, ^{3}He, α, Li, Be, and B. v_{red} is defined as $v_{red} = v_{rel}/\sqrt{Z_1 + Z_2}$.

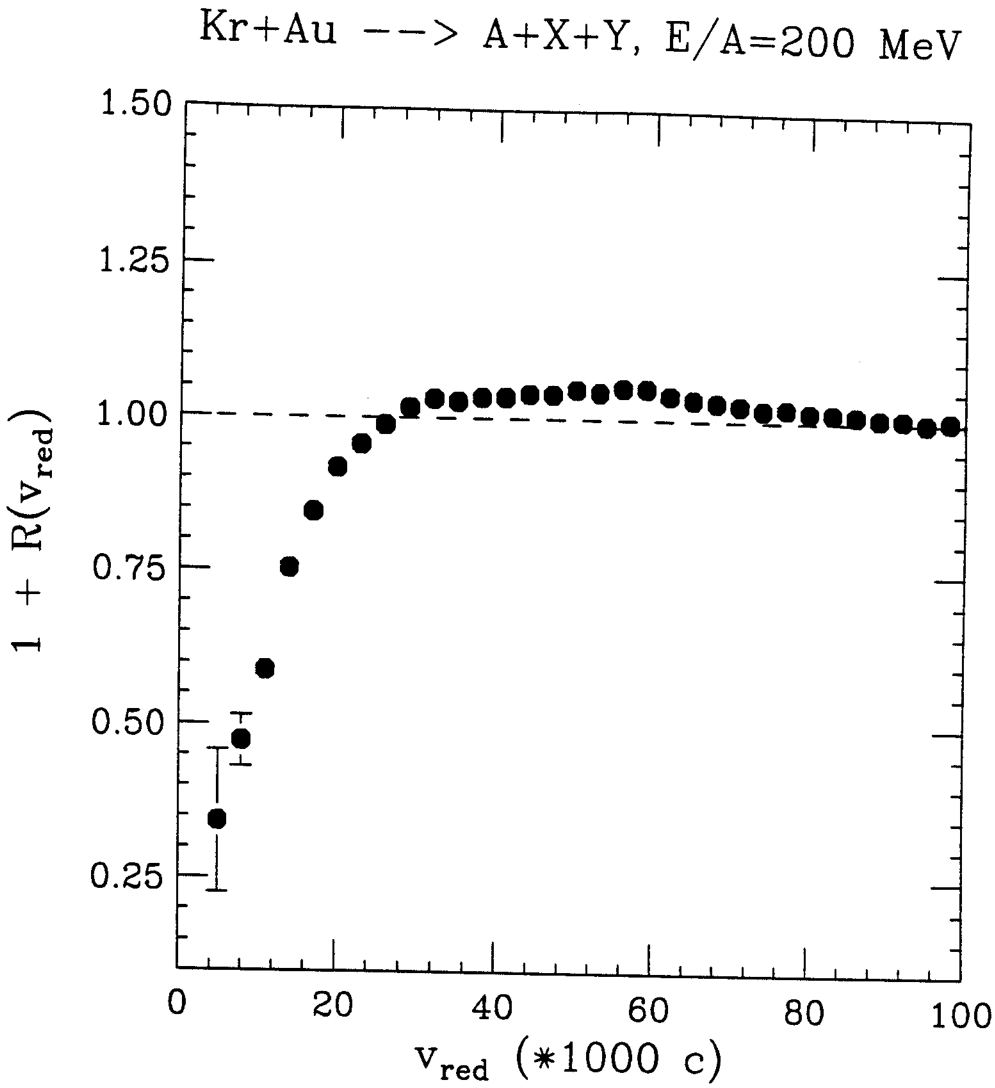

Figure 5.5: The reduced-velocity correlation function of $A + X$ for ^{84}Kr + ^{197}Au collisions at E/A = 200 MeV and $1 \leq b \leq 3$. A, X = d, t, ^{3}He, Li, Be, and B. v_{red} is defined as $v_{red} = v_{rel}/\sqrt{Z_1 + Z_2}$.

and X include d, t, ^{3}He, Li, Be, and B. To correct for the final state interactions from the reduced-velocity correlation functions, $p_{\nu}^{\perp}(y_{\nu}) \cdot p_{\mu}^{\perp}(y_{\mu})$ is weighted with the correlation function $1 + R(v_{red})$ so that the final state interaction can be canceled out.

To extract $\langle p_{\nu}^{x}(y_{\nu})\rangle$ from Eq. (5.9), two-fragment invariant distributions are constructed for each pairs of particle types within the limits of experimental statistics as a function of normalized center of mass rapidity $y_n = y_{cm}/y_{beam}$. Eq. (5.9) is then initially solved for $\langle p_{\nu}^{x}(y_{\nu})\rangle$ by matrix diagonalization for different rapidity bins [Dani 88]. Final values for $\langle p_{\nu}^{x}(y_{\nu})\rangle$ are obtained by a least squares minimization procedure in which the $\langle p_{\nu}^{x}(y_{\nu})\rangle$ on the r.h.s. of Eq. (5.9)are varied from these initial values so as to accurately reproduce the l.h.s. of Eq. (5.9). This procedure permitted an assessment of the uncertainty in the values for $\langle p_{\nu}^{x}(y_{\nu})\rangle$.

5.4 Mass dependence of directed collective flow at 200 MeV/A ^{84}Kr + ^{179}Au collisions.

Using the procedure of the previous section, values for the directed transverse flow were obtained for ^{84}Kr + ^{179}Au collisions at E/A = 200 MeV. In this analysis, two impact parameter gates were applied: $1 \leq \text{b} \leq 3$ fm and $4 \leq \text{b} \leq 6$ fm.

To address the detector acceptance issue, we simulated the velocity distributions of the fragments with a thermal expression of the form

$$P(\mathbf{v}) = \int d^3v_{coll} d^3v_{th} \mathcal{F}(\mathbf{v}_{coll}) \mathcal{G}(\mathbf{v}_{th}) \delta(\mathbf{v} - \mathbf{v}_{coll} - \mathbf{v}_{th}) \tag{5.13}$$

Here, we assume a Gaussian form $\mathcal{F}(\mathbf{v}_{coll}) \propto \exp(-\sum_i \left[\mathbf{v}_{coll}^{i}\right]^2/2\sigma_i^2)$ of collective velocity distribution with three independent principal axes to approximate the situation before breakup. σ_i are chosen so they can fit the transverse momentum distribution in the experiment. We further assume that the momenta of the produced particles obtain additional random velocity components according to the distribution $\mathcal{G}(\mathbf{v}_{th}) \propto \exp(-A\mathbf{v}_{th}^2/2T)$, where A is the fragment mass number and T is a temperature parameter.

The principal axes of the collective velocity distribution are rotated by the flow angle θ_F; σ_3 characterizes the distribution along the flow axis and σ_1 and σ_2 characterizes the other widths in and perpendicular to the reaction plane, respectively. These values for σ_i and T were adjusted to reproduce the measured rapidity and transverse energy distributions. Fig 5.6 shows the momentum distribution of α particles for two rapidity gates $\mathrm{y} = 0$ and $\mathrm{y} = 0.12$ at $1 \leq \mathrm{b} \leq 3$ fm. The solid lines are experimental values and the dashed lines are the simulations of Eq. (5.13) using $\sigma_1 = \sigma_2 = 0.1c$ and $\sigma_3 = 0.15c$. The momentum distributions of these two rapidity gates from the experiment are roughly the same as the simulated momentum distributions.

Simulated flow values using Eq. (5.13) with the values of $\sigma_1 = \sigma_2 = 0.1c, \sigma_3 = 0.16c, \theta_F = 55°$, $T = 45$ MeV are shown in Fig. 5.7 for Beryllium fragments. The open circles are the flow values before being filtered through the experimental device and the filled circles are the flow values after being filtered through the experimental device. One can see in the rapidity range of $-0.2 \leq y_n \equiv y/y_{beam} \leq 0.2$, the acceptance of the Miniball array modifies the mean transverse momenta very little. The mean transverse momentum $\langle P_x/A \rangle$ in this rapidity range is hence used to extract the directed transverse flow.

Experimental data for the mean transverse momenta P_x vs. rapidity y_n at $1 \leq \mathrm{b}$

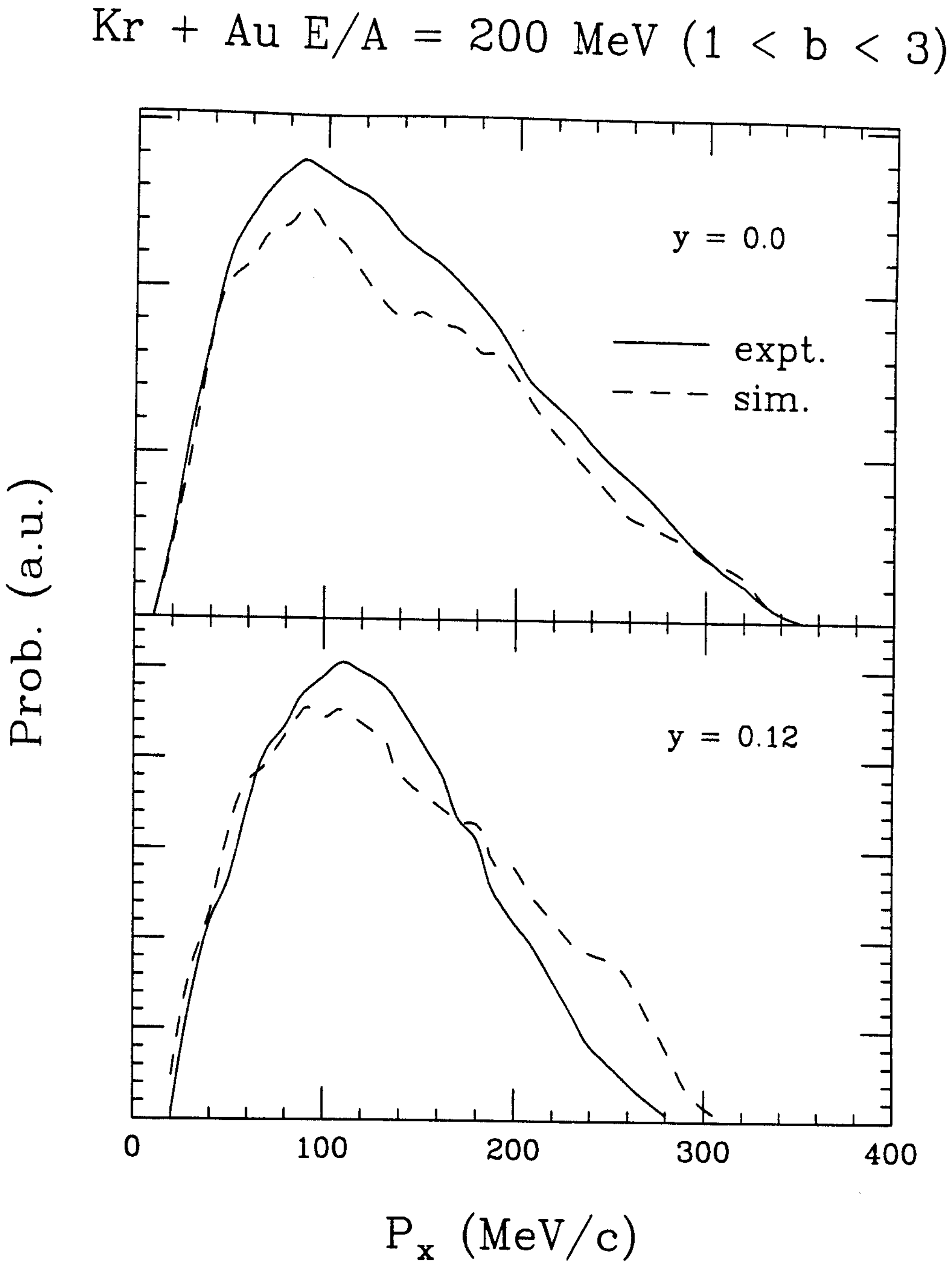

Figure 5.6: The momentum distribution of α particles for two rapidity gates y = 0 and y = 0.12 at $1 \leq b \leq 3$ fm. The solid lines are experimental values and the dashed lines are the simulation of Eq. (5.13) using $\sigma_1 = \sigma_2 = 0.1$ and $\sigma_3 = 0.15$. The momentum distributions of these two rapidity gates from the experiment are roughly the same as the simulated momentum distributions.

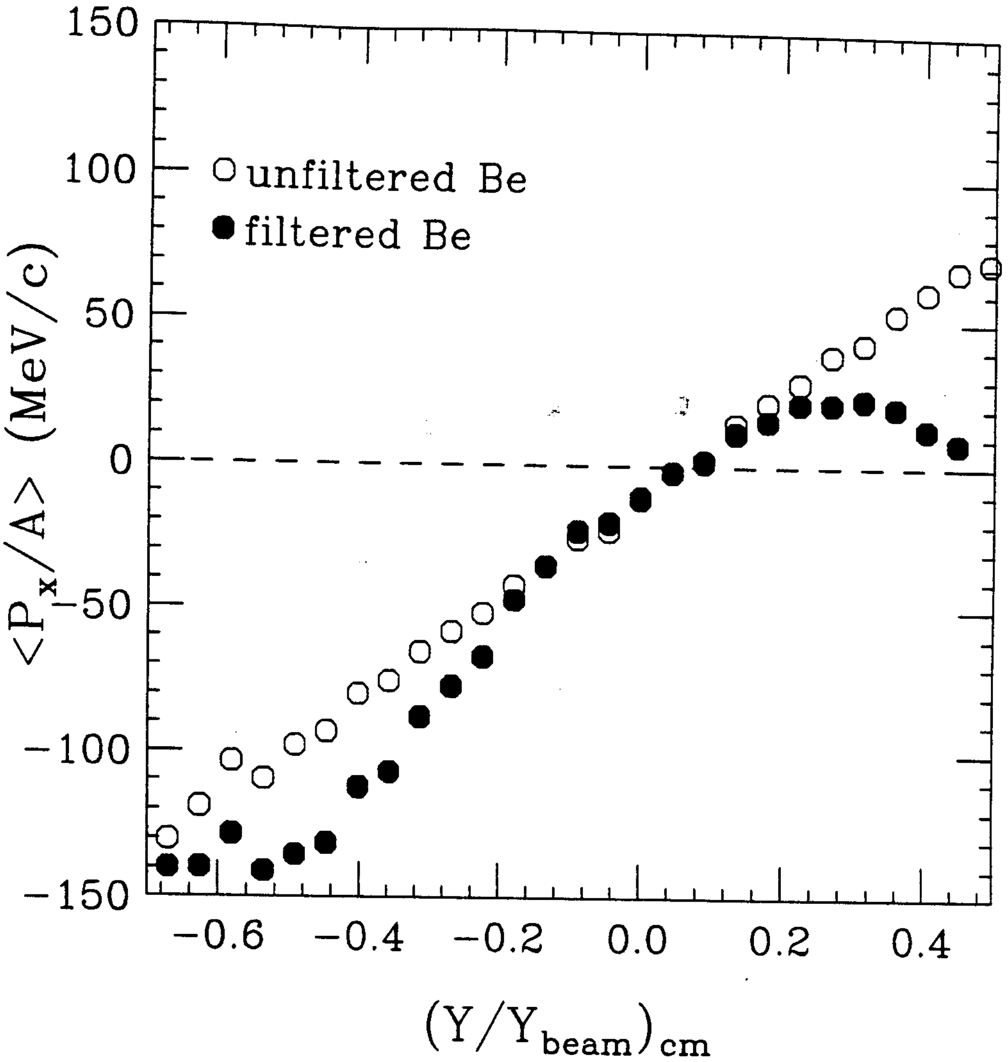

Figure 5.7: Simulations for the transverse momenta of Beryllium fragments within the thermal model of Eq. (5.13). Open and filled circles depict calculations with the model before and after corrections for the experimental acceptance have been applied.

≤ 3 fm and $4 \leq \text{b} \leq 6$ fm are shown in Fig. 5.8 and Fig. 5.9 for proton, α, Li, Be, B, and C particles. Near $y_n = 0$, the data in Fig. 5.8 and Fig. 5.9 are well characterized by the collective flow, $F = d\langle p_x/A\rangle/dy_n$, which can be easily extracted via a linear least-squares fit at $-0.2 \leq y_n \leq 0.2$. The slope is bigger for heavier fragments, and hence the larger flow.

The flow per nucleon, $d\langle p_x/A\rangle/dy_n$, is shown as a function of fragment mass in Fig. 5.10 for the two impact parameter gates. As expected, the flow per nucleon is larger for the more peripheral gate. A linear dependence of the flow upon mass is observed for $\text{Z} \leq 2$, in agreement with previous measurements of the flow of light charged particles [Doss 87, Part 95, Wang 95]. For fragments with Z>2, however, the flow is approximately independent of mass. The overall trend is consistent with the fragment observables becoming increasingly dominated by collective motion in the fragmenting system, which makes contributions to the fragment velocities which are independent of the fragment mass unlike thermal velocities which decrease inversely with the square root of the fragment mass.

To examine the interplay between collective and thermal motion more quantitatively, Eq. (5.13) is used to simulate the experimental data. The solid (dashed) line in Fig. 5.10, for calculations assuming $\sigma_1 = \sigma_2 = 0.1c, \sigma_3 = 0.15c, \theta_F = 55°$, $T = 55$ MeV ($\sigma_1 = \sigma_2 = 0.1c, \sigma_3 = 0.16c, \theta_F = 55°$, $T = 45$ MeV), reproduces everything but the α particle data, for which small relative momentum correlations revealed strong contaminations from secondary decays of heavier fragments with large flow values. To illustrate the flow values given by the collective velocity distributions for $4 \leq b \leq 6$, the simulation with $T = 0$ MeV is shown by the dotted line in Fig. 5.10. One can see that the flow values for the heavy fragments approach the limit with $T = 45$ MeV. While this parameterization is not unique,

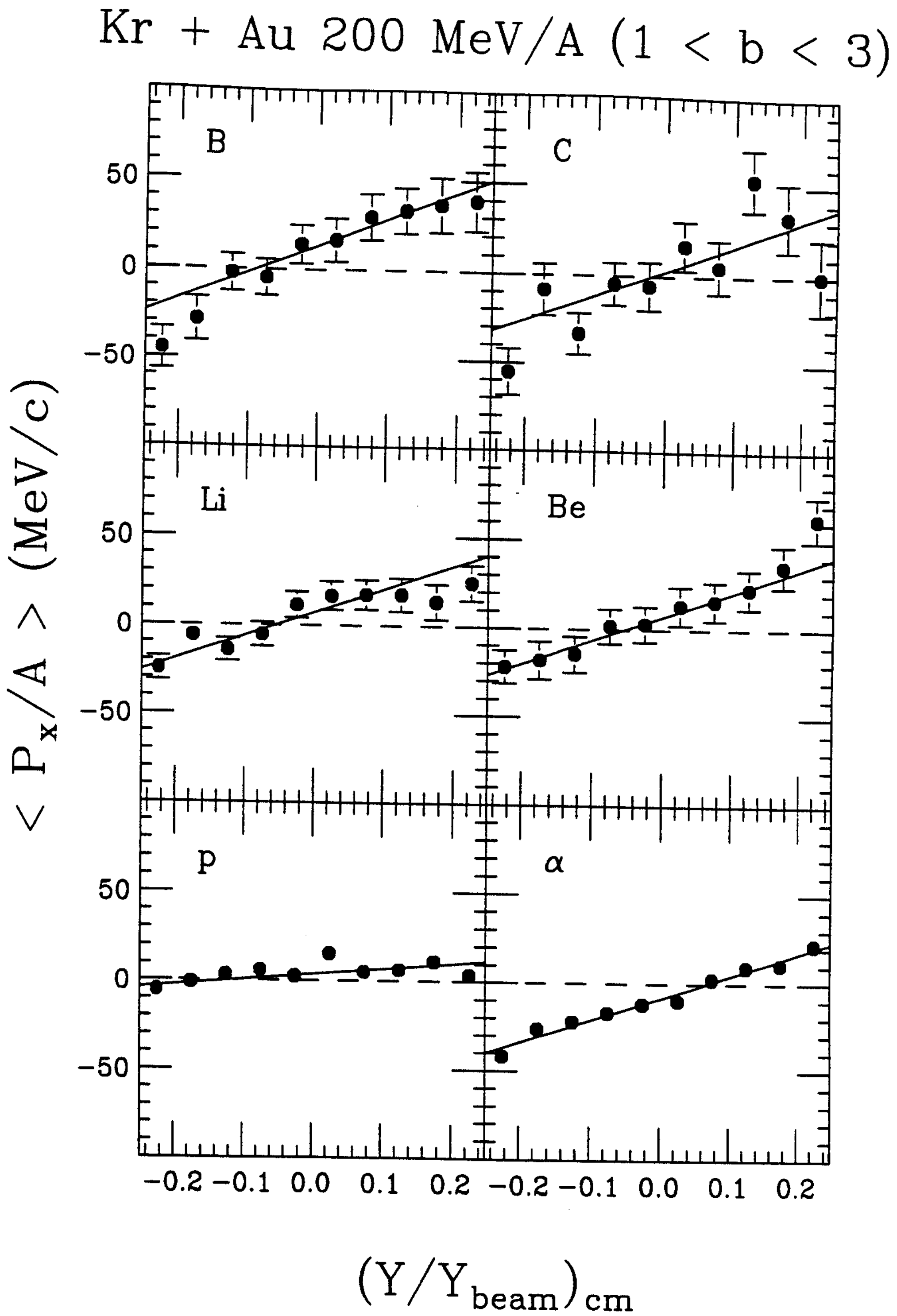

Figure 5.8: Mean P_x vs. rapidity y for 200 AMeV Kr + Au at $1 \leq \mathrm{b} \leq 3$ fm with proton, α, Li, Be, B, and C particles. The straight lines are a linear fit to the data from -0.2 to 0.2 of y.

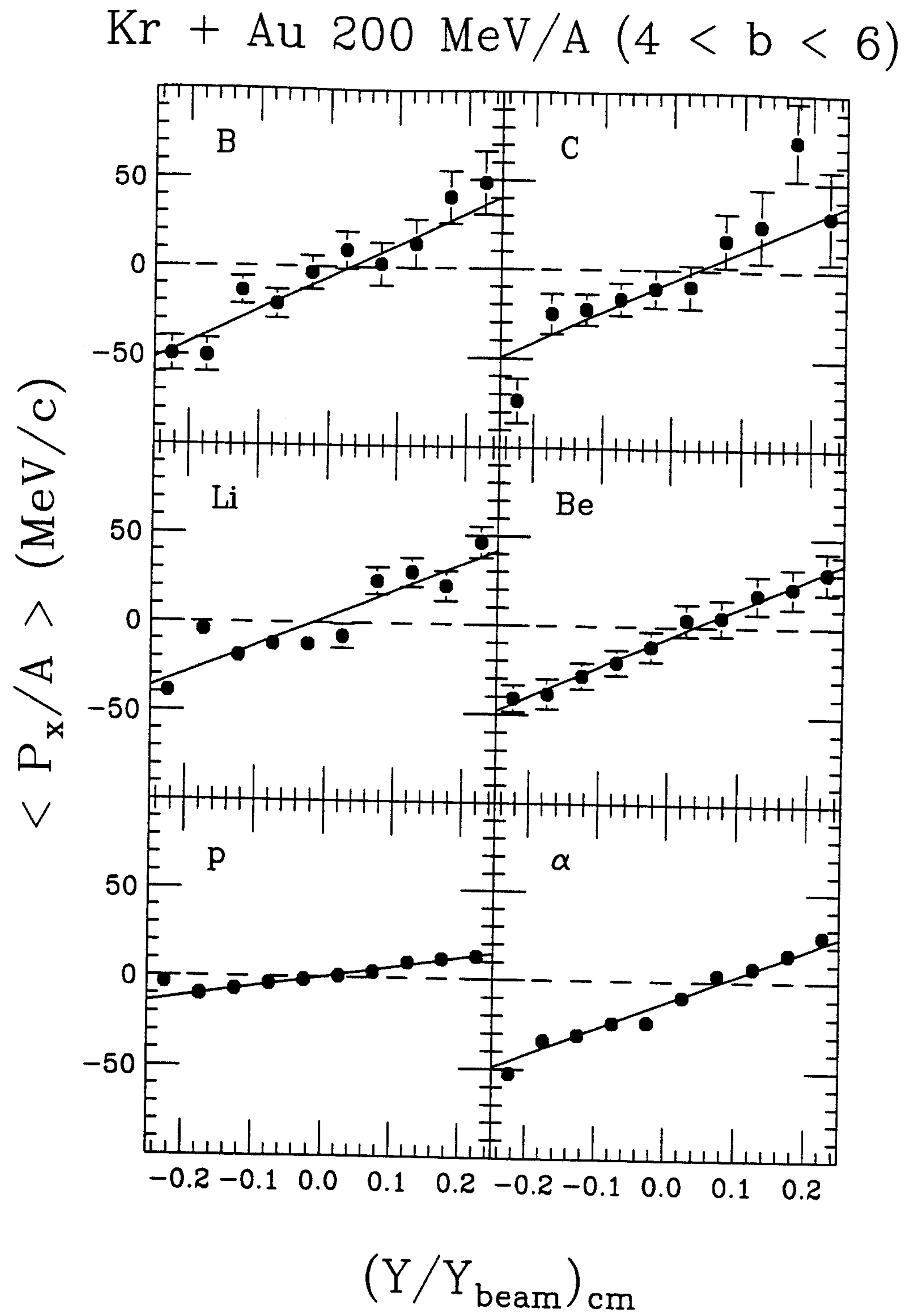

Figure 5.9: Mean P_x vs. rapidity y for 200 AMeV Kr + Au at $4 \leq b \leq 6$ fm with proton, α, Li, Be, B, and C particles. The straight lines are a linear fit to the data from -0.2 to 0.2 of y.

the model indicates that the near constancy of the heavy fragment flow occurs because it is primarily governed by the collective velocity distribution. The flow for light particles is then reduced relative to that for heavy fragments due to a mass dependent thermal mixing between the collective velocity distributions at positive and negative rapidities in the c.m. system.

In the limit of local thermal equilibrium, coalescence and thermodynamic models make very similar predictions for the particle mass dependence of momentum distributions [Cser 86]. The level of agreement shown in Fig. 5.10 therefore implies consistency with coalescence-like cluster production mechanisms [Dani 91] and provides a justification for coalescence-invariant analyses. Accordingly we constructed a coalescence-invariant effective proton flow

$$F_{eff} = \sum Z_i Y_i F_i / \sum Z_i Y_i \tag{5.14}$$

where the Z_i, Y_i, and F_i are the charge, yield, and flow values for the various particle species, to enable comparisons to the proton flow predicted by transport models such as the Boltzmann-Uehling-Uhlenbeck (BUU) equation and render comparisons to molecular dynamics models which do not accurately describe the fragment observables [Peas 94] unnecessary.

If one constructs the effective proton flow using the measured flow and yield data for Z$\leq$ 6 one obtains 51 ± 11 and 89 ± 10 MeV/c for 1 < b < 3 and 4 < b < 6, respectively. Using the measured charge yields and Eq. (5.14) to extrapolate from $Z \leq 6$ to $Z \leq 12$ raises the corresponding flow values to 54 ± 11 and 92 ± 10 MeV/c, respectively. These two extrapolated experimental effective proton flow values plus a similarly constructed

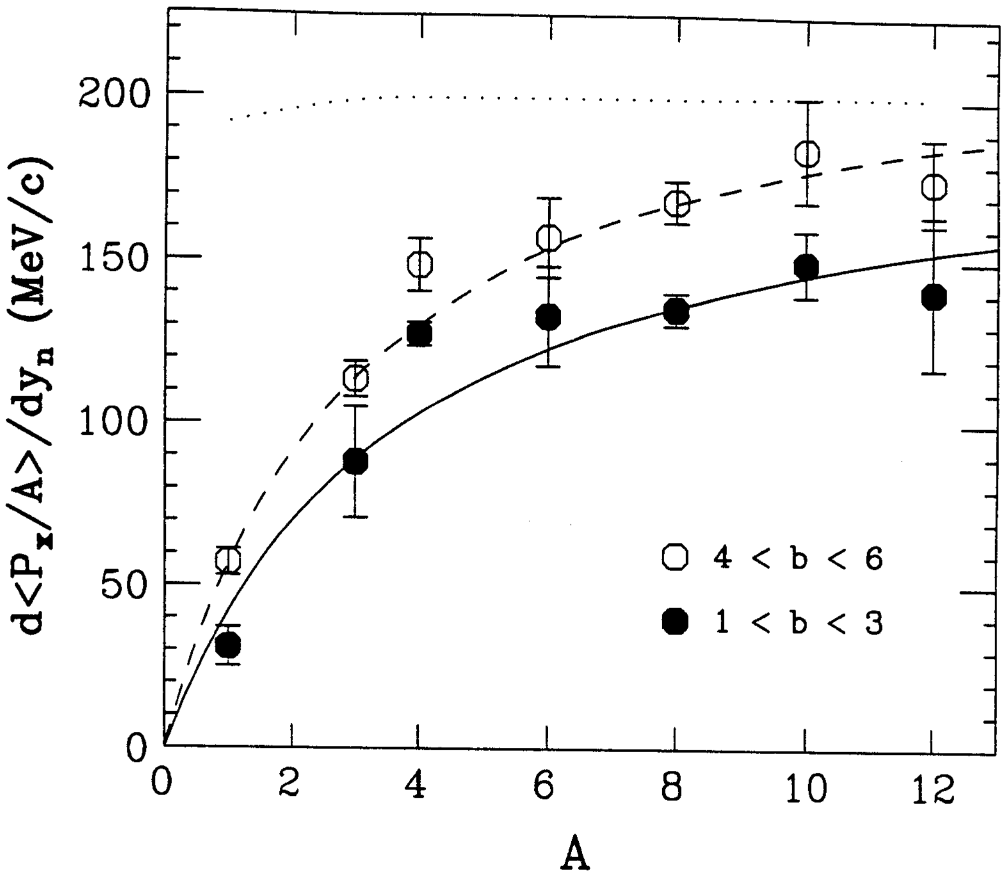

Figure 5.10: The mass dependence of the collective sidewards flow per nucleon in the reaction plane, $d\langle p_x/A\rangle/dy_n$ for the two impact parameter gates used in the analysis. The lines are the calculations from the thermal model described in the text.

overlapping intermediate value for 2.5 < b < 4.5 are plotted in Fig. (5.11) as the cross-hatched rectangles with horizontal widths that represent the relevant impact parameter bins and vertical widths (uncertainties) that primarily reflect an estimated ($< 1fm$) uncertainty in the determination of the average impact parameter. Note that the effective proton flow exceeds the measured proton flow, as expected for the coalescence model which creates clusters and depletes free proton flux in densely occupied regions in phase space, where collective phenomena are most strongly manifested.

To test the sensitivity of this measurement to the transport parameters, BUU calculations have been performed for various parameterizations of the mean field potential and including a nucleon-nucleon cross section which has been parameterized to describe measured nucleon-nucleon scattering data [Klak 93]. The BUU equation is described in Eq. (4.7). In Eq. (4.7), U is the mean field potential and is usually approximated by a Skyrme-like parameterization:

$$U(\rho) = A(\rho/\rho_0) + B(\rho/\rho_0)^\sigma \tag{5.15}$$

where ρ is the nucleon number density, ρ_0 is the saturation density and A, B, and σ are constants which can be determined by the ground state binding energy [Bert 88]. In stiff EOS, A = -124 MeV, B = 70 MeV, and σ = 2; this corresponds to the compressibility $K \approx$ 380 MeV. In soft EOS, A = -356 MeV, B = 303 MeV, and σ = 1.17; this corresponds to the compressibility $K \approx$ 200 MeV.

In Eq. (5.15), the nuclear potential is assumed to depend only on the nuclear density, ignoring any momentum dependence of the mean field. However, a more realistic parameterization should account for the fact that the one-body potential must also be a

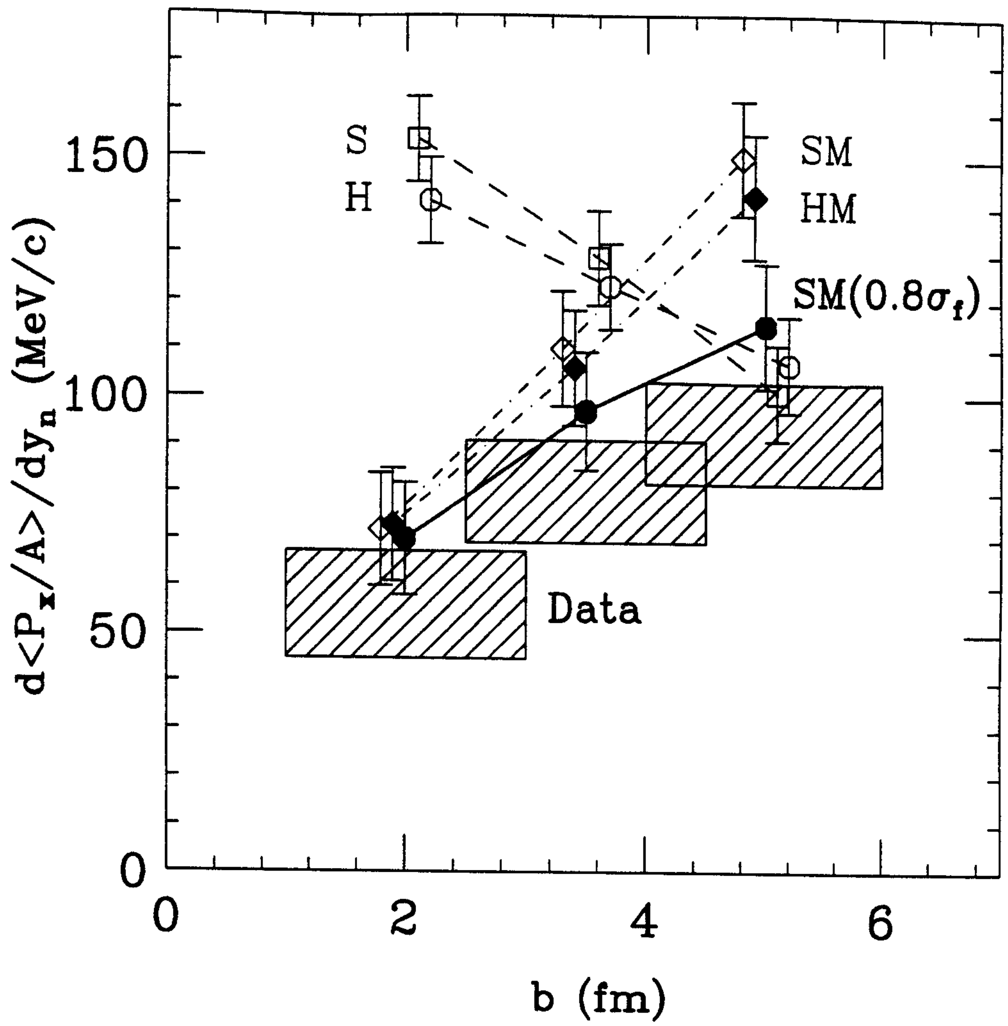

Figure 5.11: The cross-hatched rectangles depict the measured effective proton flow. Also shown are the corresponding BUU calculations for the following parameter sets: **H** - hard EOS without momentum dependence (open circles), **S** - soft EOS without momentum dependence (open squares), **HM** - hard EOS with momentum dependence (solid diamonds), **SM** - soft EOS with momentum dependence (open diamonds). **SM** **(0.8σ_{free})** - soft EOS with momentum dependence and a 20% reduction in the nucleon-nucleon cross-section (solid circles). The theoretical error bars are purely statistical.

function of the momentum p of a nucleon with respect to the nuclear medium. Evidence for this momentum dependence comes from the experimental behavior of the real part of the mean field (optical) potential [Gale 90]. Calculations were performed with a momentum dependent mean field potential of the form

$$U(\rho, \mathbf{p}) = A(\rho/\rho_0) + B(\rho/\rho_0)^\sigma + 2\frac{C}{\rho_0}\int d^3p' \frac{f(\mathbf{r}, \mathbf{p}')}{1 + [\frac{\mathbf{p}-\mathbf{p}'}{\Lambda}]^2} \tag{5.16}$$

where $f(\mathbf{r}, \mathbf{p})$ is the nucleon phase-space density and is related to the configuration space density $\rho(\mathbf{r})$ by $\rho(\mathbf{r}) = \int f(\mathbf{r}, \mathbf{p}) d^3p$. The parameters for hard EOS with momentum dependent force were chosen to be: A = -5.9 MeV, B = 36 MeV, σ = 2.45, C = -65 MeV, and Λ = 0.416. The parameters for soft EOS with momentum dependent force were chosen to be: A = -110 MeV, B = 141 MeV, σ = 1.24, C = -65 MeV, and Λ = 0.416.

Momentum dependent forces have been shown to have a large effect on the dynamics and on the observables of high-energy heavy-ion collisions [Cuss 85, Gale 87, Aich 87, Gale 90]. In general, the overall mean field interaction will be more repulsive under the condition of the heavy ion collision if a momentum dependence like that in Eq. (5.16) is included in the BUU equation. Thus the effect of a stiff equation of state may occur with a soft equation of state [Gale 87].

These BUU calculations with different potentials are shown in Fig. 5.11 for a soft (K=200 MeV) mean field (**SM** - open diamonds) and a hard (K=386 MeV) mean field (**HM** - solid diamonds) with a momentum dependence consistent with energy dependence of optical potential determined via nucleon-nucleus potential scattering [Gale 90]. Calculations with a soft mean field (**S** - open squares) and a hard mean field (**H** - open circles) without momentum dependence are also shown. All calculations have been impact parameter averaged and filtered by the experimental acceptance.

Calculations indicate that mean field repulsion (nucleon-nucleon collisions) governs the flow for the momentum dependent (independent) simulations [Zhan 94]. These differences cause alterations to the time dependent non-equilibrium transport that provide the differences in impact parameter dependences shown in Fig. 5.11. The trends of the momentum dependent calculations are in better agreement with experimental data, consistent with investigations at higher incident energies [Aich 87, Gale 87, Pan 93]. The sensitivity to the compressibility parameter K is slight, however. Improved agreement between the momentum dependent calculations and the data can be obtained by a 20% density dependent reduction of the in-medium nucleon-nucleon cross section of the form $\sigma_{NN} = (1-0.2\frac{\rho}{\rho_o})\sigma_{free}$ [West 93], consistent with the systematics of the disappearance of collective flow [West 93] and with microscopic calculations of the in-medium corrections to the nucleon-nucleon cross section [Alm 95]. This is illustrated by the solid circles in the Fig. 5.11 for a soft momentum dependent mean field (**SM**$(0.8\sigma_{free})$). The calculations with reduced cross section are somewhat higher than the data. These discrepancies can only be reduced by a few percent by including the presently uncounted contributions to the effective proton flow from fragments with Z>12.

Thus, in summary, we have measured the mass dependence of directed transverse flow for the system ^{84}Kr+^{197}Au at an incident energy of 200 MeV/A. The flow has a linear mass dependence for light fragments, but is nearly independent of mass for intermediate mass fragments with $Z > 2$. With the exception of α particles, the mass dependence is reproduced by model calculations which superimpose a thermal velocity distribution upon a collective velocity distribution. These calculation suggests that the flow of heavy fragments is governed mainly by the collective velocity distribution. Comparisons to BUU calculations demonstrate a definite preference for a momentum dependent mean field and offer support for a 20% density dependent reduction in the nucleon-nucleon cross-section from the value in free space.

Chapter 6

Summary and Conclusions

The investigation of the nuclear equation of state at elevated temperature and density significantly greater than or less than saturation density is one of the principle objectives of nuclear physics. Experimental information relevant to these issues is principally obtained by colliding complex nuclei. Most of this experimental dissertation is focused upon obtaining information about the equation of state and the liquid gas phase transition of low density nuclear matter. To study these problems, two reactions were studied:

1. Measurements of central ^{197}Au + ^{197}Au collisions at E/A = 35 MeV

This Au + Au system has many attributes that make it a good candidate for probing the nuclear liquid-gas phase transition. Previous experiments by our Miniball/Multics collaboration revealed that this system decays via a slow multifragment disintegration. Most of the experimental observations were remarkably well produced by Statistical Multifragmentation Model (SMM) calculations at a temperature of $T \approx 6MeV$ and a density of

$\rho_0/6 \leq \rho \leq \rho_0/3$ which assumed that the fragments were produced in a "cracking" phase transition.

The focus of the experiments was on testing the thermal assumptions of the SMM calculations by a direct measurement of the breakup temperature. The temperatures of ^{197}Au + ^{197}Au central collisions at E/A = 35 MeV were measured in this dissertation by measuring the ratios of the populations of pairs of particle unstable states of ^{5}Li, ^{4}He, and ^{10}B multifragmentation products, and measuring various double isotope ratios of multifragmentation products with very different binding energies. These ratios were then compared to sequential decay calculations and the emission temperatures which describe the freezeout configurations were extracted. The emission temperatures measured from both excited state populations and isotope ratios are consistent, suggesting that local equilibrium is reached in this incident energy.

The data was then extrapolated to zero impact parameter to extrapolate an emission temperature of T $\approx$ 4.6 MeV at b = 0 which is about 1.5 MeV lower than the value required by SMM calculations which reproduce the other experimental observables. The 1.5 MeV discrepancy indicates that the SMM calculations either has some deficiencies in its thermodynamical assumptions or there are additional cooling mechanisms which have been neglected in this comparison. Future experiments and improved theoretical calculations are needed to address this discrepancy.

2. Measurement of central ^{129}Xe + ^{nat}Cu collisions at E/A = 30 MeV

By studying the temperatures of residues formed in nucleus-nucleus collisions at incident energies of about E/A = 30-60 MeV, information about the incompressibility of the nuclear equation of state (EOS) at $\rho < \rho_0$ can be extracted. Previous measurements indicated that hot residues are formed in central ^{129}Xe + ^{nat}Cu collisions at E/A = 30 MeV, making this reaction suitable for this type of investigation of the low density nuclear EOS.

Similar to the measurement of central ^{197}Au + ^{197}Au collisions at E/A = 35 MeV, the emission temperatures for central ^{129}Xe + ^{nat}Cu collisions at E/A = 30 MeV were determined by measuring both excited state populations and double isotope ratios. As for Au + Au collisions at E/A = 35 MeV, consistent results were obtained via these two techniques. The emission temperatures for this experiment were compared to Boltzmann-Uehling-Uhlenbeck (BUU) calculations with the stiff EOS (K = 380 MeV) and the soft EOS (K = 200 MeV). The experimental data are closer to the soft equation of state. However, since cooling dynamics plays an important role in reducing the emission temperature for this reaction, this comparison is not conclusive as yet. Further information about the cooling effect is needed before a rigorous comparison between theory and experiment can be provided.

One experiment was conducted to investigate the resolution of ambiguities about the equation of state at high nuclear density.

3.Measurement of ^{84}Kr + ^{197}Au collisions at E/A = 200 MeV

Investigations of the compressibility of the nuclear EOS at high density have been conducted by measuring the directed transverse flow in central collisions between equal mass projectile and target nuclear in experiments at the Bevalac, GSI, AGS and CERN. Analyses of Bevalac and GSI data for equal mass projectile and target nuclei are unable to decouple uncertainties about the density dependence of the EOS at high density from the momentum dependence of the nuclear mean field. Analyses of mass asymmetric Ar + Pb data at SATURNE indicated that a comparison between data for equal projectile and target nuclei to data for mass asymmetric systems at the same incident energy per nucleon can break this ambiguity and allow a clean determination of the nuclear EOS at high density. In this dissertation, the mass asymmetric Kr + Au system was explored to determine whether these conclusions about the utility of data from mass asymmetric systems were correct.

The analyses of transverse flow in ^{84}Kr + ^{197}Au collisions at $E/A = 200$ MeV used a technique which is free of reaction plane dispersion. The directed transverse flow per nucleon in this reaction was observed to increase with mass, following a thermal- or coalescence-like behavior, and attained roughly constant limiting values at $4 \leq A \leq 12$. Comparisons of the impact parameter dependences of the measured coalescence-invariant proton flow to BUU calculations clearly favor a momentum dependent nuclear mean field. This confirmed the importance of measuring the transverse flow for unequal mass projectile and target nuclei and supported the previous conclusions about momentum dependence of the nuclear mean field. When combined with the analyses of collisions of equal mass projectile and target nuclei, it appears that the best agreement is obtained for a soft EOS. It will be interesting to see whether these conclusions remain valid as future data becomes available.

Bibliography

[Aich 84] J. Aichelin and J. Hüfner, Phys. Lett. **B136** (1984) 15.

[Aich 85] J. Aichelin and G. Bertsch, Phys. Rev. **C331** (1985) 1730.

[Aich 86] J. Aichelin and H. Stöcker, Phys. Lett. **B176** (1986) 14.

[Aich 87] J. Aichelin *et al.*, Phys. Rev. Lett. **58** (1987) 1926.

[Ajze 88] F. Ajzenberg-Selove, Nucl. Phys. **A490** (1988) 1; Nucl. Phys. **A475** (1987) 1; **A413** (1984) 1; **A433** (1985) 1; **A449** (1986) 1; **A460** (1986) 1.

[Albe 85] S. Albergo, S. Costa, E. Costanzo, and A. Bubbino, Nuovo Cimento **89** (1985) 1.

[Alm 95] T. Alm, Nucl. Phys. **A587** (1995) 815.

[Amsd 75] A.A. Amsden, G.F. Bertsch, F.H. Harlow, and J.R. Nix, Phys. Rev. Lett. **35** (1975) 905.

[Bade 82] A. Baden *et al.*, Nucl. Instrum. Methods **203** (1982) 189.

[Bald 88] A. Baldini *et al.*, Total Cross Sections for Reactions of High Energy Particles, Landolr-Börnstein, New Series Vol. I/12, ed. H. Schopper (1988).

[Baue 92] W. Bauer, G.F. Bertsch, and H. Schulz, Phys. Rev. Lett. **69** (1992) 1888.

[Baum 75] H.G. Baumgardt *et al.*, Z. Phys. **A273** (1975) 359.

[Beau 83] D. Beauvis *et al.*, Phys. Rev. **C27** (1983) 2443.

[Bert 84] G.F. Bertsch, H. Kruse, and S. Das Gupta, Phys. Rev. **C29** (1984) 673.

[Bert 87] G.F. Bertsch, W.G. Lynch, and M.B. Tsang, Phys. Lett. **B189** (1987) 384.

[Bert 88] G.F. Bertsch and S.Das Gupta, Phys. Rep. **160** (1988) 189, and ref. wherein.

[Beth 37] H.A. Bethe, Rev. Mod. Phys. **9** (1937) 69.

[Birk 83] J.R. Birkelund and J.R. Huizenga, Annu. Rev. Nucl. Sci. **33** (1983) 265.

[Blai 76] J.P. Blaizot *et al.*, Nucl. Phys. **A265** (1976) 315.

[Blai 80] J.P. Blaizot, Phys. Rep. **64** (1980) 171.

[Bloc 87] C. Bloch *et al.*, Phys. Rev. **C36** (1987) 203.

[Bloc 88] C. Bloch *et al.*, Phys. Rev. **C37** (1988) 2469.

[Boal 84] D.H. Boal, Phys. Rev. **C30** (1984) 749.

[Boal 86] D.H. Boal and A.L. Goodman, Phys. Rev. **C33** (1986) 1690.

[Boal 89] D.H. Boal *et al.*, Phys. Rev. **C40** (1989) 601.

[Boal 89a] D.H. Boal *et al.*, Phys. Rev. Lett. **62** (1989) 737.

[Bonc 84] P. Bonche, S. Levit, and D. Vautherin, Nucl. Phys. **A428** (1984) 95c.

[Bond 85] J.P. Bondorf *et al.*, Nucl. Phys. **A443** (1985) 321.

[Bond 86] J.P. Bondorf *et al.*, Nucl. Phys. **A444** (1986) 460.

[Bond 94] J.P. Bondorf *et al.*, Phys. Rev. Lett. **73** (1994) 268.

[Bond 95] J.P. Bondorf *et al.*, Physics Reports 257 (1995) 133.

[Bohr 36] N. Bohr, Nature **137** (1936) 344.

[Bowm 91] D.R. Bowman *et al.*, Phys. Rev. Lett. **67** (1991) 1527.

[Bowm 92] D.R. Bowman *et al.*, Phys. Rev. **C46** (1992) 1834.

[Bowm 95] D.R. Bowman *et al.*, Phys. Rev. **C52** (1995) 818.

[Botv 87] A.S. Botvina *et al.*, Nucl. Phys. **A475** (1987) 663.

[Botv 95] A.S. Botvina *et al.*, Nucl. Phys. **A584** (1987) 663.

[Brow 85] G.E. Brown and E. Osens, Phys. Lett. **B159** (1985) 223.

[Brow 88] B.A. Brown, Private Communication.

[Brun 91] M. Bruno *et al.*, Nucl. Instrum. Methods **A305** (1991) 410.

[Brun 92] M. Bruno *et al.*, Nucl. Instrum. Methods **A311** (1992) 189.

[Buch 84] G. Buchwald *et al.*, Phys. Rev. Lett. **52** (1984) 1594.

[Cava 90] C. Cavata *et al.*, Phys. Rev. **C42** (1990) 1760.

[Chen 87] Z. Chen *et al.*, Phys. Rev. **C36** (1987) 2297.

[Chen 87a] Z. Chen *et al.*, Nucl. Phys. **A473** (1987) 564.

[Chen 87b] Z. Chen *et al.*, Phys. Lett. **B199** (1987) 171.

[Chen 88] Z. Chen and C.K. Celbke, Phys. Rev. **C38** (1988) 2630.

[Chit 86] C.B. Chitwood *et al.*, Phys. Lett. **B172** (1986) 27.

[Chit 86a] C.B. Chitwood *et al.*, Phys. Rev. **C34** (1986) 858.

[Colo 93] N. Colonna and E. Lisi, Nucl. Instrum. Methods **A334** (1993) 551.

[Corn 95] E. Cornell *et al.*, Phys. Rev. Lett. **75** (1995) 1475.

[Cser 86] L.P. Csernai and J.I. Kapusta, Phys. Rep. **131** (1986) 223.

[Cugn 80] J. Cugnon, Phys. Rev. **C22** (1980) 1885.

[Curt 83] M.W. Curtin *et al.*, Phys. Lett. **B123** (1983) 289.

[Cuss 85] R.Y. Cusson *et al.*, Phys. Rev. Lett. **55** (1985) 2786.

[Dago 95] M. D'Agostino *et al.*, Phys. Rev. Lett. **75** (1995) 4373.

[Dago 96] M. D'Agostino *et al.*, Phys. Lett. B **368** (1996) 259.

[Dago 96a] M. D'Agostino *et al.*, Phys. Lett. B **371** (1996) 175.

[Dani 85] P. Danielewicz and G. Odyniec, Phys. Lett. **157B** (1985) 146.

[Dani 88] P. Danielewicz *et al.*, Phys. Rev. **C38** (1988) 120.

[Dani 91] P. Danielewicz and G.F. Bertsch, Nucl. Phys. **A533** (1991) 712.

[Demo 90] M. Demoulins *et al.*, Phys. Lett. **B241** (1990) 476.

[deSo 90] R.T. deSouza *et al.*, Nucl. Instrum. Methods **A295** (1990) 109.

[deSo 91] R.T. deSouza *et al.*, Phys. Lett. **B268** (1991) 6.

[Dono 87] A. D'Onofrio *et al.*, Z. Phys. **A326** (1987) 335.

[Doss 87] K.G.R. Doss *et al.*, Phys. Rev. Lett. **59** (1987) 2720.

[Endt 78] P.M. Endt and C. Van Der Leun, Nucl. Phys. **A310** (1978) 1.

[Feld 90] G. Feldman *et al.*, Phys. Rev. **C42** (1990) R1167.

[Fiar 73] S. Fiarman and W.E. Meyerhof, Nucl. Phys. **A206** (1973) 1.

[Fiel 84] D.J. Fields *et al.*, Phys. Rev. **C30** (1984) 1912.

[Fiel 86] D.J. Fields *et al.*, Phys. Rev. **C34** (1986) 536.

[Fiel 87] D.J. Fields *et al.*, Phys. Lett. **B187** (1987) 257.

[Finn 82] J.E. Finn *et al.*, Phys. Rev. Lett. **49** (1982) 1321.

[Fish 67] A.S. Fisher, Physics (Long Island City, N.Y.) **3**, (1967) 255.

[Frie 81] B. Friedman and V.R. Pandharipande, Nucl. Phys. **A361** (1981) 592.

[Frie 83] W.A. Friedman and W.G. Lynch, Phys. Rev. **C28** (1983) 950.

[Frie 88] W.A. Friedman, Phys. Rev. Lett. **60** (1988) 2125.

[Frie 89] W.A. Friedman, Phys. Rev. **C40** (1989) 2055.

[Frie 90] W.A. Friedman, Phys. Rev. **C42** (1990) 667.

[Gale 87] C. Gale, G. Bertsch, and S. DasGupta, Phys. Rev. **C35** (1987) 1666.

[Gale 90] C. Gale *et al.*, Phys. Rev. **C41** (1990) 1545.

[Gelb 87] C.K. Gelbke and D.H. Boal, Prog. Part. and Nucl. Phys. **19** (1987) 33.

[Gilb 65] A. Gilbert and A.G.W. Cameron, Can. J. Phys. **43** (1965) 1446.

[Gilk 94] M.L. Gilkes *et al.*, Phys. Rev. Lett. **73** (1994) 590.

[Glen 88] N.K. Glendenning, Phys. Rev. **C37** (1988) 2733.

[Gobb 93] A. Gobbi *et al.*, Nucl. Instrum. Methods **A324** (1993) 156.

[Gome 88] J. Gomez del Campo *et al.*, Phys. Rev. Lett. **61** (1988) 290.

[Gong 91] W.G. Gong, PhD. Thesis, Michigan State University, (1991).

[Good 84] A.L. Goodman, J.I. Kapusta, and A.Z. Mekjian, Phys. Rev. **C30** (1984) 851.

[Gros 86] D.H.E. Gross, Phys. Rev. Lett. **56** (1986) 1544.

[Gros 88] D.H.E. Gross *et al.*, Phys. Lett. **B203** (1988) 26.

[Gros 90] D.H.E. Gross, Rep. Prog. Phys. **53** (1990) 605.

[Gust 84] H.A. Gustafesson *et al.*, Phys. Rev. Lett. **52** (1984) 1590.

[Gust 88] H.A. Gustafesson *et al.*, Phys. Lett. **A3** (1988) 1323.

[Gutb 87] H.H. Gutbrod *et al.*, Phys. Rev. Lett. **59** (1987) 2070.

[Gutb 89] H.H. Gutbrod, A.M. Poskanzer, and H.G. Ritter, Rep. Prog. Phys., **52** (1989) 1267 and ref. therein.

[Hahn 87] D. Hahn and H. H. Stocker, Phys. Rev. **C35** (1987) 1311.

[Haus 52] W. Hauser and H. Feshbash, Phys. Rev. **87** (1952) 366.

[Heid 95] B. Heide and H.W. Barz, Nucl. Phys. **A588** (1995) 918.

[Hils 87] D. Hilscher *et al.*, Phys. Rev. **C36** (1987) 208.

[Hirs 84] A.S. Hirsch *et al.*, Phys. Rev. **C29** (1984) 508.

[Hsi 94] W.C. Hsi *et al.*, Phys. Rev. Lett. **73** (1994) 3367.

[Hsi 95] W.C. Hsi, PhD. Thesis, Michigan State University, (1995).

[Huan 96] M.J. Huang *et al.*, Phys. Rev. Lett. **77** (1996) 3739.

[Huan 97] M.J. Huang *et al.*, Phys. Rev. Lett. **78** (1997) 1648.

[Iori 93] I. Iori *et al.*, Nucl. Instrum. Methods **A325** (1993) 458.

[Jaqa 83] H.R. Jaqaman *et al.*, Phys. Rev. **C27** (1983) 2782.

[Jaqa 84] H.R. Jaqaman *et al.*, Phys. Rev. **C29** (1983) 2067.

[Jenn 86] B.K. Jennings *et al.*, Phys. Rev. **C33** (1986) 1303.

[Jeon 94] S.G. Jeong *et al.*, Phys. Rev. Lett. **72** (1994) 3468.

[Kim 92] Y.D. Kim *et al.*, Phys. Rev. **C45** (1992) 338.

[Klak 93] D. Klakow, G. Welke, and W. Bauer, Phys. Rev. **C48** (1983) 1982.

[Kolo 96] A. Kolomiets *et al.*, Phys. Rev. **C54** (1996) R472.

[Krof 89] D. Krofcheck *et al.*, Phys. Rev. Lett. **63** (1989) 2028.

[Krof 91] D. Krofcheck *et al.*, Phys. Rev. **C43** (1991) 350.

[Krof 92] D. Krofcheck *et al.*, Phys. Rev. **C46** (1992) 1416.

[Krus 85] H. Kruse, B.V. Jacak, and H. Stöcker, Phys. Rev. Lett. **54** (1985) 289.

[Kund 91] G.J. Kunde *et al.*, Phys. Lett. **B272** (1991) 202.

[Kund 95] G.J. Kunde *et al.*, Phys. Rev. Lett. **74** (1995) 38.

[Küpp 74] W.A. Küpper *et al.*, Ann. of Phys. **88** (1974) 454.

[Lace 93] R. Lacey *et al.*, Phys. Rev. Lett. **70** (1993) 1224.

[Lamb 81] D.Q. Lamb *et al.*, Nucl. Phys. **A360** (1981) 459.

[Land 80] L. Landau, E.M. Lifshitz, Course of Theoretical Physics: Statistical Mechanics Pergamon, New York (1980) 236.

[Lee 90] J.Lee, W. Beneson, and D.J. Morrisey, Phys. Rev. **C41** (1990) 2406.

[Lenk 89] R.J. Lenk and V.R. Pandharipande, Phys. Rev. **C39** (1989) 2242.

[Li 93] T. Li *et al.*, Phys. Rev. Lett. **70** (1993) 1924.

[Lisa 91] M.A. Lisa *et al.*, Phys. Rev. **C44** (1991) 2865.

[Lisa 93] M.A. Lisa, PhD. Thesis, Michigan State University, (1993).

[Lisa 95] M.A. Lisa *et al.*, Phys. Rev. Lett. **72** (1995) 2662.

[Litt 80] U. Littmark and J.F. Ziegler, Handbook of Range Distributions for Energetic Ions in all Elements, Pergamon Press, 1980.

[Lope 84] J.A. Lopez and P.J. Siemems, Nucl. Phys. **A431** (1984) 728.

[Lope 93] O. Lopez *et al.*, Phys. Lett. **B315** (1993) 34.

[Lync 87] W. G. Lynch, Ann. Rev. Nucl. Part. Sci. **37** (1987) 493, and ref. therein.

[Mack 77] F.D. Mackie and G. Baym, Nucl. Phys. **A285** (1977) 332.

[Mahi 88] M. Mahi *et al.*, Phys. Rev. Lett. **60** (1988) 1936.

[Marm 69] P. Marmier and E. Shelton, Physics of Nuclei and Particles, Vol. 1, Academic Press (1969) 38.

[Mich 94] K. Michaelian and A. Menchaca-Rocha, Phys. Rev. **B49** (1994) 550.

[Moli 85] J.J. Molitoris and H. Stöcker, Phys. Rev. **C32** (1985) 346.

[Mont 94] C.P. Montoya *et al.*, Phys. Rev. Lett. **73** (1994) 3070.

[More 72] L.G. Morreto, Phys. Lett. **40B** (1972) 185.

[More 75] L.G. Morreto, Nucl. Phys. **A247** (1975) 211.

[More 93] L.G. Morreto and G.J. Wozniak, Ann. Rev. Nucl. Part. Sci. **43** (1993) 379, and ref. therein.

[Moro 95] A. Moroni *et al.*, Nucl. Phys. **A583** (1995) 531.

[Morr 84] D.J. Morrissey *et al.*, Phys. Lett. **B148** (1984) 423.

[Morr 85] D.J. Morrissey *et al.*, Phys. Rev. **C32** (1985) 877.

[Morr 94] D.J. Morrissey, W. Benenson, and W.A. Friedman, Ann. Rev. Nucl. Part. Sci. **44** (1994) 27, and refs. therein.

[Müll 94] H. Müller and R.M. Dreizler, Nucl. Phys. **A563** (1994) 649.

[Mura 89] T. Murakami *et al.*, Nucl. Instrum. Methods **A275** (1989) 112.

[Naya 89] T.K. Nayak *et al.*, Phys. Rev. Lett. **62** (1989) 1021.

[Naya 92] T.K. Nayak *et al.*, Phys. Rev. **C45** (1992) 132.

[Nato 93] J.B. Natowitz *et al.*, Phys. Rev. **C48** (1993) 2074.

[Ogil 90] C.A. Ogilivie *et al.*, Phys. Rev. **C42** (1990) R10.

[Ogil 91] C.A. Ogilvie *et al.*, Phys. Rev. Lett. **67** (1991) 1214.

[Pan 93] Q. Pan and P. Danielewicz, Phys. Rev. Lett. **70** (1993) 2062.

[Pan 95] J. Pan and S. DasGupta, Phys. Rev. **C51** (1995) 1384.

[Pana 84] A.D. Panagiotou *et al.*, Phys. Rev. Lett. **52** (1984) 496.

[Part 95] M.D. Partlan *et al.*, Phys. Rev. Lett. **75** (1995) 2100.

[Peas 94] G.F. Peaslee *et al.*, Phys. Rev. **C49** (1994) R2271.

[Peil 89] G. Peilert *et al.*, Phys. Rev. **C39** (1989) 1402.

[Peil 94] G. Peilert *et al.*, Rep. Prog. Phys. **57** (1994) 533.

[Phai 92] L. Phair *et al.*, Nucl. Phys. **A548** (1992) 489.

[Phai 93] L. Phair, PhD. Thesis, Michigan State University, (1993).

[Phai 93a] L. Phair *et al.*, Nucl. Phys. **A564** (1993) 453.

[Poch 85] J. Pochodzalla *et al.*, Phys. Lett. **B161** (1985) 275.

[Poch 87] J. Pochodzalla *et al.*, Phys. Rev. **C35** (1987) 1695.

[Poch 95] J. Pochodzalla *et al.*, Phys. Rev. Lett. **75** (1995) 1040.

[Poch 96] J. Pochodzalla, Preceeding of First Catania Relativistic Ion Studies, Acicastello, Italy, May 27-31 (1996).

[Rave 83] D.G. Ravenhall *et al.*, Nucl. Phys. **A407** (1983) 571. 23

[Renf 84] R.E. Renfordt *et al.*, Phys. Rev. Lett. **53** (1984) 763.

[Ritt 85] H.G. Ritter *et al.*, Nucl. Phys. **A447** (1985) 3c.

[Rose 84] J.H. Rose *et al.*, Phys. Rev. Lett. **53** (1984) 344.

[Sain 88] F. Saint-Laurent *et al.*, Phys. Lett. **B202** (1988) 190.

[Saue 76] G. Sauer *et al.*, Nucl. Phys. **A264** (1976) 221.

[Sche 74] W. Scheid, H, Müller, and W. Greiner, Phys. Rev. Lett. **32** (1974) 741.

[Schl 87] T.J. Schlagel and V.R. Pandharipande, Phys. Rev. **C36** (1987) 162.

[Schm 90] R.P. Schmit, Phys. Rev. Lett. **65** (1990) 2080.

[Schw 93] C. Schwarz *et al.*, Phys. Rev. **C48** (1993) 676.

[Schu 82] H. Schulz *et al.*, Phys. Lett. **B119** (1982) 12.

[Serf 96] V. Serfling, Ph.D Thesis, University of Frankfurt (1996).

[Sero 86] B.D. Serot and J.D. Walecka, Adv. Nucl. Phys. **16** (1986) 1.

[Shen 93] W.Q. Shen *et al.*, Nucl. Phys. **A551** (1993) 333.

[Siem 79] P.J. Siemens and J.O. Rasmussen, Phys. Rev. Lett. **42** (1979) 880.

[Sobo 83] L.G. Sobotka *et al.*, Phys. Rev. Lett. **51** (1983) 2187.

[Song 83] S. Song *et al.*, Phys. Lett. **B130** (1983) 14.

[Stoc 73] W. Stocker and J, Buralaff, Nucl. Phys. **A202** (1973) 265.

[Stöc 78] H. Stöcker *et al.*, Z. Phys. **A286** (1978) 121.

[Stöc 80] H. Stöcker, J.A. Marhun, and W. Greiner, Phys. Rev. Lett. **44** (1980) 725 and ref. therein.

[Stöc 81] H. Stöcker *et al.*, W.Z. Phys. **A203** (1981) 259.

[Stoc 82] R. Stock *et al.*, Phys. Rev. Lett. **49** (1982) 1236.

[Stöc 86] H. Stöcker and W. Greiner, Phys. Rep., **137** (1986) 277.

[Stoc 86a] R. Stock, Phys. Rep. **135** (1986) 259.

[Sull 90] J.P. Sullivan *et al.*, Phys. Lett. **B249** (1990) 8.

[Sull 92] J.P. Sullivan and J. Péter, Nucl. Phys. **A540** (1992) 275.

[Sura 87] E. Surand, Nucl. Phys.**A462** (1987) 109.

[Sura 89] E. Surand *et al.*, Phys. Lett. **B229** (1989) 359.

[Sura 90] E. Surand, Proceeding of the XXVIII International Winter Meeting on Nuclear PHysics, Bormio, Italy, Jan. 22-26, 1990, and references therein.

[Trei 81] J. Treiner *et al.*, Nucl. Phys. **A317** (1981) 253.

[Tsan 84] M.B. Tsang *et al.*, Phys. Rev. Lett. **52** (1984) 1967.

[Tsan 84a] M.B. Tsang *et al.*, Phys. Lett. **B148** (1984) 265.

[Tsan 86] M.B. Tsang *et al.*, Phys. Rev. Lett. **57** (1986) 559.

[Tsan 88] M.B. Tsang *et al.*, Phys. Rev. Lett. **60** (1988) 1479.

[Tsan 89] M.B. Tsang *et al.*, Phys. Rev. **C40** (1989) 1685.

[Tsan 90] M.B. Tsang *et al.*, Phys. Rev. **C42** (1990) R15.

[Tsan 91] M.B. Tsang *et al.*, Phys. Rev. **C44** (1991) 2065.

[Tsan 92] M.B. Tsang *et al.*, Phys. Lett. **B297** (1992) 243.

[Tsan 93] M.B. Tsang *et al.*, Phys. Rev. Lett. **71** (1993) 1502.

[Tsan 96] M.B. Tsang *et al.*, Phys. Rev. **C53** (1996) R1057.

[Tsan 96a] M.B. Tsang *et al.*, NSCL preprint 1035 (1996).

[Wang 91] S. Wang *et al.*, Phys. Rev. **C44** (1991) 1091.

[Wang 95] S. Wang *et al.*, Phys. Rev. Lett. **74** (1995) 2646.

[Weat 96] L.W. Weathers and M.B. Tsang, Nucl. Instrum. Methods **A381** (1996) 567.

[Weis 37] V.F. Weisskopf, Phys. Rev. **52** (1937) 295.

[Welk 88] G.M. Welke *et al.*, Phys. Rev. **C38** (1988) 2101.

[West 78] G.D. Westfall *et al.*, Phys. Rev. **C17** (1978) 1368.

[West 85] G.D. Westfall *et al.*, Nucl. Instrum. Methods **A238** (1985) 347.

[West 93] G.D. Westfall *et al.*, Phys. Rev. Lett. **71** (1993) 1986.

[Will 96] C. Williams, PhD. Thesis. Michigan State University, (1996).

[Wile 92] J.L. Wile *et al.*, Phys. Rev. **C45** (1992) 2300.

[Wils 90] W.K. Wilson *et al.*, Phys. Rev. **C41** (1990) R1881.

[Wong 82] C.Y. Wong, Phys. Rev. **C25** (1982) 1460.

[Xi 93] H. Xi *et al.*, Nucl. Phys. **A552** (1993) 281.

[Xi 96] H. Xi *et al.*, Phys. Rev. **C54** (1996) R2163.

[Xi 97] H. Xi *et al.*, Phys. Rev. Lett. in press (1997).

[Xu 86] H.M. Xu *et al.*, Phys. Lett. **B182** (1986) 155.

[Xu 89] H.M. Xu *et al.*, Phys. Rev. **C40** (1989) 186.

[Xu 90] H.M. Xu *et al.*, Phys. Rev. Lett. **65** (1990) 843.

[Xu 91] H.M. Xu *et al.*, Phys. Lett. **B261** (1991) 240.

[Xu 93] H.M. Xu, P. Danielewicz, and W.G. Lynch, Phys. Lett. **B299** (1993) 199.

[Xu 94] H.M. Xu, W.G. Lynch, and P. Danielewicz, Phys. Rev. **C50** (1994) 1659.

[Xu 94a] H.M. Xu, Nucl. Phys. **A568** (1994) 365.

[Zhan 90] W.M. Zhang *et al.*, Phys. Rev. **C42** (1990) R491.

[Zhan 94] J. Zhang *et al.*, Phys. Rev. **C50** (1994) 1617.

[Zhu 92] F. Zhu *et al.*, Phys. Lett. **B282** (1992) 299.

[Zhu 94] F. Zhu *et al.*, Phys. Lett. **B322** (1994) 43.

[Zhu 95] F. Zhu *et al.*, Phys. Rev. **C52** (1995) 784.